Design of miniaturized wearable broadband energy harvesters

Gljušćić, Petar

UNIVERSITY OF RIJEKA
FACULTY OF ENGINEERING

Petar Gljušćić

DESIGN OF MINIATURIZED WEARABLE BROADBAND ENERGY HARVESTERS

DOCTORAL DISSERTATION

Rijeka, 2022.

UNIVERSITY OF RIJEKA
FACULTY OF ENGINEERING

Petar Gljušćić

DESIGN OF MINIATURIZED WEARABLE BROADBAND ENERGY HARVESTERS

DOCTORAL DISSERTATION

Thesis Supervisor: Prof. D. Sc. Saša Zelenika

Rijeka, 2022.

SVEUČILIŠTE U RIJECI
TEHNIČKI FAKULTET

Petar Gljušćić

KONSTRUKCIJA NOSIVOGA UREĐAJA MINIJATURIZIRANIH DIMENZIJA ZA PRIKUPLJANJE I PRETVORBU NISKORAZINSKE ENERGIJE IZ OKOLIŠA

DOKTORSKA DISERTACIJA

Mentor: prof. dr. sc. Saša Zelenika

Rijeka, 2022.

Thesis Supervisor: Prof. D. Sc. Saša Zelenika, University of Rijeka, Croatia, Faculty of Engineering

This doctoral thesis was discussed on March 25th 2022 at the University of Rijeka, Croatia, Faculty of Engineering in front of the following Evaluation Committee:

1. Assist. Prof. D. Sc. Jelena Srnec Novak, University of Rijeka, Faculty of Engineering, Croatia

2. Prof. D. Sc. Željko Domazet, University of Split, Faculty of Electrical Engineering, Mechanical Engineering and Naval Architecture, Croatia

3. Prof. D. Sc. Francesco De Bona, University of Udine, Polytechnic Department of Engineering and Architecture, Italy

Acknowledgements

The research topic presented in this thesis is the result of extensive physical experiments and numerical modelling conducted by the author, many of which would not be possible without the support of helpful individuals, each in their field. First, I would like to thank my thesis supervisor, Prof. D. Sc. Saša Zelenika for his helpful comments and discussions during the work on the thesis. I would also like to thank Assist. Prof. D. Sc. Ervin Kamenar for his guidance and advice with all areas dealing with sensor technology, control and electrical phenomena, and D. Sc. Marko Perčić for his consultation regarding various Design-of-Experiments methods, as well as all the students who contributed to the herein presented work through their theses and projects. Moreover, special thanks should also be given to my colleagues, family and friends for their patience, support and understanding during my studies. Thank you all!

Abstract

Energy harvesting (EH) is the process of collecting low-level ambient energy and converting it into electrical energy to be used for powering miniaturized autonomous devices, wearable electronics or Internet-of-Things components. The use of kinetic energy, converted into electrical energy via the piezoelectric principle, is of special interest in this frame. The main drawback of piezoelectric EH devices is the narrow area of optimal operation around the eigenfrequency of a specific device. The voltage levels achieved within this area are high, but they rapidly decrease with the variation of the excitation frequency. This is especially important in wearable applications, where the excitation frequency from human motion varies randomly.

Based on a thorough analysis of the state-of-the-art in energy harvesting, with a particular focus on wearable applications, an innovative design approach, which comprises the segmentation of a conventional energy harvester into optimized segments, excited by plucking their free ends is proposed in this work. An original method of optimization is utilized here, combining the DoE methodology and a complex experimentally validated numerical model. Several novel miniaturized energy harvesters with optimized shapes are suggested, produced and experimentally tested, while keeping in consideration, in this frame, the generally neglected fatigue strength. The experimental results have shown a good match with the numerical data. The results show that a significant increase in performance, i.e., up to ~ 500%, can be achieved by using the herein proposed design approach, compared to a conventional device. What is more, the proposed optimized devices are capable of providing enough power for a compact wearable device aimed for biomedical application, requiring ~ 5 mW of power, also suggested in this work. An extensive DoE-based experimental study of plucking parameters is also carried out, providing a deeper insight into the complex mechanism of impact excitation, as well as valuable guidelines for plectrum design, using additive manufacturing. The concept of the design of a wearable watch-like device is also developed, capable of generating an estimated ~ 270 mW of maximum power as well as ~ 6.8 mW of average power.

The performed research provides a significant scientific contribution to the field of kinetic EH by proposing an optimized solution to the aforementioned problem, based upon an original framework of application of state-of-the-art approaches. The results obtained on optimized design configurations are validated and verified by using numerical and experimental methods.

Keywords: piezoelectric energy harvesters, wearables, DoE, frequency up-conversion, optimized geometry, FE numerical modelling, experimental assessment

Prošireni sažetak

"Žetva energije" (engl. *energy harvesting,* EH) je proces prikupljanja niskorazinske energije iz okoliša te njene pretvorbe u električnu energiju, s ciljem napajanja minijaturiziranih autonomnih uređaja, uređaja za nosive tehnologije te komponenti za „Internet stvari".

Nosive tehnologije pogonjene EH sustavima mogu se koristiti u telemedicini za praćenje stanja pacijenata, automatsko doziranje lijekova te za praćenje zdravstvenog stanja radnika zaposlenih na poslovima visokog rizika. U ovom pogledu, upotreba kinetičke energije, pretvorene u električnu pomoću piezoelektričnog učinka, od posebne je važnosti. Najveći nedostatak koji se pojavljuje kod primjene piezoelektričnih uređaja je njihovo usko područje optimalnog rada oko vlastite frekvencije specifičnog uređaja. Vrijednost napona, koju je moguće postići u tom području, je visoka, ali ona naglo opada već kod neznatne promjene uzbudne frekvencije. Ta je pojava posebno izražena kod primjene u nosivim tehnologijama, gdje uzbudna frekvencija, uzrokovana gibanjem čovjeka, nasumično varira. Kako bi se prevladao opisani problem, osmišljena je metoda konstruiranja piezoelektričnih pretvarača temeljena na detaljnoj analizi recentne literature, koja kombinira podjelu konzole u veći broj optimiziranih segmenta izloženih uzbudi trzanjem slobodnog kraja pomoću mehanizma pretvorbe frekvencije (engl. *frequency up-conversion*).

Postupkom optimizacije kombinacijom metodologije dizajna eksperimenata (DoE) i korištenja složenih numeričkih modela i analiza, predložene su optimizirane geometrije piezoelektričnih uređaja prilagođene primjenama u nosivim tehnologijama, a posebno najčešće upotrebljavanim senzorima stanja ljudskog zdravlja, te koje pokazuju bolja radna svojstva od trenutno komercijalno dostupnih konstrukcija. Numerički modeli razvijenih konstrukcijskih oblika validirani su pomoću eksperimentalnih mjerenja provedenih na originalno razvijenim postavama te se dobiveni rezultati izuzetno dobro poklapaju s numeričkim podacima. U sklopu ispitivanja uzeta su u obzir ograničenja uzrokovana dinamičkom čvrstoćom materijala, što se u literaturi najčešće zanemaruje. Rezultati dobiveni eksperimentalnim ispitivanjem optimiziranih minijaturiziranih uređaja pokazali su kako je, koristeći metodu konstruiranja predloženu u sklopu ovoga rada, moguće postići višestruko povećanje izlazne snage, normalizirane po površini uređaja, i to i do ~ 500%. Uz to, pokazano je da su razvijeni uređaji u mogućnosti proizvesti dovoljno snage za pokretanje kompaktnog nosivog uređaja namijenjenog za primjenu u medicini (~ 5 mW).

Opsežna eksperimentalna studija, temeljena na DoE metodologiji, provedena je i s ciljem analize parametara procesa trzanja slobodnog kraja konzole pomoću trzalice izrađene aditivnim

tehnologijama te njihovog utjecaja na odziv pretvarača. Time je dobiven dublji uvid u složen mehanizam uzbude trzanjem, kao i važne smjernice za optimalno konstruiranje trzalica namijenjenih za izradu pomoću aditivnih tehnologija. Također je razvijeno i konceptualno rješenje nosivog uređaja u obliku sata, koji se sastoji od dva miniaturizirana optimizirana uređaja za prikupljanje kinetičke energije, podvrgnuta uzbudi trzanjem pomoću kompaktnog mehanizma za pretvorbu frekvencije. Najveća predviđena izlazna snaga takvog uređaja je ~ 270 mW, dok prosječna izlazna snaga iznosi ~ 6,8 mW, što premašuje potrebe predloženog medicinskog nosivog uređaja.

Znanstveni doprinos ovog istraživanja ostvaren je kroz originalnu metodu konstruiranja piezoelektričnih uređaja za prikupljanje niskorazinske energije iz okoliša, koja rezultira višestrukim povećanjem (i do ~ 5 puta) izlazne snage kod optimiziranih uređaja. Metoda uzbude trzanjem slobodnog kraja u kombinaciji s optimizacijom segmenata omogućuje konkretizaciju minijaturiziranog piezoelektričnog EH sustava, prilagođenog za prikupljanje i pretvorbu energije nasumične kinematičke uzbude gibanja ljudi. Uključivanjem dinamičke čvrstoće materijala u postupak konstruiranja EH uređaja, osiguran je dugotrajan rad takvog sustava, izloženog dinamičkim uvjetima rada. Izlazna snaga tako konstruiranog EH sustava predstavlja realističnu vrijednost, koju je moguće očekivati kod njegove stvarne primjene kroz njegov cjelokupan vijek trajanja.

Znanstvenim doprinosom području nosivih tehnologija i prikupljanja niskorazinske energije iz okoliša danim u doktorskoj disertaciji stvoren je tako temelj za razvoj nove klase konstrukcijskih konfiguracija autonomnih nosivih uređaja pokretanih energijom gibanja ljudi sa širokom primjenom na području medicine i sporta ali i „industrije 4.0“, „interneta stvari“ (IoT) te praćenja stanja struktura u strojarskim i građevinskim konstrukcijama (engl. *structural health monitoring*).

Ključne riječi: piezoelektrični uređaji za prikupljanje niskorazinske energije iz okoliša, nosive tehnologije, dizajn eksperimenata, pretvorba frekvencije, optimizacija geometrije, numeričko modeliranje, experimentalna mjerenja

TABLE OF CONTENTS

1. INTRODUCTION

In the initial part, the general introductory information about the presented research is provided. A brief overview of the general scientific motivation, aims and contributions of the conducted research presented in this thesis, and an outline of the thesis organization is hence given.

1.1. Scientific Motivation

With the ever increasing advancement of electronic components, reflected also in the corresponding reduction of sizes and power requirements, as well as with the concurrent raise of the awareness on the importance of well-being, fitness and preventable health issues, a new class of devices, i.e., wearables, has been rapidly evolving in the last couple of decades [113, 176]. Wearable devices, commonly worn as a wrist or arm accessory, e.g. a watch-like device, or as a part of clothing, can, in fact, be found today in a wide range of applications [75]. A wide array of such devices can be found in physiological sensing applications, e.g. as heartrate and oxygen saturation monitors, or as activity monitors. These devices do display, however, the potential for a far broader utilization [71, 95, 116]. Wearable devices, depending on their application, can comprise a variety of sensors, e.g. accelerometers in fall detectors or temperature sensors and pulse oximeters in remote health monitors, or in telemedicine applications, but they encompass also data processing and communication components, power management circuitry and a power source, i.e., a battery [1, 71, 95]. In order to enable a wider implementation of continuous health monitoring, such devices necessitate a reliable power source able to sustain their operation over long time periods [79, 224]. Conventional non-renewable power sources, i.e. batteries, require periodical recharging and eventual replacement, substantially limiting the devices' autonomy as well as generating waste upon expiration [192]. What is more, batteries can also restrict the miniaturization of wearable devices, easily exceeding by several times the volumetric size of the sensors they are powering [192]. However, wearable devices employed in biomedical applications, i.e. health monitoring, could be significantly improved by replacing the conventional power source with an energy harvesting (EH) system, collecting renewable ambient energy [175, 192]. Such an upgrade would allow a further reduction of their dimensions and masses, while, more importantly, achieving an increased power autonomy as well as having positive environmental effects, reducing the amount of hazardous waste from the materials present in batteries [129, 192]. Energy harvesting is the process of collecting low level ambient energy from the environment and its conversion into usable electrical energy. Depending on

the available energy source, various approaches can be employed in this frame: waste heat can be converted using thermoelectric generators (TEGs), ambient radio frequency (RF) can be collected with special antennas, and, particularly significant for wearable applications, vibrations from human, animal and machine motion can be collected and converted via piezoelectric energy harvesters (PEHs) [97, 160]. Vibrations caused by human motion, during walking, running and other activities of daily living (ADL), represent, in fact a copious and readily available energy source for wearable devices. Since, however, the kinetic excitation induced by human motion is random in nature, it can cause challenges inherent to PEHs [17, 88, 70]. In effect, a typical PEH generates its highest voltage output when excited near its eigenfrequency, with the efficiency being significantly reduced even when the excitation frequency is slightly shifted [97, 160]. Recent literature describes a considerable number of promising approaches aimed at solving this issue, by broadening the operating frequency spectrum of a PEH as well as by overcoming the problem caused by random excitation, some of which will be described, analysed and used later in this work [17, 86, 105, 161, 198]. A thorough analysis and optimization of PEH design parameters, along with the application of state-of-the-art modelling tools and experimental measurements, will enable the development of piezoelectric energy harvesting devices optimized for maximum performance when integrated as a power source in innovative autonomous wearable devices. A design solution of such a device will be developed and tested, as a proof-of-concept of the herein used design approach. To reduce the cost and increase the reliability of the end device, the principle of simplicity in mechanical design will be used as a guideline in shape optimization as well as in prototype development [102]. The important, but often overlooked issue of privacy and data protection should also be addressed when dealing with the widespread use of autonomous wearable devices and Internet-of-Things (IoT) systems in collecting personal medical data. The integrity of the thus acquired data, its usability and auditing represent, along with the overall privacy of the patient information, the main area of concern in this regard [190]. Recent literature not only analyses the possible dangers of such systems, but also provides potential privacy-preserving solutions, several possible data encryptions (cryptographic) and control approaches, trusted third party auditing of the acquired data, as well as data anonymization via the usage of identifiers such as ID numbers, names or phone numbers. In an IoT system, collected private and public data should, in any case, be clearly distinguished in order to maintain the “public and private border line”, especially when dealing with sensitive personal medical data [14, 190, 194].

1.2. Aims of the Work

Based on the outlined motivation, the goal of this thesis is to contribute to the understanding of the influence of design parameters on the behaviour of miniaturized piezoelectric energy harvesters. The thesis is particularly focused on addressing the problem of conventional PEHs' narrow operating frequency bandwidth, as well as overcoming the issues with the random excitation from human motion, which represent major deterrents to the integration of miniaturized PEHs in wearable devices. Such devices could, through their reduced size and increased power autonomy, be especially applicable in the fields of telemedicine and remote patient monitoring. For this purpose, a combined approach of geometry optimization using Design-of-Experiments (DoE) methods, synergistically merged with an innovative impact excitation mechanism, will be studied. In order to conduct the optimization, as well as to thoroughly analyse its results, complex numerical models will be used comprising modal, harmonic and transient analyses. What is more, additional stress analyses of the optimized PEHs, generally neglected in most of the available literature, will be carried out to ensure that the stress levels are kept below the dynamic limits of the piezoelectric material during the experiments, which will, in turn, provide useful data for the development of long-lasting PEH-powered devices. To validate the numerical models, the ensuing results will be compared with the data acquired in harmonic and impact excitation experimental measurements. Furthermore, a detailed study of the effects of the properties of the excitation mechanisms on the PEH responses will also be carried out and the results will be analysed using numerical methods. The thus attained data will, in turn, be utilized for the development of a design solution of a wearable device comprising optimized PEH geometry as well as an innovative impact excitation mechanism. The described research will provide a novel mechanical engineering design approach to solve the issues inherent in PEH devices, as well as significantly contribute to the future development of a new class of autonomous wearable devices.

1.3. Contributions of the Thesis

The research performed in the frame of the doctoral thesis strives to provide a scientific contribution to the study of novel miniaturized wearable energy harvesting devices for medical applications, particularly the area focusing on the piezoelectric principle. The contribution of this work comprises a thorough study of the effects of geometrical parameters on the performances of piezoelectric energy harvesters, along with the development of an innovative com-

pact impact excitation mechanism, so to overcome the random excitation issues present in wearable PEH applications. Several innovative geometry variations are therefore studied, including segmented cantilevers and those with added stress concentrators, all optimized in order to generate a maximum specific power output. Addressing these issues includes both the numerical as well as the experimental approach. The complex numerical analyses, in a synergistic combination with an optimization approach using DoE methods, give a deep insight into the way the design parameters affect the performances of PEHs and result in an original comprehensive mechanical engineering approach for achieving optimized PEH performances in terms of the obtainable specific power levels within the given environmental conditions, i.e., for wearable applications. What is more, the assessment of the mechanical limitations of the studied dynamical systems allows an improved approach towards the final design of compact autonomous wearable devices, so that they can withstand longer operating cycles, while maintaining the same performance levels. The experimental part of the performed research consists of the development of innovative experimental setups suitable for the validation of the used numerical simulations, based on both harmonic excitations as well as impact excitations. All of the novel optimized PEH variations developed using the aforementioned optimization methods are thus experimentally tested, and the attained results are compared with the numerical data. What is more, an additional study is carried out, so as to investigate the effects of the excitation mechanism's parameters on the performances of a PEH subjected to impact excitation. Both the simulations and the experiments have resulted in significantly increased specific voltage and power outputs (up to ~ 5 times compared to the conventional rectangular devices), that clearly match the requirements of powering wearable medical sensors with the coupled data collection, elaboration and transmission modules. The conclusions derived from the aforementioned results provide a valuable contribution to the future development of the design of a new class of miniaturized piezoelectric energy harvesters, notably those aimed at wearable applications. A conceptual design of a compact watch-like device, aimed to be worn on the wrist, is presented in this work, comprising the novel optimized PEHs subjected to impact excitation, able to ensure a reliable power supply. The compact optimized EH systems presented in this work, purposely adapted to random excitations, represent a relevant enabling technology for the advancement and evolution of autonomous wearable devices, with promising use in telemedicine, work safety, professional athletics, industry 4.0, IoT and structural health monitoring systems.

1.4. Organization of the Thesis

The basic structure of the doctoral thesis is organized in sections, each covering one of the main parts of the research. Section 1 describes the primary scientific motivation along with the research objectives and particularly emphasizes the contributions given to the considered field of research. In Section 2 the basics of wearable devices as well as of the generally used energy harvesting principles are explained, along with the issues related to human motion excitation and the potential solution. The state-of-the-art in wearable kinetic energy harvesting technologies is also elaborated in detail within this section. Section 3 provides an overview of the electronic components typically found in medical wearable devices. The most commonly used sensors, data processing and communication modules, as well as energy storage and power management components are listed, and their main characteristics are highlighted. Furthermore, the duty cycles for various sensors are discussed according to medical practice, and a wearable medical device is proposed. The experimental and numerical methods used in this work are thoroughly described in Section 4. The detailed depiction of the used innovative experimental setups is given and the damping coefficient of the used harvesting devices is assessed. All segments of the complex numerical models are also covered and the mesh sensitivity analysis is carried out. The analysis of PEH design parameters, i.e., the initial study of the influence of the design parameters, as well as the detailed description of the used optimization process relying on advanced DoE methods are covered in Section 5. The thus proposed shapes of the optimized PEHs, along with their final dimensions, are also given in this section. This is followed by a comprehensive strength analysis, allowing assessing the inherent limits of their operating conditions within the respective fatigue strength limits, and therefore a safe long-term operation of the suggested devices. In Section 6 the obtained experimental results are exhibited and interpreted, and the numerical models are experimentally validated. The results of impact excitation experiments are reported, and the power outputs of all optimized PEHs are determined. The performances of the studied PEHs are also thoroughly critically analysed in this section. In Section 7, a basic outline of the used additive manufacturing method is given, along with the results and conclusions derived from the experimental study of the properties of the 3D printed excitation mechanism. A detailed description of the development of an elaborated wearable device design solution is also provided, and the power output levels are estimated. The conclusion of the thesis given in Section 8 contains the summary of the main observations and comments, as well as a description of possible prospects for future research.

2. STATE-OF-THE-ART

The integration of an optimized energy harvesting device into wearable devices could prove to be a beneficial addition to the rapidly growing field of wearable technology, especially aimed at medical applications. Such a step would enable the development of autonomous wearable devices, and significantly expand the application possibilities of wearables. An introduction to wearable technologies as well as energy harvesting principles, particularly the piezoelectric approach, will be given in this section of the work, together with a comprehensive overview of the state-of-the-art in these fields of research.

2.1. Wearable technologies

As worldwide connectivity increases, a new interesting trend of wearable technologies emerges in the mobile device market, showing a steady global growth during the last decade (Figure 2.1.), with Asia and North America being strong leaders in the field. A rising number of users, wishing an unlimited connectivity and unhindered social media interactions, express an interest to possess wearable mobile devices that can be in the form of an accessory or a part of their clothing [54, 176].

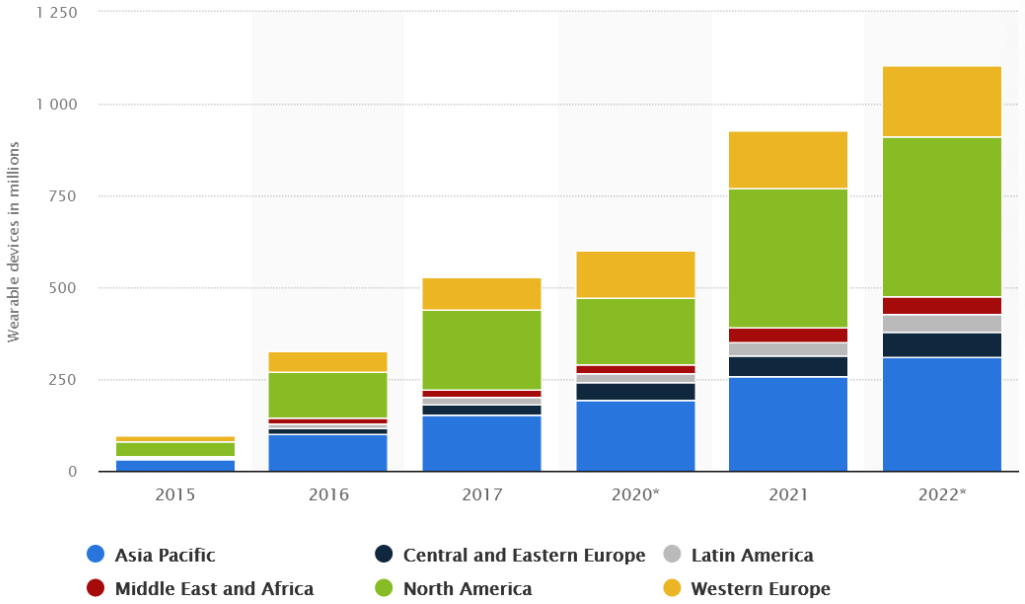

Figure 2.1. Number of connected wearable devices worldwide from 2015 to 2022 (in mil.) [54].

What is more, as the ideas of fitness, well-being and a wider appreciation of wellness have gained a strong prominence in modern everyday life, the need for more advanced wearables, not limited to weight loss monitors and step counters, is rising. These novel “personal

healthcare" devices provide an insight into the users' activity in the form of physical and mental health monitoring, i.e., heart rate, body fat percentage, sleep quality, stress levels, fitness tracking and similar or related data, but they can facilitate also more mundane tasks, such as checking incoming text messages, viewing urgent information, and enabling financial transactions [12, 75, 176].

When considering the various concepts of wearable devices and the different approaches to their design, Seneviratne et al. [176] provide a comprehensive classification of both commercially available wearables as well as some related research prototypes:

- **accessories**, i.e., smart watches or wristbands, smart eyewear, headsets or straps [71, 83, 95, 173, 209, 228] –devices with embedded sensors, with or without a display, with fitness or health monitoring, as well as with wireless communication hand free control or other functionalities;
- **e-textiles**, i.e., smart main garments and foot or hand worn devices [2, 101, 136] – shirts, pants, gloves and shoes embedded with sensors, and
- **e-patches**, i.e., sensor patches and e-tattoos or e-skin [208, 225] – adhesive sensor patches placed on the skin with haptic or fitness tracking functionalities, as well as flexible or stretchable electronics used as sensors or for wireless communication [176].

A typical wearable device designed for biomedical applications, e.g. for remote patient monitoring, comprises a sensor module for tracking a set of health parameters (such as heart rate, blood oxidation, blood pressure, fall detection etc.), a data processing/storage module (data logger), and preferably a low power communication system and a power supply [12, 71].

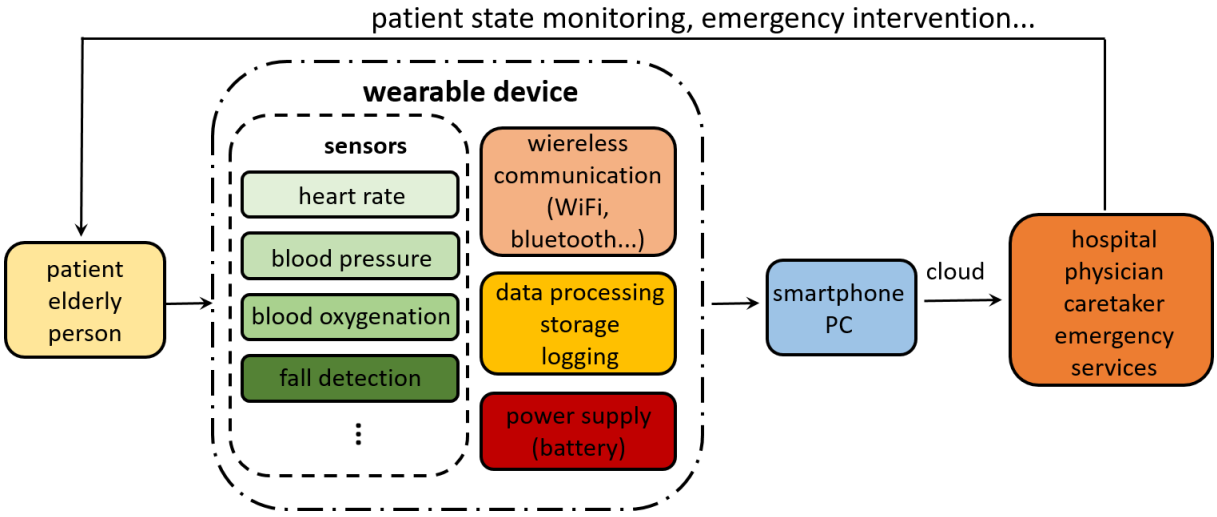

Figure 2.2. Block diagram of the operating process of a medical wearable device.

Such a device, worn by the user, e.g. a patient recovering at home or an elderly person, tracks the user's state of health through a selected set of parameters and stores the collected data. It

can be permanently or periodically connected to the internet via a smartphone or a PC, and send the health parameters data to the cloud, where an expert, e.g. a physician or caretaker, can check the user's state and act accordingly in case of an emergency (Figure 2.2.) [12, 71, 228]. If a medical wearable device is also equipped with a miniaturized drug delivery system, a physician at the hospital could remotely adjust the patient's medicament dose in real time, based on the data gathered by the same device [148, 178, 212]. In case of chronic diseases, the drug delivery could even be automated, e.g. in case of insulin delivery [23].

Together with the above described medical use, i.e., in patient health monitoring and early detection of disorders and automated drug delivery, similar devices can be employed in a wide range of potential applications such as, but not limited to [71, 95, 116]:

- **risky professions:** monitoring of the workers´ state to prevent dangerous situations or potential injuries, particularly common in construction, mining or shipbuilding;
- **education:** stress level and health condition monitoring could provide a suitable foundation for the development of personalized learning plans, time management recommendations, or for scheduling of classroom activities;
- **office environment and industry:** occupational stress can be the cause of health deterioration, implying that the monitoring of the health parameters of the employees can be beneficial in preventing such occurrences;
- **sports and recreation:** monitoring of parameters related to training activities and health conditions allows the prevention of injuries, achieving optimal fitness levels or assessing sleep quality.

A wearable device, as all electronic devices, requires a source of power in order to operate. Typically, this is achieved by using a conventional power source such as a replaceable or rechargeable battery. With the necessity to replace or recharge them, such devices possess a limited autonomy, which can be of significant importance when working with elderly people or patients living in remote locations [192]. Furthermore, if the discarded batteries are taken into consideration, along with the relatively low lifespan of rechargeable batteries, the resulting environmental impact is not negligible [41].

The conventional (battery) power supply found in the aforementioned type of devices could be replaced with an optimized EH system, which would collect waste energy from human motion and convert it into usable electrical energy to power the wearable device. The principles of energy harvesting, along with the issues that arise with its implementation into wearable technologies, as well as the potential solutions, will be thoroughly explained in the following subsection.

2.2. Energy harvesting and wearables

The energy harvesting approach to power generation is an elegant way to replace conventional power sources in wearable devices by collecting surplus energy generated by the human body during typical activities of daily living and converting it into electrical energy. The specific nature of human behaviour, however, causes certain issues with this approach, which will be covered next, together with some of the most promising solutions.

2.2.1. Energy harvesting

Energy harvesting is the process of collecting low-level ambient energy from the environment and converting it into usable electrical energy. The thus collected electrical energy can be used or stored using super capacitors, and managed using a suitable power management system [97, 160, 192]. Among the numerous ambient energy sources present in the environment, the ones considered most promising in the EH framework are solar or artificial light energy; waste heat, emitted by many mechanical and biological systems; radio frequency (RF), present in the environment due to the radio emissions from communication networks; and kinetic energy, generated by all moving systems, mechanical, atmospheric and biological [38, 171, 172]. Each of the listed energy forms can be collected and converted into usable electricity by employing specific technologies. Light energy can, thus, be converted into electricity via photovoltaic modules, using the photoelectric effect (Figure 2.3a) [115, 122, 160, 201]. Any substantial temperature gradient can be utilized as a power source by using TEGs, i.e., solid state semiconductor based devices that use the Seebeck effect to generate voltage from the flow of heat (Figure 2.3b) [35, 72, 145, 160, 192] . Specialized miniaturized antennas (Figure 2.3c) can be employed to collect and convert ambient electromagnetic (EM) radiation, such as RF waves, within a wide frequency spectrum, i.e., mobile communication [9, 114, 192, 206].

When kinetic energy, a ubiquitous and copious energy form, is considered, there is a wide array of technologies aimed at its collection and conversion, from more conventional approaches such as miniaturized electric generators and electromagnetic vibration energy harvesters, to more advanced ones, such as triboelectric, magnetostrictive, electrostatic and piezoelectric energy harvesters [97, 160, 226]. Conventional miniaturized electric generators (Figure 2.3d) represent a simple and off-the-shelf method to collect ambient kinetic energy; they can be coupled to a micro turbine and utilized to collect energy from e.g. a flowing river [94]. Electromagnetic energy harvesters, as shown in Figure 2.3e, typically comprise a moving per-

manent magnet within a coil. The movement of the magnet relative to the coil, excited by ambient vibration, e.g. a passing vehicle, generates electricity [29]. In a triboelectric energy nanogenerator (TENG - Figure 2.3f), charge is induced between two different triboelectric surfaces that are in contact due to pressure or bending. When the surfaces are separated with release of pressure, electric potential builds on the back electrodes [213].

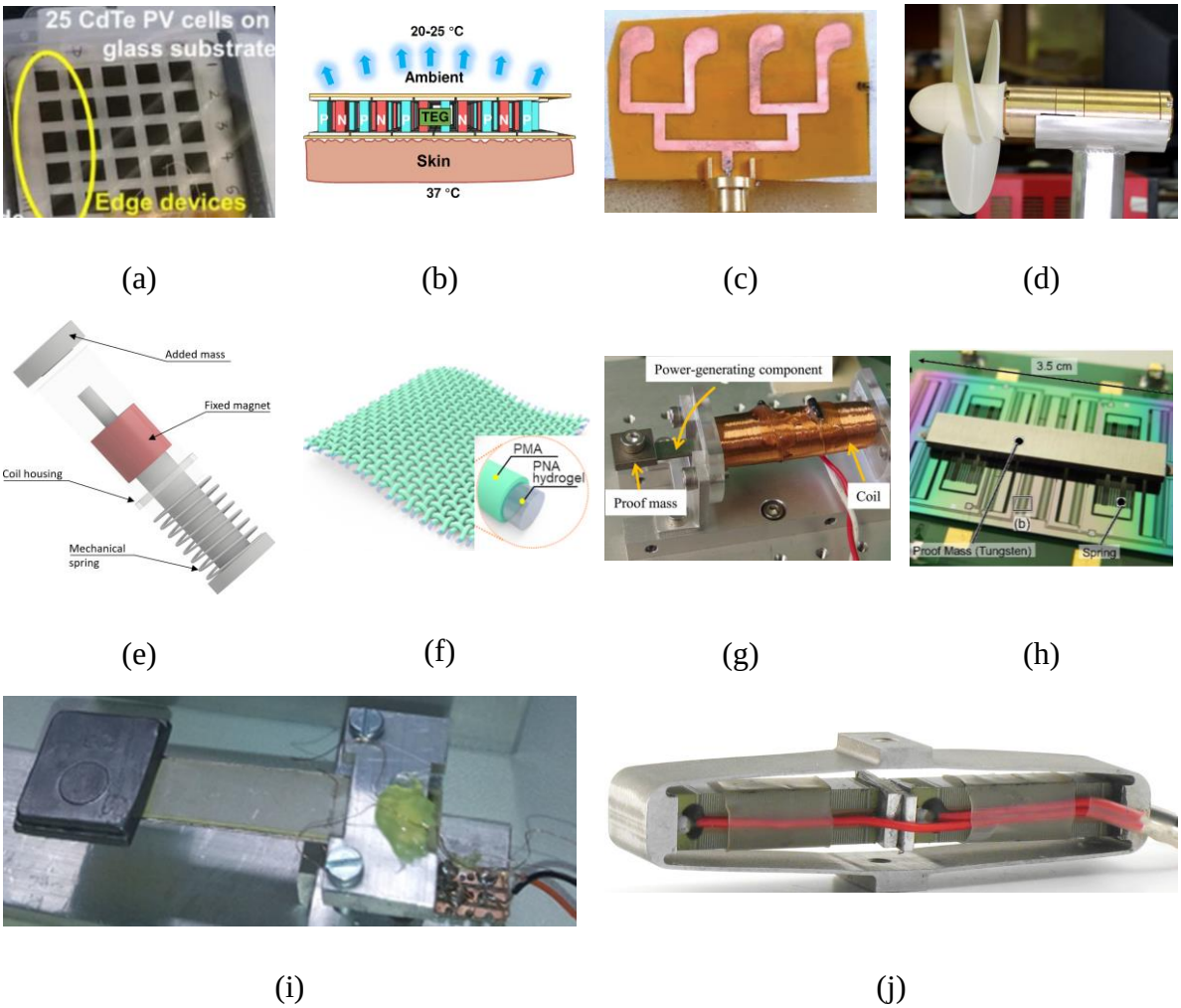

(a) (b) (c) (d)

(e) (f) (g) (h)

(i) (j)

Figure 2.3. EH technologies for different energy sources: PV modules [122] (a), TEG [145] (b), specialized RF antenna [206] (c), miniaturized turbine generator [94] (d), EM vibrations EH [29] (e), triboelectric EH textile [180] (f), magnetostrictive kinetic EH [223] (g), ES kinetic EH device [85] (h), cantilever PEH (31 mode) [17] (i), PEH stack (33 mode) [34] (j).

The magnetostrictive effect is a phenomenon similar to the piezoelectric effect, i.e., elongations are induced by subjecting the material to a magnetic field due to magneto-elastic coupling. An inverse effect takes place when stress is applied to the material [15, 223, 226]. An example of an experimental magnetostrictive device is shown in Figure 2.3g. The basic operating principle of electrostatic energy harvesters, shown in Figure 2.3h, is to use micro-electro-mechani-

cal (MEMS) structures to modulate the capacitance between two surfaces, i.e. a variable capacitor, induced by mechanical vibration. By constraining charge on the capacitor and the capacitance decreases, the charge will migrate from the capacitor towards a load or a storage element, converting thus the mechanical energy into electrical energy [85, 97, 160].

The intrinsic property of piezoelectric materials is that the mechanical strains of the piezoelectric structure are converted into charge (electric field), i.e. voltage. This phenomenon, known as the piezoelectric effect, occurs due to electromechanical coupling. When, in turn, voltage is applied to the piezoelectric material, mechanical deformations occur, which is caused by backwards electromechanical coupling resulting in the reverse piezoelectric effect [8, 160].

The piezoelectric effect, generating charge from strain caused by mechanical forces applied either perpendicularly to or in line with the poling direction, governed by the piezoelectric strain coefficient *d*, i.e. the ratio of induced electric charge and mechanical stress, can be determined using its fundamental equations:

$$\delta = \frac{\sigma}{E} + d \cdot E_{\text{el}} \tag{2.1}$$

$$D = \varepsilon \cdot E_{\text{el}} + d \cdot \sigma \tag{2.2}$$

where δ represents mechanical strain, σ the mechanical stress, E is the Young's modulus of the piezoelectric material, d refers to the piezoelectric strain coefficient, while E_{el} represents the electric field. D is charge density, i.e., the electrical displacement and ε refers to the dielectric constant of the piezoelectric material. Only two modes are typically considered to be practical, and are therefore used in energy harvesting applications, i.e. mode 31 and mode 33 [8, 160].

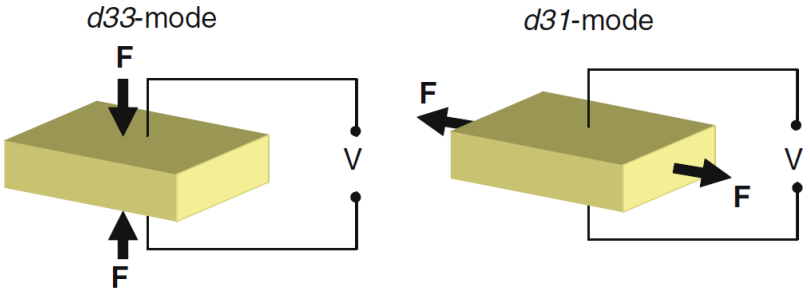

Figure 2.4. Illustration of the two piezoelectric modes typically utilized in EH [160].

These two modes, illustrated in Figure 2.4., differ in the way in which force is applied in relation to the poling direction, i.e. in the 31 mode the force is applied perpendicular to the poling, e.g. that of a cantilever based PEH under a bending load (Figure 2.3i), while in the 33 mode the force is applied in the poling direction, e.g. that of a piezoelectric stack harvester under a compressive load (Figure 2.3j) [160]. The most commonly used piezoelectric devices type, em-

ployed in EH applications, is a bimorph cantilever, comprising two layers of piezoelectric material using the 31 mode, attached to a typically metallic substrate. Such a structure, illustrated in Figure 2.5., is clamped at one (the excited) end, while the free end oscillates freely. A tip (proof) mass can be attached to the free end in order to tune the device's eigenfrequency to a specific ambient excitation, as well as to amplify deformations, and, thus, increase the generated voltage. Electrodes are fitted to both sides of the piezoelectric layer, allowing the utilization of the generated voltage [97, 160].

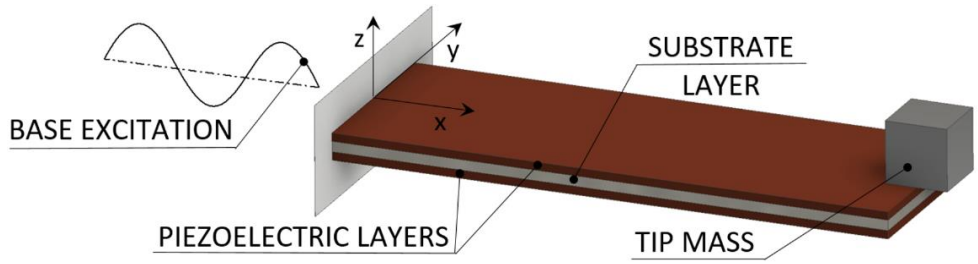

Figure 2.5. Illustration of bimorph PEH with a tip mass [71].

The electrodes attached to the piezoelectric layers of a bimorph are commonly connected to an electrical load in two ways, i.e., in parallel or in series (Figure 2.6.). When the two piezoelectric layers are poled in opposite directions, i.e., an electric field is applied across the complete thickness of the bimorph, the electrodes are connected in series. The parallel connection is, in turn, used when both piezoelectric layers are poled in the same direction, i.e., the electric field is applied individually to each of the layers [55, 163]. The piezoelectric layers of the herein considered harvesters are connected in parallel, in order to achieve a low-output impedance, typically required for electric circuits, as a serial connection results, in turn, in a high-output impedance [160]. When the clamped base of the PEH is subjected to harmonic excitation, i.e., when a sinusoidal external force of a certain frequency is applied to it, the structure of the PEH is deformed, strain occurs inside the piezoelectric layers, and voltage is generated [89, 97]. As the mechanical deformation affects the electrical properties of the piezoelectric layers, due to the piezoelectric (electromechanical) coupling, a backwards coupling effect also occurs within the piezoelectric layers, i.e. the influence of the generated voltage on the mechanical properties of the material [55, 97, 160]. This, in turn, results in the shifting of the device's eigenfrequency, i.e. coupled eigenfrequency, f_{coup}, Hz, away from the purely mechanical value, i.e. uncoupled or mechanical eigenfrequency, f_{mech}, Hz, when connected to a resistive load, due to the stiffening of the piezoelectric material, caused by the backwards coupling effect [25, 55].

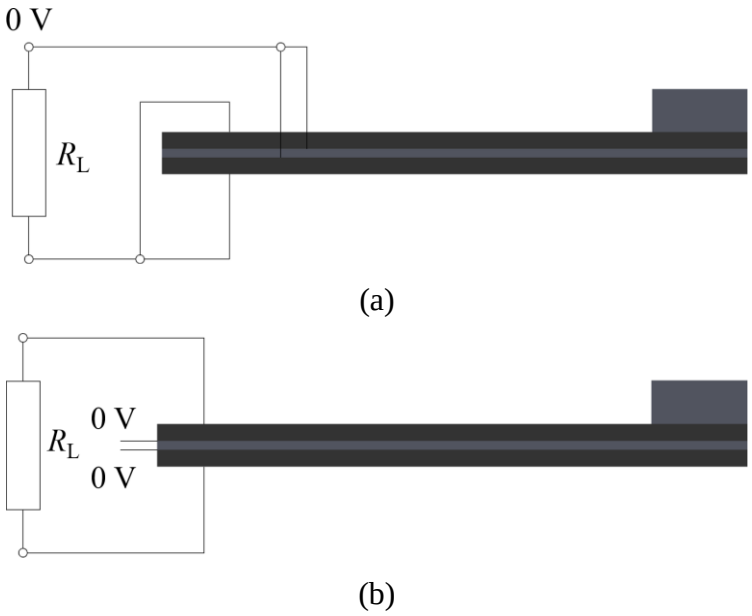

Figure 2.6. Parallel (a) and serial (b) electrical connection of a piezoelectric bimorph [71].

The conversion efficiency of the cantilever PEH, defined as the ratio of the generated electrical power and the power coming from the mechanical vibrations [100, 222], increases as the excitation frequency approaches its coupled eigenfrequency, with the maximum voltage being generated in a narrow band around that exact frequency value. It should be noted that the here considered coupled eigenfrequency significantly differs from the purely mechanical eigenfrequency due to the effects of electromechanical coupling on the response of the structure [68, 97, 160]. A typical response, i.e., voltage output, of a PEH bimorph subjected to a harmonic base excitation is shown in Figure 2.7. Piezoelectric energy harvesters represent the prevalent solution for kinetic energy harvesting, mainly due to a high energy density in comparison to the majority of the other EH approaches [16]. What is more, they are characterised by simplicity and a relatively high conversion efficiency, i.e. ~ 50-90% [222], but also by the scalability, which offers a wide array of possible applications from micro- up to the macroscale [97, 160, 172, 177]. Another form of piezoelectric EH devices, common in recent research, is the macro-fibre composite (MFC). The MFC device is a composite material comprising piezo ceramic fibres encased in structural epoxy between two polyamide films and it is typically attached to a flexible vibrating structure [93, 124]. The narrow frequency band of optimal operation of a PEH around the coupled eigenfrequency embodies the main drawback for the integration of these devices into wearable technologies as primary power sources, due to the random nature of human motion and the excitation it provides, which will be the focus of the subsequent subsections.

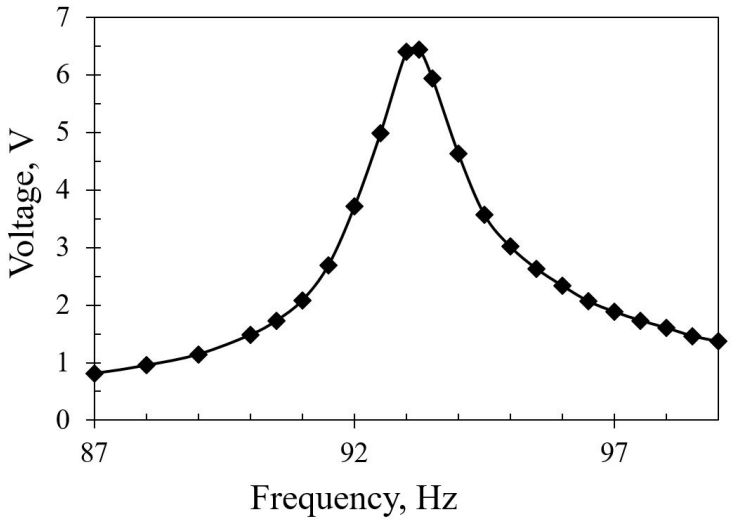

Figure 2.7. Typical response of a cantilever PEH subjected to harmonic excitation [71].

2.2.2. Issues with wearable PEHs and human motion excitation

Numerous studies have covered the subject of the energy available from the human body, mostly focusing on two basic energy forms, i.e., thermal energy from body heat and kinetic energy from body movement or body processes such as breathing [17, 88, 110, 132]. In their work, In and Palacios [88] provide a comprehensive overview of the available energy forms as well as their potential magnitudes, covering both thermal and kinetic sources. As it can be observed in Table 2.1., kinetic energy sources, namely arm and foot movements, promise the highest power potentials for energy harvesting, i.e., a theoretical maximum of around 60 - 70 W, which demonstrates a significant advantage of collecting kinetic energy from human movement compared to using energy from body processes or body heat [88].

Table 2.1. Potential power levels available from the human body [88].

Energy source	**Energy form**	**Available power**
Body heat	Thermal	2.4 – 4.8 W
Blood pressure	Kinetic	< 0.93 W
Arm motion		< 60 W
Footfalls		< 67 W
Finger motion		6.9 – 19 mW
Breathing band		< 0.83 W
Exhalation		< 1 W

Collecting the energy from human motion and converting into electrical energy represents, hence, a viable approach to the use of the energy from the human body as a power source for wearable devices, in the form of vibrations or impacts [88, 132]. While providing a copious and

easily usable source of kinetic energy, human motion is, however, characterized by random and chaotic movements, and, therefore, when collected and converted using piezoelectric energy harvesters, results in a random excitation [17].

Human motion data has been widely studied in literature and it encompasses the most common ADLs such as walking, climbing the stairs, running, daily hygiene activities etc. [50, 57]. The study conducted by Bai et al. has shown the random characteristics of human behaviour in ADLs, with vibrations and impacts occurring at frequencies from $f \sim 0.5$ up to 10 Hz [17]. From the data provided on an "as is" basis through EnABLES, a project funded by the EU H2020 Infrastructure Programme (H2020-INFRAIA-2014-2015) under the Grant Agreement 730957, it can be observed that the maximal acceleration values during most ADLs are ~ 1 g [57]. A study carried out at the Precision Engineering Laboratory of the University of Rijeka, Croatia, Faculty of Engineering [200], measured the acceleration values during several ADLs over a period of time using a smartphone integrated accelerometer attached at the wrist area of the subject [118]. An example of the thus measured data is shown in Figure 2.8., displayed in the frequency domain. As it is shown in Figure 2.8., the frequency values of vibrations and impacts from human walking are at around 1 and 1.8 Hz, with accelerations of ~ 0.1 g. When running is considered, the values of ~ 1.3 and ~ 2.6 Hz, with accelerations of ~ 0.7 g, are recorded, showing an expected increase in magnitude.

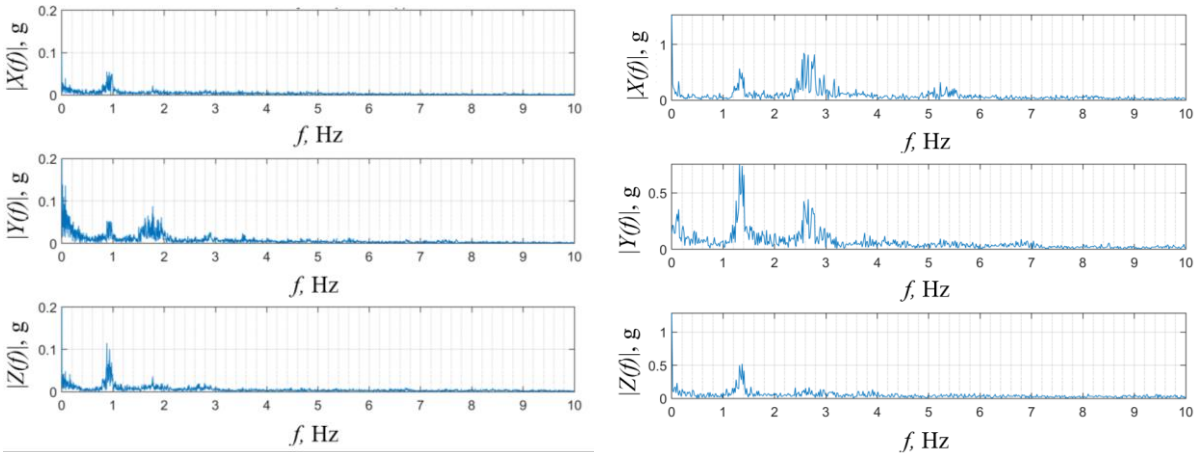

(a) (b)

Figure 2.8. Frequency spectrums of ADL accelerations: walking (a) and running (b) [118].

The ADLs of hand washing and teeth brushing, reported in [118], display, in turn, similar frequency and acceleration values, ranging from ~ 1 to 4 Hz and ~ 0.1 to ~ 0.3 g, respectively. The similarity can be caused due to the fundamentally similar repetitive motion during both activities. Finally, the activities of eating and using the PC show relatively low acceleration

values from 0.05 to ~ 0.2 g at frequencies below 1 Hz [70, 118, 200]. These results coincide with the aforementioned studies.

The random nature of human motion excitation, in combination with the inherent drawback of a piezoelectric bimorph energy harvester, results in less than optimal operation of the PEHs and reduced conversion efficiency, i.e., a smaller generated power per unit of volume or surface of the device. Numerous approaches aimed towards solving this issue, i.e., attempting to widen the optimal operating frequency spectrum of PEHs, have been suggested in recent literature [62, 92, 198, 216, 230]. The most promising among them can be classified in three major categories [69]:

- **changing the boundary conditions at the cantilever free end**, i.e., active tuning and damping control methods [30, 162, 179],
- **changing the cantilever geometry**, i.e., shape optimization, using several differently tuned cantilevers or complex geometries with bi-stable or nonlinear responses [7, 22, 86, 107, 161], and
- **frequency up-conversion** (FUC), i.e., impacting or plucking the cantilever free end and letting it oscillate at its respective eigenfrequency [76, 96, 103, 217].

An innovative design approach, combining geometric variations and optimization, as a crucial design parameter of PEHs' dimensioning, and a frequency up-conversion excitation mechanism, is considered in this work, and will be explained in detail in the following sections.

2.2.3. Frequency up-conversion mechanisms

The mechanism of frequency up-conversion (FUC) provides a viable method for turning random and chaotic vibrations into periodic motion aimed at PEH excitation. Two major mechanism types commonly found in literature are impact and plucking [4, 62]. The impact FUC mechanism, two examples of which are shown in Figure 2.9., typically comprises a moving or rolling mass, subjected to random ambient excitation, which impacts a piezoelectric beam or cantilever [60, 210]. By applying load to the PEH, the impacting mass provides the excitation of the device, which is then left to oscillate at its eigenfrequency, thus operating in the optimal conversion conditions, as well as at its maximal efficiency [58, 77]. On the other hand, the method of plucking consists of a moving plectrum that deflects the free end of the PEH by applying load from the moment of contact until the plectrum detaches from the PEH, releasing the tip of the cantilever and thus ensuring the free vibration of the device [63, 96]. A simplified depiction of the process can be seen in Figure 2.10.

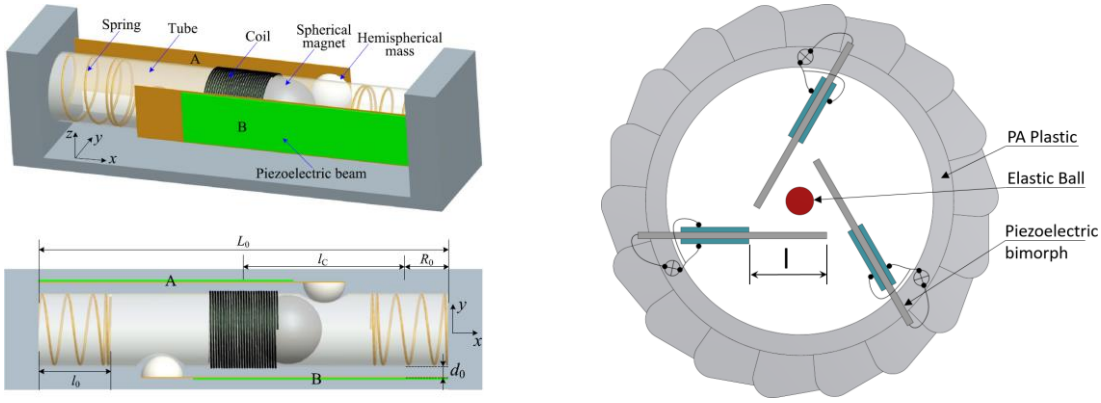

(a) (b)

Figure 2.9. Examples of impact FUC mechanisms: hybrid EM-piezoelectric vibration energy harvester (a) [58], and rotational PEH (b) [221].

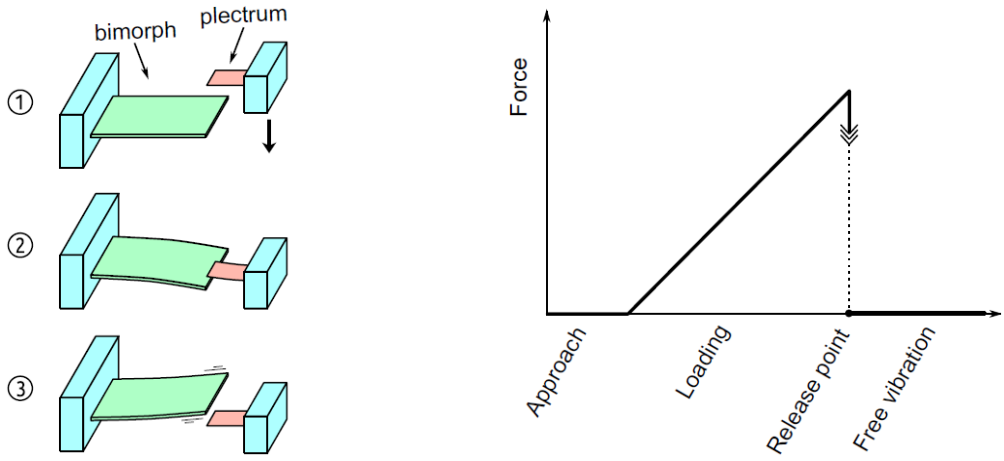

a) b)

Figure 2.10. Illustration of the plucking mechanism steps (a), and graphical depiction of the plucking load (b) [157].

The motion of the plectrum can be either linear or rotational, depending on devices' design as well as the type of harnessed motion. A sliding mass provides, therefore, the linear motion of the plectrum, while, more commonly used in literature, the rotating motion is generated via a counterweight flywheel [33, 76, 112, 229]. The rotational flywheel-based FUC mechanism appears to be, according to available literature, a suitable candidate for wearable applications, if integrated in a watch-like device with careful design considerations [33, 112]. In both the sliding and rotational mechanisms the excitation can be achieved via opposed magnets, rather than by mechanical contact, i.e. magnetic impact or magnetic plucking [62, 154, 215, 217].

2.3. State-of-the-art in piezoelectric energy harvesting, geometry optimization and FUC mechanisms

As it was mentioned in the previous sections, a combined approach to overcoming the issues intrinsic to bimorph PEHs, evident when integrated into wearable technologies, will be used in this work. For that purpose, a detailed review of the state-of-the-art of both PEH geometry variation as well as of frequency up-conversion, with an emphasis on wearable applications, will be given in this subsection. In their seminal work in 2005, Priya et al. introduced the piezoelectric windmill, depicted in Figure 2.11a, one of the first mechanisms that utilize plucking as PEH excitation [159]. The device consists of a rotating hub with teeth, powered by a small wind turbine, which was used to "pluck" ten radially placed PEH rectangular cantilevers. The windmill was able to generate 7.5 mW of power at a wind speed of 4.5 m/s. The strength of the piezoelectric material exposed to dynamic loads was, in turn, not considered [159]. Moro and Benasciutti suggested in 2010 a shoe-mounted rectangular PEH tuned with a tip mass and excited via base impacts caused by walking [136]. The device produced ~ 400 μW of power when equipped with a 16.4 g tip mass. Although the authors did consider the stress of the piezoelectric materials, it remains a highly unpredictable value, since it is dependent on the random nature of excitation acceleration from human motion and the dynamical impact on the device itself (especially the piezoelectric layers). Gu and Livermore proposed in 2011 a frequency up-conversion approach using a spring-type cantilever with a tip mass as an impact mechanism providing excitation to a piezoelectric harvester [76]. The spring cantilever collects random vibrations from the environment and transfers them periodically to the PEH. The power output of ~ 450 μW generated by the device was shown to be a performance improvement over a reference PEH, subjected to harmonic excitation. In 2011 Pozzi and Zhu developed a knee-mounted mechanism aimed at utilizing the relative movements of the leg during walking, i.e., the flexion and extension of the knee, as illustrated in Figure 2.11b [157]. The device comprises an outer rotating ring equipped with plectra and an inner hub with PEHs attached to it, i.e., an inverted piezoelectric windmill. The relative movement of these two components allows the plucking of the PEHs. The low power output of the device was improved in the authors' later work from 2012, where a 2 mW power output was measured over a full cycle of gait [156]. An upgraded device with magnetic plucking was presented by the authors in 2016 [155]. Janphuang et al. studied in 2013 the efficiency of a PEH subjected to impact excitation, which was provided via a toothed flywheel with the teeth impacting a tip below the PEH free end [91]. They concluded that the conversion efficiency in terms of voltage output increases with the rotational speed of

the flywheel.

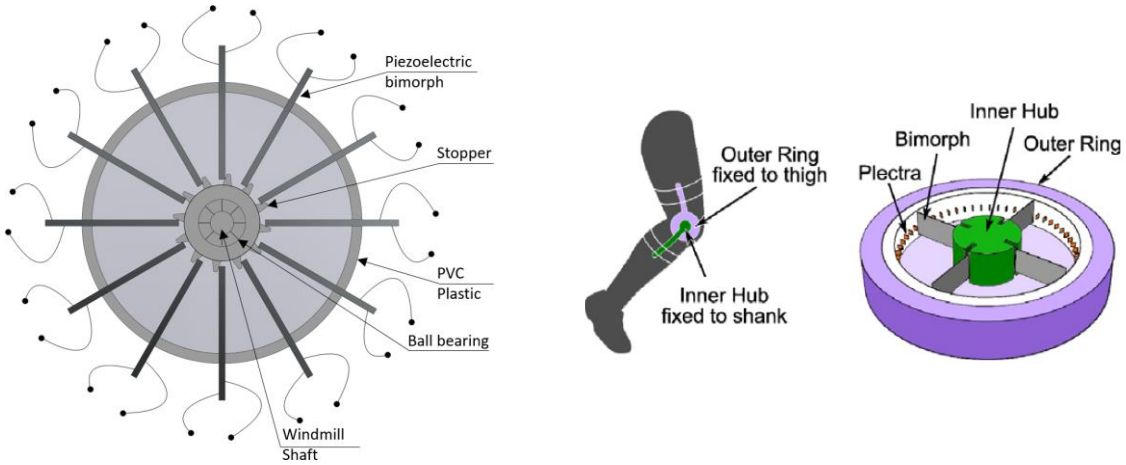

(a) (b)

Figure 2.11. Approaches to kinetic EH: piezoelectric windmill [159] (a) and the knee-mounted plucked PEH [156] (b).

The power levels are not given, and there are no PEH layer strength considerations. In 2014 Pillatsch et al. proposed a device, worn on the upper arm, comprising a rotating flywheel with a plectrum and a single rectangular PEH (Figure 2.12a) [154]. The flywheel collects the random excitation from human motion and translates it into a periodical plucking of the PEH using opposing magnets. During continuous flywheel rotation, the device produces 40 μW of power, while in real-life conditions, i.e., when running, the power levels drop down to ~ 7 μW. These power levels are given without any consideration of the piezoelectric material strength. Lockhart et al. developed in 2014 a miniaturized wrist-worn device that consists of a rotating flywheel with 200 μm pins on the inner part [112]. The rotating pins mechanically pluck four radially mounted rectangular MEMS PEHs, generating 11 μW of power under continuous plucking conditions, without considering material stress, and with a significant drop in performance (~ 6 μW) when the rotation frequency varies. The authors also provide comprehensive guidelines for wrist-worn flywheel design. Despite the numerous benefits of a miniaturized design regarding wearable applications, the size of the device reflects negatively on its performances, making its practical use, i.e., the powering of autonomous wearable devices, rather difficult. In their work from 2017, Xue and Roundy analysed the various magnet orientations in a flywheel-type FUC setup and their effect on PEH performances. The best results were found to occur when the magnets are positioned in the same plane (in-plane plucking configuration), as well as when they are set at a slight offset (out-of-plane indirect configuration). In both cases the magnets are positioned in a repulsive arrangement [218]. These findings were later included in the design of a wrist-worn EH device (Figure 2.12b), comprising a rotating

flywheel magnetically plucking a number of thin film sputtered PEHs. Under sinusoidal excitations, the device was able to generate a relatively low power of 40 μW, without considering the stresses of the PEHs [219].

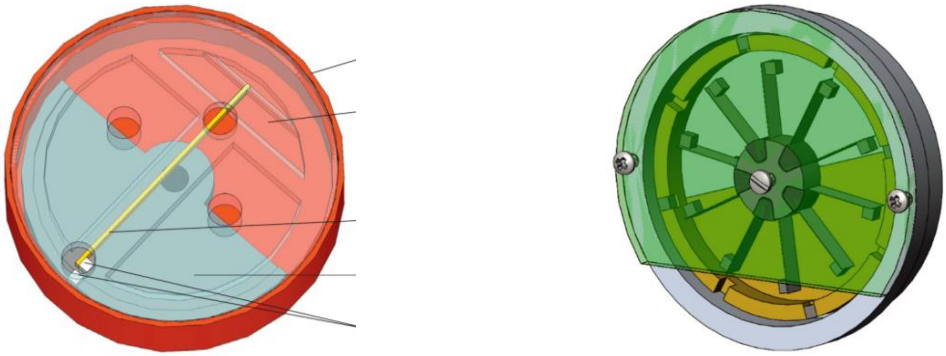

(a) (b)

Figure 2.12. Approaches to kinetic EH: a magnetically excited PEH with rotating flywheel [154] (a) and a wearable device with magnetically plucked thin film PEHs [219] (b).

Kathpalia et al. studied in 2018 in detail the plucking mechanism [96]. They analysed the effects of plectrum thickness and overlap on the initial deflections and the plucking force, as well as on the average power output of the PEHs, and developed an experimentally validated analytical model describing the process, focusing on the nonlinearities of the compliant plectrum. Fu and Liao took, in 2019, a different approach to the modelling of the plucking mechanism [63]. The load was modelled in this case as an infinitely large mass impacting the piezoelectric beam. The plucking was also compared to a transversal impact on the surface of a piezoelectric beam in terms of force application within a unit of time. Both works offer a deeper understanding of the plucking mechanism and provide valuable insights for the development of FUC-based devices. Izadgoshasb et al. proposed in 2019 an innovative device, displayed in Figure 2.13a, comprising a double pendulum mechanism for leg movement EH [90], albeit providing a viable approach and showing promising performances (~ 2 mW). The proposed solution uses a relatively complex motion mechanism. Furthermore, the force acting on the PEH is directly linked to the intensity of random human motion, and, without the inclusion of a stress analysis, the long term use of such a device remains questionable. An interesting study was carried out by He et al. in 2020, concerning the orientation of the magnetically plucked PEH with respect to the exciting magnet plane of rotation (Figure 2.13b) [81]. The study included the variation of the PEH installation angle from 0° up to 60° in order to utilize multimode coupled vibrations. The best results in terms of voltage and power output, were observed at an installation angle of 60°, thus showing the viability of such an approach. Febbo et al. proposed in 2020 an impact driven PEH, consisting of a moving mass affixed on a spring-type cantilever,

impacting a cantilever with an MFC patch [60]. The C-shaped end of the moving mass, is designed in such a way to impact the MFC cantilever on its up and down swing. Despite being able to generate a reasonable 180 μW of power, the relatively crude and bulky device could benefit from a number of improvements.

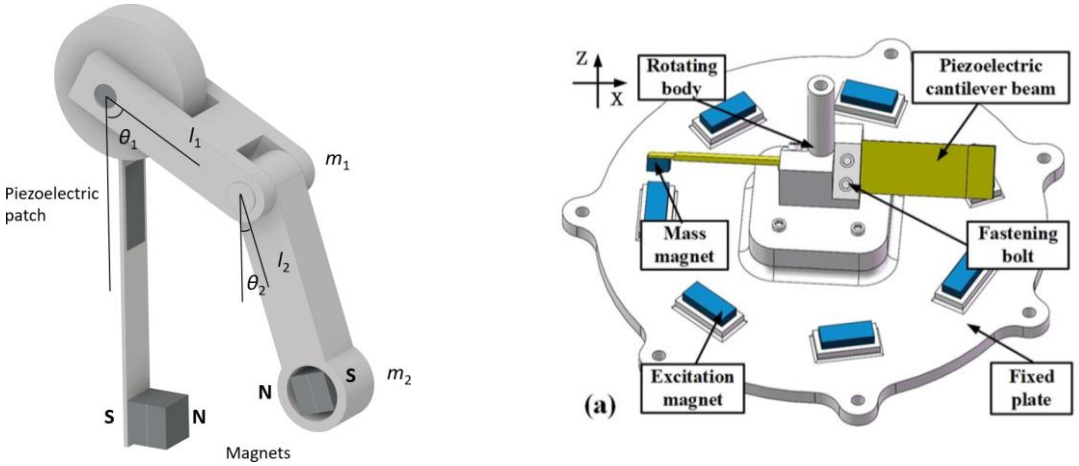

(a) (b)

Figure 2.13. Approaches to kinetic EH: double pendulum wearable EH device [90] (a), PEH installation with angle variation [81] (b).

In their work from 2021, Peng et al. used a combination of stack PEHs equipped with a force amplifier and a FUC mechanism [151]. The FUC mechanism was shown to increase the power output up to ~ 170 times compared to the same harmonically excited PEH, thus achieving a power output of 320 mW. Regardless of its good performances, the rather bulky design of the overall device makes it somewhat unwieldy for wearable applications. Lo et al. investigated in 2021 the effects of mixed resonant modes on the PEH response by utilizing a two-point magnetic plucking mechanism (Figure 2.14a) and noticed significant voltage gains over a wider frequency band [111].

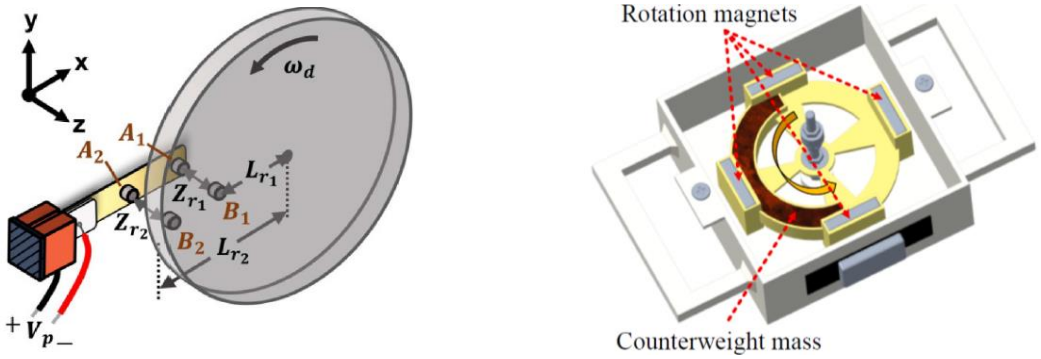

(a) (b)

Figure 2.14. Approaches to kinetic EH: PEH utilizing mixed resonant modes [111] (a), and a hand-held EH device using magnetically bent piezoelectric beams [19] (b).

An innovative approach to PEH excitation was, finally, suggested by Bao et al. in 2021, as part of a hand-held EH device, displayed in Figure 2.14b [19]. Magnets attached to a rotating flywheel interact here with stationary magnets positioned in the middle of radially arranged piezoelectric beams clamped at both ends, thus magnetically exciting the PEHs. The device, still in an early development phase, is relatively bulky, and, along with a low power output of 0.18 μW, in need of significant improvements if it is to be utilized for wearable EH.

Concerning the variation of geometrical parameters of PEH devices, in 2010, Benasciutti et al. studied the behaviour of PEHs with optimized shapes, both trapezoidal, i.e. clamped by the wider end, as shown in Figure 2.15a, as well as inverted trapezoidal, clamped by the narrow end, devised in order to create a more uniform stress distribution along the cantilever [22]. In both cases, the optimized shapes had a width comparable to the reference rectangular device. The authors have shown that the performance of optimized PEHs, subjected to harmonic excitations, is significantly improved when compared to a comparable rectangular PEH of comparable width and working at the same eigenfrequency, i.e., that, in terms of specific power output (power output normalized over the device's volume) the inverted trapezoidal PEH provides an improvement up to a 113% compared to the rectangular device. The improvements were attributed to a better stress distribution across the optimized shapes, which resulted in an increased voltage, and thus power output. While this optimization approach demonstrated the possibilities of considerable PEH performance improvements, while maintaining the simplicity of design and manufacture, further improvements could be achieved by introducing additional optimization criteria, thus utilizing more of the limited volume available in wearable devices. A more complex optimized geometry was suggested in 2012 by Park et al., applied to a PVDF energy harvester (Figure 2.15b) [150]. The authors achieved considerable power gains in relation to the reference rectangular device, particularly when the shape optimization algorithm was not limited in terms of surface area. Relatively low μW range absolute power outputs were achieved, while only tensile strength was considered, which strongly limits the application, as well as the durability of such a device, subjected to dynamical working conditions. As in the case of Benasciutti et al., the space available for the PEH is not fully utilized. Leadenham and Erturk experimented in 2015 with a different spatial orientation of the PEHs [107]. The authors studied a nonlinear M-shaped device, clamped at two ends with two piezoelectric patches, aimed at very low acceleration (< 0.1 g) applications, using both primary and secondary resonances in order to broaden the operation spectrum. A ~ 600% increase in the half power bandwidth was achieved with this rather complex mechanism without stress considerations. Li et al.

suggested in 2020 an L-shaped structure comprising two PEHs, utilizing both bending and torsion, i.e. mode 31 and mode 36 [109].

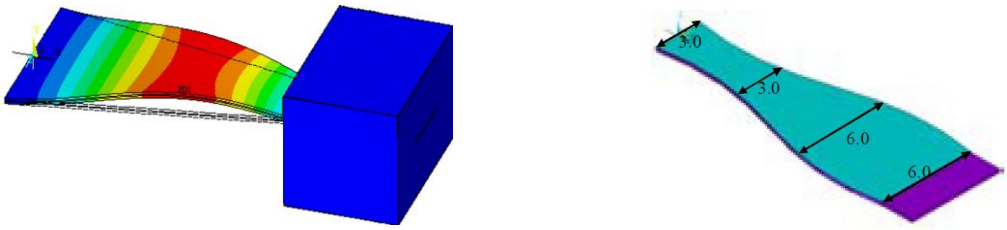

(a) (b)

Figure 2.15. PEH geometry alteration approaches: trapezoidal shape [22] (a), complex optimized geometries [150] (b).

The device was able to generate a power output in the μW range at low excitation frequencies, which, while making the device suitable for wearable applications in terms of excitation conditions, is still relatively low for powering wearable electronics. Although being an interesting and promising approach to piezoelectric EH, due to its limited performances, its complexity and the lack of a material strength analysis, the proposed solution requires additional studies and improvements. The topology optimization (TO) approach, in terms of thickness, was applied to the layers of a PEH by de Almeida and Pavanello in 2018 [7]. The variation of volume percentages, in combination with different materials, provided an interesting insight into layer's geometry, but resulted in an overly complex topology of an already thin PEH feature. This complexity could, in turn, reflect on the manufacturing process and, particularly, on the durability of the device, considering especially that no stress analysis has been performed. Homayouni-Amlashi et al. applied the TO method to the surface of a rectangular PEH clamped at one corner with a tip mass placed on the opposite one [84]. Two optimized designs were developed, both displaying noticeable voltage gains. However, no study of the dynamic stresses occurring in such complex geometries and no power output values are presented, which limits the understanding of the potentials of this promising approach. Biswall et al. investigated in 2021 the effects of a rectangular hole in a MEMS PEH cantilever on the performance of the device [24]. The authors varied and optimized the size and the position of the hole, as it can be seen in Figure 2.16a, which resulted in an improved performance of the studied PEH, and a maximum specific power output of ~ 24 $\mu W/mm^2$ was reported. The increase in performances proves the validity of the suggested approach. Masara et al. conducted, finally, in 2021 a theoretical study considering the segmentation of a rectangular PEH into three separate ones, operating at different eigenfrequencies due to the different respective lengths (Figure 2.16b) [121]. The performance in terms of the power outputs of all the three segments combined (~ 300 mW),

was found to be improved when compared to similar devices reported in available literature.

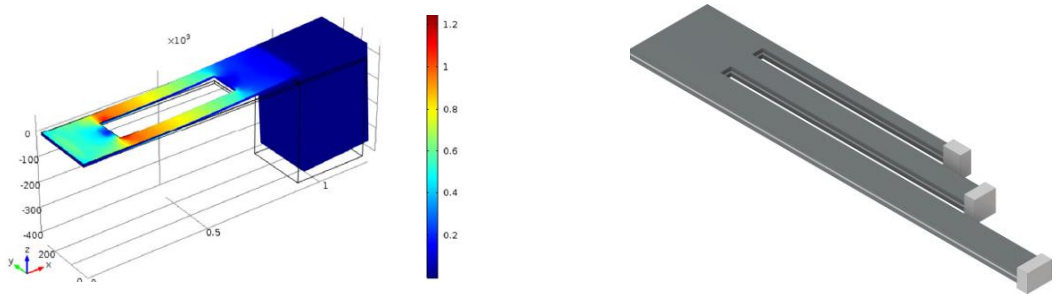

(a) (b)

Figure 2.16. PEH geometry alteration approaches: a MEMS device with optimized holes [24] (c) and a harmonically excited segmented PEH [121] (b).

Since the stress levels of the piezoelectric layers are not considered, the substantial power output levels reported in this work, while showing ample potential for powering wearable devices, should be taken with due discretion.

This section introduced wearable technologies as well was presented the basic principles of energy harvesting, with particular attention given to the piezoelectric approach applied to human motion energy harvesting. The issues innate to piezoelectric bimorph energy harvesters, caused by random excitation from human motion, were discussed. Two main approaches to solve these issues were presented, i.e., the frequency up-conversion and geometry optimization, and a thorough and comprehensive overview of the state-of-the-art in both these fields of research was given. After a careful consideration of the aforementioned methods, and particular attention dedicated to the design and operational simplicity, an innovative path comprising a combination of frequency up-conversion, geometry optimization and PEH segmentation was selected in this work. The synergy of these three methods of PEH design, employed separately in previous art, representing an original approach to PEH design, could bring forward their combined benefits, with the goal to develop an improved miniaturized energy harvesting device optimized for wearable applications. The proposed device will comprise a rotating flywheel with several plectra collecting the random ambient excitations generated by human motion and it will provide a periodical excitation for a number of PEHs optimized for maximum specific power output.

The next section will provide a comprehensive overview of electronic components, mostly commercially available, and commonly utilized in wearable applications. The basics of EH power management, with particular attention to wearable medical applications, will be covered and an example of an autonomous wearable device will be described.

3. ANALYSIS OF THE TYPICAL ELECTRONIC COMPONENTS EMPLOYED IN WEARABLE BIOMEDICAL APPLICATIONS

A wide range of electronic components and subsystems form the basis of a wearable device. Typically, as shown in Figure 2.2., these include one or several sensors, a signal processing unit, usually combined with memory storage elements, wireless communication components, as well as a power supply unit including an energy storage element. When medical applications are considered, such as those foreseen for remote health monitoring and telemedicine applications, commonly used sensors comprise accelerometers [147], i.e., fall detection [228], temperature sensors [126, 131], heart rate [11, 167], blood pressure [174] and glucose monitors [66], while a number of different signal processors, memory storage and communication modules can be combined to achieve the desired functionality of the device. A comprehensive overview of these sensors, as well as of some additional sensor types and components, will be provided in this section together with their respective power requirements, offering a guideline for the development of autonomous wearable devices, powered by optimized EH systems[1].

3.1. Sensor components

Within the wide field of medical applications, numerous combinations of sensors are used for specific wearable devices. Within this subsection, several categories of commonly used sensors, namely accelerometers, temperature sensors, heart rate monitors, blood pressure monitors, blood glucose monitoring systems and pulse oximeters will be analysed, and their respective power requirements and operating voltage will be summarised.

3.1.1.Accelerometers

Accelerometers are sensors designed to measure linear acceleration, i.e., the change in velocity per unit of time, and are typically employed to determine shock, falling and orientation [53], but also inclination and vibration information [166]. They are being increasingly utilized

[1] Part of the work described in this section was published by the author of the thesis and his collaborators in a peer-reviewed scientific paper [71], produced and published as part of the obligations foreseen in the curriculum of the doctoral study of the Faculty of Engineering of the University of Rijeka, Croatia, and hence this section is based, partly directly derived and cited from this work.

for device position and orientation detectors - as components of portable, handheld and wearable electronic devices, e.g. smart watches, phones, tablet PC and video game controllers [53]. Such accelerometers are able to measure the acceleration of a system in all three axes, as well as to identify the direction and magnitude of the measured acceleration as a vector, while the output signal can either be analogue or digital [53]. In the frame of wearable technologies, accelerometers are typically used in the low-*g* MEMS integrated circuits (ICs), and are generally based on piezoelectric or capacitance operating principles, examples of which can be seen in Figure 3.1. [166].

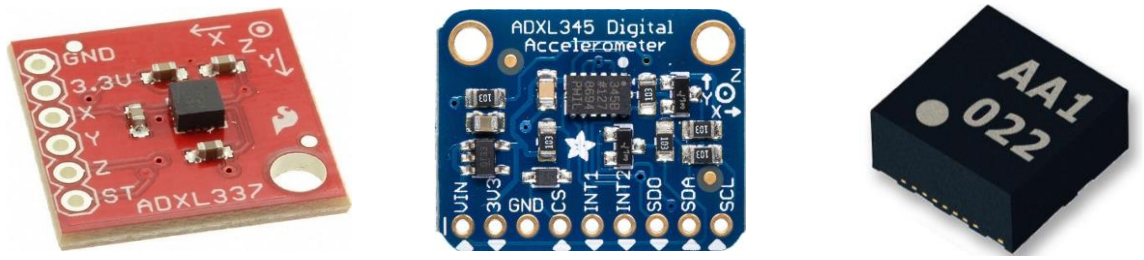

(a) (b) (c)

Figure 3.1. Examples of commercially available accelerometers: ADXL337 analogue accelerometer [43] (a), ADXL345 digital accelerometer [47] (b), and KX022 tri-axes accelerometer [158] (c).

Piezoelectric accelerometers comprise microscopic piezoelectric structure, which, when subjected to stresses caused by ambient accelerative forces, generate voltage [53]. Devices using capacitance contain two microstructured plates placed next to each other. Their relative movement, induced by an accelerative force, causes a change in the capacitance, which is then converted into voltage via additional processing circuitry, typically integrated on the accelerometer chip [53]. In terms of voltage, commercially available MEMS accelerometers, typically operate between 1.8 and 3.6 V [108, 181], while, when power requirements are considered, the values vary between ~ 300 μW for the digital, and up to 900 μW for the analogue variants [147]. Special versions, allowing for a low power operating mode are also available, e.g. the KX022 tri-axis accelerometer, with a 36 μW low power mode [167]. Such low power devices could, in turn, represent a viable option for wearable applications, where the available power is limited, and the overall power requirement of the device should be kept at a minimum.

3.1.2.Temperature sensors

Most conventional devices aimed at temperature measurement operate through the transfer of heat from a source to the device, where a suitable transducer converts the chemical or phys-

ical change into a measurable signal [181]. The commonly used thermocouples detect the voltage caused by the electron configuration change at a junction created by joining two dissimilar conductive materials, i.e., via the thermoelectric (Seebeck) effect. Several types of thermocouples are commonly in use, e.g. type J, K or E, comprising different junction materials pairs, and, thus, aimed at different applications based on the involved temperature range, the sensitivity or the response speed [181]. Another approach to temperature measurement are resistance temperature detectors (RTDs), i.e., temperature sensors utilizing the thermoresistive properties of particular metallic materials, e.g. platinum, nickel and copper. The temperature of an object is determined in this case by measuring the change in resistance of a thermoresistive metallic element exposed to said temperature. At elevated temperatures of ~ 800°C, RTDs display a lower measuring accuracy compared to thermocouples, which is of lesser importance within the frame of wearable applications, particularly in the field of medicine [181]. Thermistors are, in turn, robust temperature sensors that use the thermoresistive properties of metallic oxides, e.g. cobalt, chromium or nickel oxides, i.e., the negative resistance change of an exposed element, typically detected via a bridge circuit. When compared to RTDs, thermistors exhibit a faster response and a higher sensitivity [181]. The temperature dependency of the resonant frequency of single crystals (such as e.g. SiO_2) represents the operating principle of resonant temperature sensors. The high accuracy and precision of this physical phenomenon results in particularly precise temperature sensors, able to detect fairly small changes in temperature [181]. Commercially available miniaturized, i.e., less than 2 mm x 2 mm in size, temperature sensors are generally thermocouple based IC devices, some examples of which can be seen in Figure 3.2. The operating voltage requirements of these devices range from 1.7 V up to 5.5 V [126, 131, 167]. In terms of power consumption, the commercially available devices shown in Figures 3.2a and 3.2b require ~ 40 to ~ 80 μW [180-181], while a significantly higher power need is innate to the MAX30208 device (Figure 3.2c), which also provides a clinical measurement accuracy and it is classified as a "clinical grade wearable sensor" [126].

(a) (b) (c)

Figure 3.2 Examples of commercially available miniaturized IC temperature sensors: BD1020HFV [137] (a), MCP9700 [131] (b), and MAX30208 clinical grade sensor [137] (c).

3.1.3.Heart rate monitors

The use of portable heart rate (HR) monitors started in the late 1950s, and they have since become essential tools used in clinical, diagnostic as well as prognostic medical practice in the frame of cardiovascular diseases [175]. Along with clinical applications, HR monitors are increasingly being used to study the body response to stress due to training or exercise, aiding in training level evaluation for athletes, as well as spreading to everyday use through consumer wearable electronics [175]. The most common technologies used for non-invasive HR monitoring are listed and described next in this subsection.

Electrocardiography (ECG) is a technology using biopotential in order to detect the heart's electrical activity, i.e., the surface potentials, observed on specific thorax locations, generated by local electrical dipoles, induced by periods of respective electrical depolarization and repolarization, connected to the contraction and relaxation cycles of heart cells [175]. The generic expression used for HR is beats-per-minute or bpm, and it is obtained from heartbeat intervals in milliseconds [175].

Phonocardiography (PCG) is an electric-acoustic approach measuring and analysing the sound of heartbeats. The heartbeat intervals and, in turn, the HR is estimated by detecting the characteristic sound generated by closing of the atrioventricular valves inside the heart [175].

Photoplethysmography (PPG), represents a HR monitoring approach that employs optical technology to measure the propagation of light inside the tissue during a cardiac cycle. This technology also allows the measurement of blood oxygen saturation, i.e., pulse oximetry, by using light of two different wavelengths to estimate the absorbance of arterial blood [165, 175]. A large number of commercially available miniaturized HR monitoring devices operate on the PPG principle [175], some of which are shown in Figure 3.3.

(a) (b)

Figure 3.3. Examples of commercially available miniaturized HR monitoring components: MAX30102 [137] (a) and BH1790GLC [167] (b).

The two IC components MAX30102 and BH1790GLC operate at similar voltage ranges, i.e., 1.8 – 3.3 V and 1.7 – 3.6 V respectively [126, 167], with no voltage data available for the

component used within the Samsung Galaxy Gear Neo 2® smartwatch with comparable functionality [11]. The HR monitoring component used by Samsung® displays a significantly higher power requirement, i.e., ~ 50 mW, when compared to the two IC components MAX30102 and BH1790GLC, requiring less than 1 mW of power to operate [126, 167], making the aforementioned IC components suitable for an autonomous wearable medical device.

3.1.4.Blood pressure sensors

Increased blood pressure or hypertension is a medical condition manifesting as chronic and sustained elevation in arterial blood pressure. It represents a significant risk factor for numerous cardiovascular diseases and, according to the World Health Organization (WHO) data, it affects over a billion people all over the world, [175]. The use of conventional automated oscillometric devices is not widespread in this frame among the general population, mainly due to their limitations in terms of cumbersome construction, i.e., the unsuitability for home use or night-time measurements, as well the inability to continuously measure blood pressure, which may, in turn, omit short term variations in pressure [175].

Numerous approaches to wearable blood pressure measurements have been studied in literature. The conformal ultrasonic device (Figure 3.4a) developed by Wang et al., aimed at continuous monitoring of the central blood pressure from deeply embedded vessels, e.g. the carotid artery and the jugular vein, is based on a combination of rigid piezoelectric and soft structural components [207]. The ultrathin (240 μm) device, composed of several transducers, displays comparable working characteristics to currently available medical ultrasonic sensors. Such an array of transducers is able to continuously measure the diameter of a pulsating blood vessel, which is, in turn, converted into waveforms and analysed. The power requirements for such a device, as provided by the authors, is ~ 24 mW, while no operating voltage data is given [207]. Gong et al. suggested a wearable and highly sensitive pressure sensor with ultrathin gold nanowires, displayed in Figure 3.4b [74]. Among other potential applications presented by the authors, the said device can also be employed for real-time blood pressure measurements through the detection of wrist pulses. The blood pressure values assessed by using the device have been validated via clinical data available in literature [74]. The device is reported to operate at 1.5 V and requiring less than 30 mW of power. Salo et al. proposed an approach to continuous extravascular blood pressure monitoring using a tactile complementary-metal–oxide–semiconductor (CMOS) sensor, shown in Figure 3.4c [174]. The pulsating pressure within the blood vessels results in a local displacement of the tissue surface, adherent to the tactile sensor membranes, which are deformed by it. The deformation of the membranes can thus be detected as a change

in capacitance and transduced into a usable signal. According to the authors, the utilized tactile sensor requires 11.5 mW of power and operates at 5V [174].

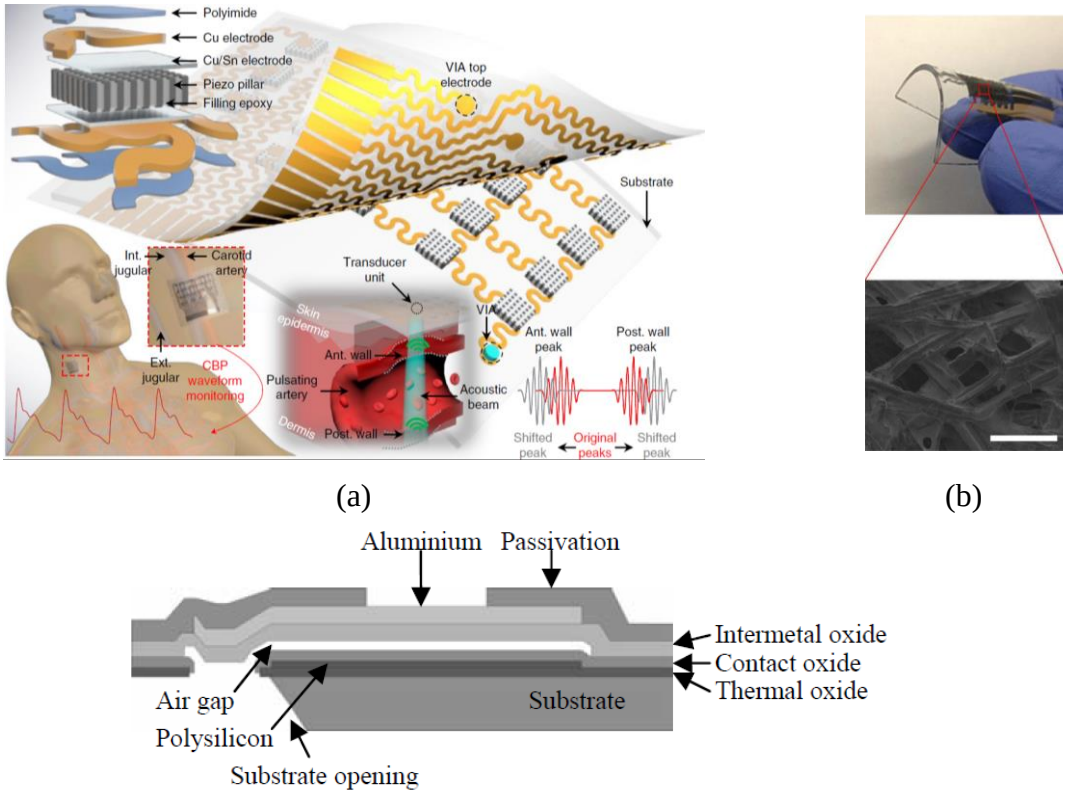

Figure 3.4. Examples of blood pressure monitoring concepts: the ultrasonic device developed by Wang et al. [207] (a), the Au nanowire pressure sensor designed by Gong et al. [74] (b), and the CMOS sensor suggested by Salo et al. [174] (c).

In addition to the above mentioned technologies, PPG based sensors, described in Subsection 4.1.3, that are part of standard clinical monitoring equipment, can also be employed to monitor blood pressure [175]. Two types of PPG blood pressure monitoring techniques can then be differentiated: pulse wave velocity (PWV) and pulse wave analysis (PWA). The PWV approach requires two separate sensors placed at different points on the human body, measuring the propagation speed of the blood pressure waves inside the arterial tree. PWA, on the other hand, operates using a single sensor, performing a morphological analysis of the blood pressure waveform [175].

3.1.5.Blood glucose monitoring systems

The continuous monitoring of blood glucose levels is essential in managing type 1 diabetes, a condition where the human body is unable to produce insulin and thus control the blood sugar level. By monitoring these values, a timely administration of insulin can thus be ensured, and

sugar levels kept within an optimal range [175].

Gia et al. studied the feasibility of an invasive and continuous real time glucose monitoring (CGM) system with an IoT-based approach [66]. The reported power requirement of the utilized sensor node operating at 2 V is 1 mW. The low power CGM contact lens developed by Hayashi et al., shown in Figure 3.5a, comprises a supply-modulated CMOS transmitter and a solid-state glucose fuel cell [80]. The fuel cell, besides providing the needed power, serves as the glucose concentration sensor, i.e., it increases the output voltage when the glucose concentration in the tears increases. This non-invasive CGM system operates at ~ 100 mV requiring less than 1 μW of power [80]. The implantable RFID CGM sensor tag, designed by Xiao et al. [214], displayed schematically in Figure 3.5b, uses an electrochemical sensor combined with radio-frequency identification (RFID) communication technology. The implanted sensor is able to generate a nA order current, depending on the glucose levels present in human blood, and it is powered via the RFID antenna using the RF EH principles. The glucose level values are, finally, assessed using an external RFID reader. The overall system operates at a voltage range from 1 to 1.2 V and consumes 50 μW of power [214].

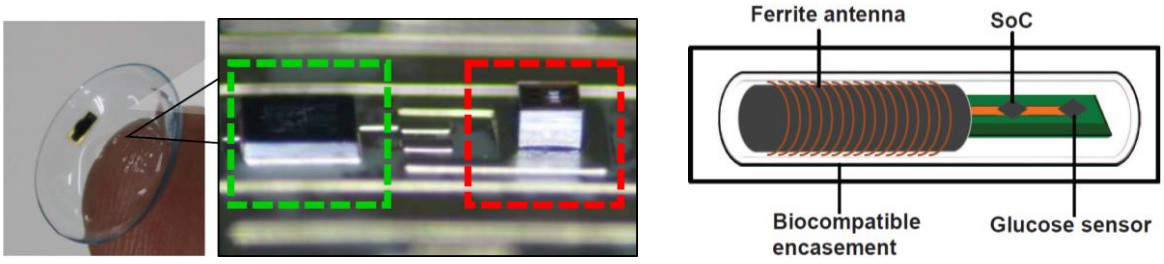

(a) (b)

Figure 3.5. Blood glucose monitoring systems: low power CGM contact lens developed by Hayashi et al. [80] (a) and the implantable RFID sensor tag suggested by Xiao et al. [214] (b).

3.1.6.Pulse oximeter sensors

Pulse oximetry represents a widespread non-invasive spectrometric method for the real-time assessment of gas content in arterial blood, typically based on the previously described PPG principle [175], providing early information regarding circulatory and respiratory issues, and allowing timely interventions. Generally, pulse oximeters are utilized in operating rooms, emergency, intensive, neonatal and paediatric care, as well as in sleep studies and veterinary applications [193]. The PPG approach includes the illumination of living tissue and capturing the propagated light via a photodetector. The subsequent analysis of the captured light provides information regarding the illuminated tissue [175]. Such an approach enables a non-invasive measurement of the oxygenated haemoglobin percentage present in patients' blood, achieved

via the comparison of the transmission characteristics of the red and the infrared LED lights passing through the patients' tissue [193]. Lee et al. designed a reflective patch aimed at organic pulse oximetry sensing with ultra-low power consumption, illustrated in Figure 3.6a [108]. This wearable device uses organic light-emitting diodes (OLEDs) as PPG light sources, as well as organic photodiodes as photodetectors and it was reported to operate in a 3.3 – 5 V voltage range, requiring 68 – 125 μW of power. Tavakoli et al. presented, in turn, an ultra-low power analogue pulse oximeter comprising a single chip, shown in Figure 3.6b [193].

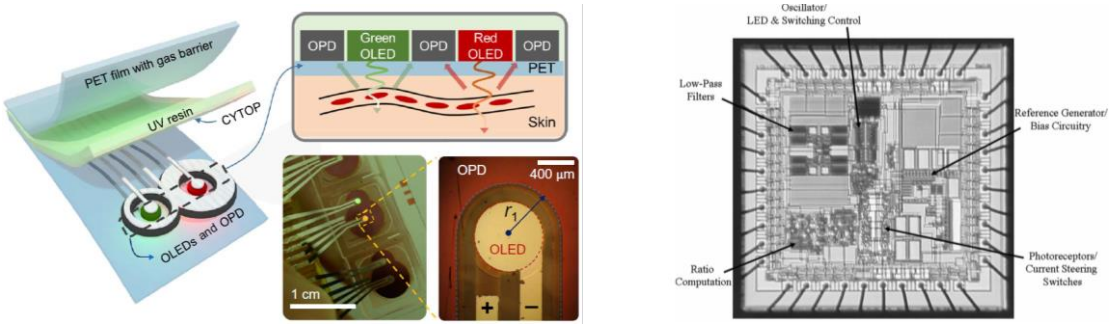

(a) (b)

Figure 3.6. Examples of pulse oximeter sensors: the reflective organic sensing patch developed by Lee et al. [108] (a), and the ultra-low-power device suggested by Tavakoli et al. [193] (b).

The authors attribute the reduction in power requirements to the use of a novel logarithmic transimpedance amplifier[2] with inherent contrast sensitivity, distributed amplification, unilateralization, and automatic loop gain control, which, when combined with a photodiode, results in a high-performance photodetector, allowing the reduction of power required for the light-emitting diodes (LEDs). The sensor operates at 5 V and requires 5.8 mW of power [193]. A commercially available IC component, previously described as a heart rate monitor, i.e., the MAX30102 HR device using the PPG principle, can also be employed as a low power pulse oximeter wearable component, operating within a 1.8 – 3.3V voltage range and consuming less than 1 mW of power [126], representing a viable option for a wearable medical device.

3.2. Data acquisition, processing and communication components

To enable sensor data acquisition and processing, a number of additional hardware blocks are required. Typically, an ADC will be placed between the sensor and a signal processor,

[2] A logarithmic transimpedance amplifier computes the logarithm or log-ratio of an input current or voltage relative to a reference current or voltage [195].

sometimes in combination with additional signal conditioning components, e.g. an electronic filter [175]. The acquired and processed data is then transmitted via a wireless communication module to a detached receiving device, e.g. a smartphone, for further analysis. The specific components selected in this frame significantly depend on the type, application and overall design requirements of the designed system, as well as the physical or physiological phenomena being measured.

3.2.1.Analogue-to-digital converters

Generally, the continuous signals representing attributes measured by the respective sensors, are analogue in nature, while the most commonly used components processing these signals require a digital input, thus creating the need for an ADC. ADCs allow the analogue signals to be sampled at discrete points in time, and the sample values to be represented in digital form, i.e., converted according to an appropriate code, making them readable by digital processors, e.g. computers or microcontrollers [128, 134]. Numerous different ADCs are available commercially, possessing different technical characteristics, i.e., noise, sensitivity, resolution or power requirements, which have to be carefully considered when designing a system. Some examples of commercially available ADCs are presented here, showing their basic properties along with the operating voltage ranges and power requirements. While all of the herein considered components operate within a comparable voltage range, i.e., 2 – 5.5 V, the two 16-bit ADCs, AD7684 and ADS1114, both show a sub-mW power consumption, 15 μW and 369 μW, respectively [147]. On the other hand, the 24-bit DS1251 requires up to ~ 2 mW of power [126].

3.2.2.Signal processors

One of the fundamental components of a wearable system is a signal processing module. This is, typically, a microprocessor or microcontroller, integrated on a single chip or as a separate independent component, providing the computational capability required for controlling the sensors and the communication modules, as well as the overall system operation [175]. Commonly, signal processors represent a major load for the power supply system, comparable to the wireless communication module, necessitating a thorough duty cycle optimization [175]. A few examples of commercially available signal processors suitable for wearable applications are considered here, and their operating voltage ranges and power requirements are given. In all three cases, the operating voltage ranges from ~ 1.7 to 3.6 V; however, in terms of power consumption, the 16-bit MC56F8006 requires ~ 140 mW at 32 MHz, while significantly lower

power levels are necessary for operation of the 16-bit STM32L151C8 and the 32-bit nRF52832 devices, i.e. 17.3 mW while operating at 32 MHz and 6.4 mW at 64 MHz, respectively [147].

3.2.3.Wireless communication components

The data acquired via the sensors and processed by a wearable medical device can either be stored using an on-board data storage module, ready to be accessed later, or it can be transmitted to an external device, e.g. a RFID scanner, a smartphone or, via two-stage communication, to a remote healthcare server. The on-board storage approach can be advantageous in terms of privacy and security, allowing data access to authorized individuals only, while the wireless transmission offers a more user friendly approach and allows real-time data access, e.g. by a physician or caretaker [116, 175]. The two-stage communication approach comprises a short range transmission of the acquired data between the wearable device and a nearby external gateway node, e.g. a smartphone, a computer or a microcontroller processing board, and a second, long-range transmission of the data to a distant server, located e.g. at a healthcare facility, via the internet or a cellular network. The short range transmission can function as a continuous data transfer or via periodical batch data transmissions occurring during the pairing of the wearable device with the external node. The gateway node receiving the short range data can also provide advanced data processing, analysis and visualization [116]. Wireless communication between the on-body sensors and the gateway node represents the preferred option over a wired connection, due to the cumbersome wires hindering the mobility of the user [116]. Various wireless protocols are currently being used, including RFID, Bluetooth, Wi-Fi, medical implant communication service (MICS) and ZigBee. The RFID protocol is limited to very short transmission ranges, i.e., to 0 – 3 m, and a low data transfer rate of ~ 640 kbps [116]. The power requirements of such a system are in the range of 200 mW, although the power from the wireless transmitter can also be used for the wearable node [91, 128]. Miniaturized RFID-based devices can also be designed as tattoo-like wearables applied directly on the skin [99]. Bluetooth represents a low power alternative able to transfer data up to 100 m at a rate of 1 – 3 Mbps [116], and it is widely available in most personal electronic devices. Furthermore, numerous commercially available IC components, e.g. the Laird® BL5340 series Bluetooth modules, offer a suitable solution for wearable applications [106]. The power requirements of a Bluetooth-based data transfer system typically range from 2.5 – 100 mW [116]. Wi-Fi is characterized by extremely high power requirements of up to 1 W, and complex configurations, as well as a considerable range of around 100 m and a high data transfer rate of ~ 54 Mbps [116]. It is, however, considered inefficient for long-term monitoring applications, due to the excessive battery drain,

and thus unsuitable for autonomous wearable devices [116]. MICS is an ultra-low power wireless communication technology operating at a short range of ca. 2 m, designed to enable communication with medical implants, e.g. cardiac pacemakers and neuro-stimulators, at a transfer rate of 200 – 800 kbps. It typically requires a very low amount of power in the range of 25 μW [116]. The ZigBee protocol represents, finally, a low power (35 – 100 mW) and low data transfer rate (250 kbps) technology, typically not available in consumer electronics, and it's able to transfer data within a 10 – 100 m range [91, 128].

3.3. Energy storage components

Wearables, same as all electronic devices, require power in order to function. A stable and reliable power source is therefore essential if the wearable device is expected to perform the tasks it is designed for, i.e., signal acquisition, processing and transmission [30, 52, 128]. It is suggested in recent literature that the maintenance needs of such devices should, ideally, be kept to a minimum, as well as that a continuous operation of a wearable device throughout its lifetime should be assured [30, 128, 139], which can be particularly important when implantable devices are considered, so as to limit the number of required surgical procedures due to battery replacements or device maintenance [175].

There are numerous methods of energy storage applicable to wearables, ranging from conventional and rechargeable batteries [175], up to various types of supercapacitors [52, 128] and biofuel cells [80]. Even though the current and ever improving rechargeable battery technologies (Li-ion and Li-Po), with high energy densities (20 – 150 Wh/kg), have mostly taken the place of the conventional non-rechargeable ones, they do exhibit a limited lifetime, e.g. 8 years for implantable pacemakers [37]. Supercapacitors (SCs) are devices with elevated capacitance values that can be utilized for energy storage, allowing rapid cycles of charge and discharge. Compared to batteries, they typically possess lower energy densities (4 – 5 Wh/kg), but exhibit a significantly longer lifetime (10 – 20 years) in a much wider temperature range [175]. Both rechargeable batteries and SCs are suitable to be used in combination with an energy harvesting system to accumulate the electricity intermittently generated by the EH system, thus ensuring a steady supply of power for the device to operate [52, 139, 164]. A suitable power management system, specifically designed for wearable EH systems is, therefore, required in this frame to balance the charge rate and power needs of the various components of the device, i.e. the sensors, the processors and the transmitters, as well as one or multiple EH generators [52, 139, 164].

An overview of energy storage devices, commonly utilized in wearable applications, is given in Table 4.1., where the voltages, energy capacities and energy densities of the various rechargeable and non-rechargeable devices are listed. Generally, the voltage range of these devices seems to be between 3 and 3.7 V, with batteries leaning towards the higher end of the range, and the SCs towards the lower. In terms of energy capacity, the highest values are found in conventional non-rechargeable batteries, followed by the rechargeable Li-ion and Li-Po ones, with the lowest values being exhibited by SCs, with a similar trend noticeable when energy density is considered [175]. The volume of the devices reported in Table 3.1. ranges from 1.1 cm^3 for SCs, up to 2.5 – 4.2 cm^3 for batteries, with rechargeable ones leaning towards the lower end of this range [175]. With this in mind, and considering the intermittent power generation of a typical kinetic EH system, characterized by periodical peaks in generated power, the use of SCs seems like a viable energy storage option for an autonomous wearable device [52, 139].

Table 3.1. Commonly used energy storage devices – technical data [175].

Device type	**Chargeability**	**Voltage, V**	**Capacity, mAh**	**Energy density, mAh/mm^3**	**Ref.**
1/2 AA battery	non-rechargeable	3.6	1200	0.29	[52]
CR2032 coin		3	240	0.23	[125]
300 mAh LiPo	rechargeable	3.7	300	0.08	[18]
120 mAh Li-ion		3.7	120	0.05	[139]
5 F supercap.		3	1.3	0.0008	[204]
1 F supercap.		3.2	0.3	0.0003	[149]

3.4. Power management

Energy harvesting devices typically generate voltage outputs that are highly dependent on the utilized EH principle. The direct current (DC) voltage generated by using a DC generator serving as an EH transducer exhibits a variation in amplitude dependent on the rotor velocity [94], while, on the other hand, a kinetic energy harvester based on a segmented piezoelectric cantilever generates a number of alternating current (AC) outputs at different frequencies, innate to each of the excited segments. The electrical output generated by an energy harvester also depends on the other components present within the circuit and their resistance values, i.e. the sensors, the processors and the transmitters, which not only affect the voltage amplitudes, but also the frequencies of the respective outputs. According to the overview given in the previous subsections, the electronic components typically employed in wearables require a stabilised DC voltage generally falling within the 2 – 5 V range for proper operation [10, 47, 55, 60,

83, 108, 127, 140, 146, 153, 179-181]. To obtain a smooth and stabilized voltage supply, according to the specified needs of individual wearable medical device components (sensors, processors and communication modules), a suitable management of the collected ambient energy is required, utilizing purposely designed power management circuitry. In cases when the sensing, processing and transmission electronic components are in a dormant state, an energy surplus may in turn be produced by the EH system. This surplus needs to be properly managed by the aforementioned circuitry, i.e. it needs to be stored on an energy storage component, e.g. a rechargeable battery or an SC [52, 128, 139], to be efficiently utilized by the respective load when required. Another benefit of using a storage element is the possibility to achieve short power bursts. These high amounts of energy can be delivered to the respective component in short time periods, typically required by data transmission components during the periodical transfers of the acquired data.

The central component of a typical set of generalized power management electronics, schematically displayed in Figure 3.7., is a DC-to-DC buck converter, which collects low level energy on a low capacity storage component, i.e., a capacitor on the primary side and transfers this energy to the secondary side, once the energy levels are high enough to charge the main storage component or to power a predefined load. Some of the commercially available ICs suitable for EH power management in autonomous wearable medical devices are shown in Table 3.2., listing some of their basic technical characteristics, where the majority of the ICs possess multiple inputs for different EH sources, and are able to support output currents up to 100 mA, i.e., up to 500 mW at 5 V [24, 52, 72, 179, 196].

Table 3.2. Typical off-the-shelf power management ICs suitable for wearable EH.

Device type	Input voltage	Output voltages	Ref.
Solar/piezoelectric kinetic/electro-magnetic EH devices			
MB39C811	2.6 – 23 V DC/AC	1.5, 1.8, 2.5, 3.3, 3.6, 4.1, 4.5, 5 V DC	[94]
Solar/piezoelectric kinetic/electro-magnetic EH devices			
LTC3588-1	2.7 – 20 V DC/AC	1.8, 2.5, 3.3, 3.6 V DC	[26]
LTC3588-2	14 – 20 V DC/AC	3.45, 4.1, 4.5, 5 V DC	[133]
Solar/thermo-electric/radio-frequency/piezoelectric kinetic EH devices			
MAX17710	0.75 – 5.3 V DC	1.8, 2.3, 3.3 V DC	[126]

The input voltage threshold needed to “wake up” the power management electronics varies from mV up to several tens of V, depending on the IC component. To protect the device, the maximum voltage is typically limited (clipped by a protective shunt) to ~ 20 V. Furthermore, a

full-wave bridge rectifier is embedded in some of the commercial ICs allowing the direct connection of low-power AC generators, i.e., PEHs [24, 72, 179, 196].

If the energy harvested from the ambient is to be efficiently utilized, and the normal function of all the components ensured, the operating principle of the EH system, as well as the technical characteristics of the connected load components need to be carefully considered, and appropriate passive elements, e.g. resistors, inductors and capacitors, need to be included within the circuitry and optimized, as it can be seen in the schematics depicted in Figure 3.7. Such an approach to EH power management has been successfully used in previous research aimed at energy harvesting solutions dealing with autonomous tire pressure monitoring systems [26], as well as an autonomous remote wireless sensor network utilizing energy from river flow [94].

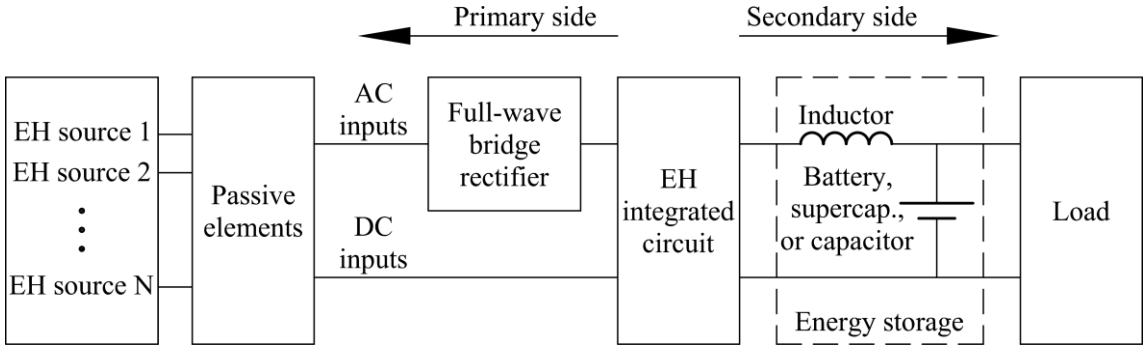

Figure 3.7. Generalized schematic representation of EH power management electronics.

3.5. Example of a wearable device

Based on the above listed and described electronic components, displayed in Table 3.3., ensuring a better overview, it is possible to assemble a theoretical wearable medical device, to estimate its overall power requirements. This information will, in turn, be of vital importance in the design of EH solutions aimed at powering the herein studied class of devices. Such an integrated device could, for example, comprise a number of sensors, a signal processor, a communication module as well as an analogue-to-digital converter as well as the power management circuitry. As a medical device, its components that measure body temperature, e.g. the MCP9700 sensor, a pulse oximeter monitoring heart rate, e.g. the MAX30102 sensor, as well as an accelerometer aimed at fall detection, e.g. the analogue ADXL337, could form its basic array of sensors, each paired with an ADC DS1251 analogue-to-digital converter. The acquired data could be processed using an nRF52832, 32-bit ARM Cortex-M4, operating at 64 MHz, and then transmitted via a 2.4–2.5 GHz Bluetooth communication module over a distance up to 100 m, easily covering, for example, the surface area of a house or an apartment, i.e., ensuring

the first (short-range) part of the aforementioned two-stage communication approach. The power required by such a device, amounting to ~ 115 mW without considering duty cycles, could be generated via a kinetic EH system, managed using the MB39C811 module (supporting multiple inputs as well as a wide array of output voltages) and stored on an appropriate SC component. A simplified schematic of this device is shown in Figure 3.8. As the power management circuitry typically allows multiple inputs, different EH power sources can be combined, creating a hybrid EH system [16, 139], utilizing a wider range of available energy sources, e.g. waste heat via thermoelectric generators [16, 72], in addition to the kinetic energy generated from human motion. Such an approach could significantly increase the amount of available power, thus improving the autonomy of the wearable device. It should be noted here that the list of components provided above could be optimized according to their respective power or voltage needs as well as according to their load resistance values, which should, ideally, be paired with the internal resistance of the EH system, ensuring, thus, the maximum conversion efficiency and, therefore, the maximum power output. Since a sizable portion of the power required by such a device is used by the communication components, the overall power consumption could potentially be significantly reduced by implementing the periodical approach to data acquisition and transfer, i.e., duly considering the respective duty cycles [98]. Several parameters, commonly measured by wearable devices, do not require continuous monitoring, according to medical guidelines, e.g. the body temperature in patients is taken in the morning and in the evening, blood pressure is most commonly monitored a couple of times per day to correct the prescribed therapy, while a fall detector data is relevant only when the acceleration suddenly exceeds a certain threshold [9, 72]. These guidelines could help in creating a data transmission schedule, eliminating, thus, the need for a constant data transfer, i.e., requiring high power bursts only a couple of times a day for a very short period of time [9, 72]. Some health parameters, e.g. the blood glucose levels, the heartrate and blood oxygenation, on the other hand, require continuous monitoring [10]. However, by setting appropriate threshold levels for the monitored parameters, the wearable device could be set to send an alarm signal only in cases when values larger (or smaller) than a predefined threshold, are detected, eliminating the need for constant communication, thus significantly reducing the power consumption again. The duty cycles of electronic components commonly used in wearable medical devices, reported in available literature, typically range from 0.001% for a Bluetooth system, over ~ 10% for displays and 8-50% in the case of pulse oximeters, depending on the operating mode, 20-80% for signal processors and up to 100% for temperature sensors [98, 147, 186].

Table 3.3. Sensors, processors and communication components applicable to wearables

Device type	Voltage	Power	Ref.
MEMS accelerometer			
Analogue, 300 mV/g, ADXL337	3.0 V	900 μW	[147]
Digital, 3.9 mg/LSB, ADXL345	2.5 V	350 μW	[147]
KX022 tri-axis (* - low power mode)	1.8 – 3.6 V	522 (36*) μW	[167]
Temperature sensor			
BD1020HFV -30°C to +100°C	2.4 – 5.5 V	38.5 μW	[167]
MAX30208 0°C to +70°C	1.7 – 3.6 V	241 μW	[126]
MCP9700 -40°C to +150°C	2.3 – 5.5 V	82 μW	[131]
Heart rate monitor			
Samsung Galaxy Gear Neo 2® component	-	~ 50 mW	[11]
MAX30102 pulse oximetry / heart-rate monitor	1.8 – 3.3 V	< 1 mW	[126]
BH1790GLC optical heart rate sensor	1.7 – 3.6 V	720 μW	[167]
Blood pressure monitoring approaches			
Conformal ultrasonic device	-	~ 24 mW	[207]
Wearable sensor with Au nanowires	1.5 V	< 30 mW	[74]
CMOS Tactile Sensor	5 V	11.5 mW	[174]
Blood glucose monitoring system			
IoT-based CGM system sensor node	2 V	1 mW	[66]
Continuous glucose monitoring contact lens	~ 100 mV	< 1 μW	[80]
Implantable RFID CGM sensor tag	1 – 1.2 V	50 μW	[214]
Pulse oximeter sensor			
Reflective organic pulse oximetry sensing patch	3.3 – 5 V	68 – 125 μW	[108]
Ultra-low-power pulse oximeter with amplifier	5 V	4.8 mW	[193]
MAX30102 pulse oximetry / heart-rate monitor	1.8 – 3.3 V	< 1 mW	[126]
Analogue-to-digital converter			
AD7684 16-bit SAR 100 kS/s	2.7 – 5 V	15 μW	[147]
ADS1114 16-bit sigma-delta 0.860 kS/s	2 – 5.5 V	368 μW	[147]
DS1251 24-bit sigma-delta 20 kS/s	3.3 – 5 V	1.95 mW	[126]
Signal processor			
MC56F8006 Audio DSP, 16-bit 56800E	1.8 – 3.6 V	137 mW	[147]
STM32L151C8, 32-bit ARM Cortex-M3	1.7 – 3.6 V	17.28 mW	[147]
nRF52832, 32-bit ARM Cortex-M4 64	1.7 – 3.6 V	6.4 mW	[147]
Communication protocol			
RFID 13.56 MHz 860–960 MHz (0 – 3 m)	-	200 mW	[116]
Bluetooth 2.4–2.5 GHz (1 – 100 m)	-	2.5 – 100 mW	[116]
Wi-Fi 2.4–5GHz (100 m)	-	~ 1 W	[116]
MICS 402–405 MHz (2 m)	-	25 μW	[116]
ZigBee 900 MHz–2,4GHz (10 – 100 m)	-	35 – 100 mW	[175]

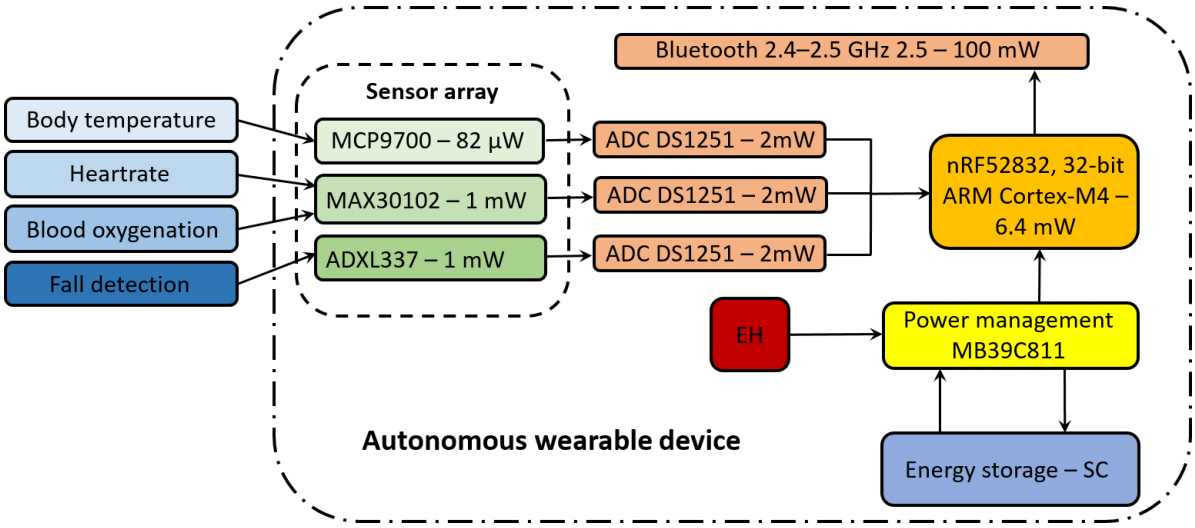

Figure 3.8. Schematic depiction of an autonomous EH-powered wearable medical device.

When the respective duty cycles are taken into consideration, the overall power required by the above described miniaturized wearable medical device amounts to ~ 5 mW.

A comprehensive overview of mostly commercially available electronic components, namely sensors, ADCs, signal processing, as well as energy storage and communication modules, commonly utilized in wearable applications, was given in this section. The basics of EH power management, with particular attention to wearable medical applications, was presented and an example of an autonomous wearable device was suggested, necessitating ~ 5 mW of power for optimal operation.

The experimental and numerical methods used for the development of optimized piezoelectric EH devices will hence be described in the following section. It will provide a detailed description of two experimental setups utilized in this work, covering the essential characteristics of their main components. The chronological development of the most prominent mathematical models will also be outlined, and the complex numerical modelling approach will be thoroughly presented. What is more, a short outline of the issues occurring in the clamping area of the PEH will also be given.

4. EXPERIMENTAL AND NUMERICAL METHODS

In order to enable the development of novel PEH geometries, a suitable modelling approach is needed. Furthermore, appropriate experimental setups are required to validate the results obtained via numerical simulations. This section will cover in detail the methods and models used in this thesis, along with a comprehensive overview of the herein developed experimental setups[3].

4.1. Experimental setups

The extensive stress, modal, harmonic, and transient numerical FE analyses, conducted in this work, require to be validated by suitable experimental measurements, in order to ensure the accuracy of the obtained results and the viability of the models in the development of optimized PEHs. Two separate experimental setups are thus developed at the Precision Engineering Laboratory [200], emulating both the harmonic as well as the plucking (FUC) PEH excitation. The experimental measurements carried out by using these setups will enable the validation of the numerical models, comprising the results of the modal, the harmonic and the transient analyses, but also provide means for a comprehensive characterization of the optimized devices, developed within this work.

4.1.1. Harmonic excitation setup

The harmonic excitation setup, schematically displayed in Figure 4.1a with the individual components shown in Figures 4.1b and 4.1c, is employed to induce a controlled harmonic (sinusoidal) excitation to the clamped PEH bimorph over a predefined frequency range using an electrodynamic permanent magnet shaker. The parameters of the sinusoidal signal are controlled with a NI LabVIEW® [141] virtual instrument operating on the NI MyRIO 1900 device [142], which is also used for data acquisition (DAQ). The excitation, provided by a Brüel&Kjær® LDS V201 electrodynamic permanent magnet shaker (1) [32] powered by a sinusoidal signal via an LDS LPA100 power amplifier [31], and thus of the PEH clamping fixture

[3] Part of the work described in this section was published by the author of the thesis and his collaborators in two peer-reviewed scientific papers (refs. [70] and [71]), which were produced and published as part of the obligations foreseen in the curriculum of the doctoral study of the Faculty of Engineering of the University of Rijeka, Croatia, and hence this section is based, partly directly derived and cited from this work. All the numerical and experimental data, relevant for this work, is available online at https://repository.riteh.uniri.hr/islandora/object/riteh:2274.

(5), is assessed using a Vernier® 3D-BTA accelerometer (3) [202], affixed to the PEH clamping base and connected to the Vernier® BT-MDAQ adapter (4) [203], linking it to the aforementioned NI MyRIO 1900 device (2). The studied PEH, subjected to harmonic excitation, is clamped to a 3D printed fixture attached to the shaker, and connected in parallel to the DAQ unit via a TE® 1051 resistance decade box (6) [196], allowing the variation of load resistance values from 10 mΩ up to ~ 1MΩ.

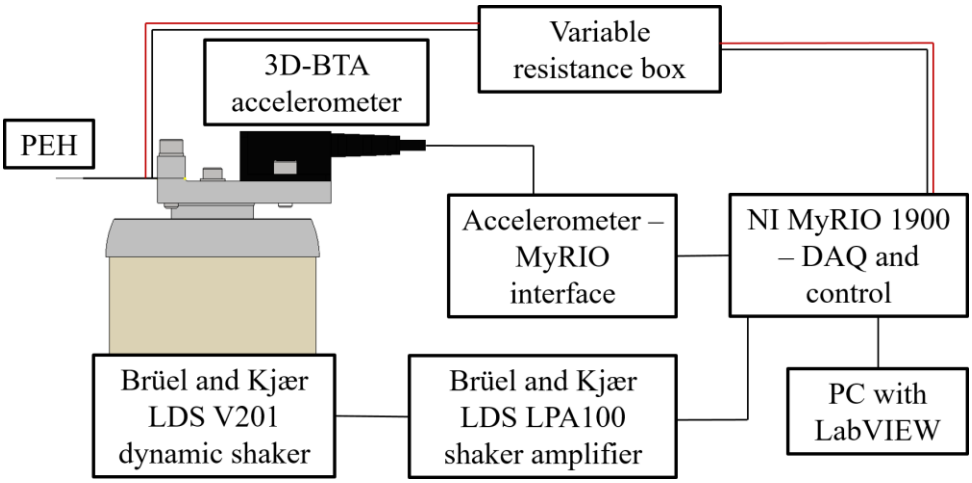

(a)

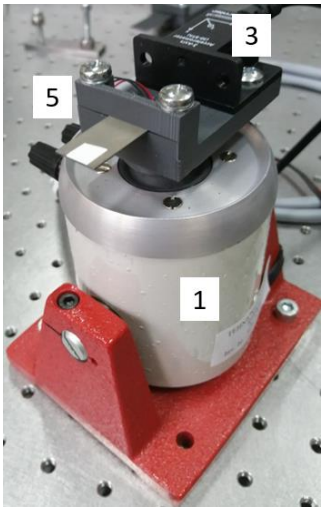

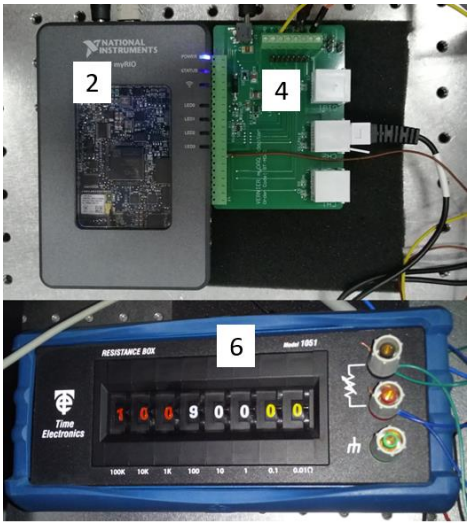

(b) (c)

Figure 4.1. Schematic representation of the harmonic experimental setup (a), shaker, accelerometer and PEH (b), DAQ and control components with the variable resistance box (c).

The boundary conditions at the clamped end, as well as the excitation characteristics, are set as close as possible to those used in the FE model, minimizing, thus, the possible mismatch of the results. The basic technical characteristics of the experimental equipment utilized in this work are provided in the Tables 4.1. and 4.2.

Table 4.1. B&K® LDS V201 shaker technical [32].

B&K® LDS V201 shaker	
Sine force peak, N	26.7
Max acceleration sine peak, g	91
Velocity sine peak, m/s	1.83
Displacement continuous p-p, mm	5
Moving element mass, kg	0.020
Usable frequency range, Hz	5 – 13 000

Table 4.2. B&K® LDS LPA100 power amplifier technical data [31].

B&K® LDS LPA100 power amplifier	
Rated power output	94 VA in 3.15 Ω
Maximum power output capacity	154 VA in 3.15 Ω
Gain	22 V/V ± 2 dB max.
Frequency range at maximum power	DC to 15 kHz for 30 min at max. VA
Total harmonic distortion at rated output	<0.1%, 15 Hz to 5 kHz <0.2%, 5 kHz to 15 kHz
Signal-to-noise ratio	> 95 dB

The basic information regarding the three axes accelerometer, i.e., its range and accuracy is given in Table 4.3., while the specifications of the resistance box, comprising the resistance range as well as the respective maximum current and accuracy, are listed in Table 4.4.

Table 4.3. Vernier® 3D-BTA accelerometer technical data [202].

Vernier® 3D-BTA accelerometer		
For each axis	Range:	± 49 m/s^2 (±5 g)
	Accuracy:	± 0.5 m/s^2 (±0.05 g)
	Typical Resolution:	0.037 m/s^2
Stored calibration information	Slope:	30.46 m/s^2/V
	Intercept:	–72.62 m/s

Table 4.4. TE® 1051 Resistance Decade Box Technical data [196].

Time Electronics® 1051 Resistance Decade Box								
Range	0 to 1 MΩ							
Resolution	0.01 Ω steps							
Residual resistance	Less than 90 mΩ							
Power rating	1 W per resistor							
Decade	0.01 Ω	0.1 Ω	1 Ω	10 Ω	100 Ω	1 kΩ	10 kΩ	100 kΩ
Accuracy	± 10%	± 5%	± 1%	± 0.5%	± 0.1%	± 0.1%	± 0.1%	± 0.1%
I_{max}	1 A	1 A	1 A	0.3 A	0.1 A	33 mA	10 mA	3 mA

4.1.2. Impact excitation setup

The impact excitation setup provides the means for a controlled process of plucking the PEH free end, thus emulating the FUC excitation method. The system consists of a rigid 3D printed PEH clamping base and a Faulhaber DC motor-gearhead assembly [59] equipped with a number of plectra radially arranged on a 3D printed rotor. The clamping structure allows the adjustment of the distance between the rotor axis of rotation and the tip of the free end of the PEH. A purely mechanical (i.e. not magnetic) plucking mechanism is used here to prevent the possible damping effects of magnets on the oscillating PEHs [54, 157]. The plucking frequency, i.e., the DC motor rotation speed, can be controlled by controlling the voltage supplied to the motor via a laboratory power supply [87], and can, thus, be calculated via the following expression [59]:

$$n_0 = \frac{U - (I_0 \cdot R)}{2\pi \cdot i \cdot k_M}, \tag{4.1}$$

where n_0, min^{-1}, is the DC motor output shaft speed, U, V, is the supply voltage, R, Ω, represents the terminal resistance of the DC motor, and I_0, A is the no-load current. The term i is the gear ratio of the gearhead and k_M, mNm/A, represents the torque constant for the selected DC motor [59]. For the herein utilized Faulhaber 2233.A0459 018S DC motor-gearhead assembly [59], the above listed values are: I_0 = 5 mA, R = 25 Ω, i = 28 and k_M = 18.8 mNm/A.

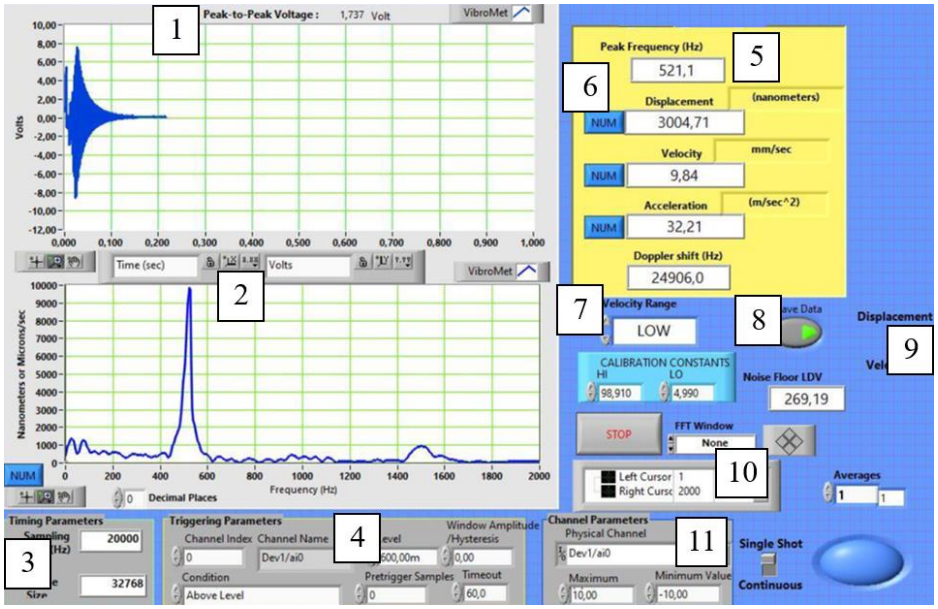

Figure 4.2. Laser vibrometer DAQ VI graphical interface: laser signal voltage output (1), FFT (2), sampling frequency settings (3), triggering signal settings (4), measured peak frequency (5), calculated acceleration, velocity and displacement amplitudes (6), velocity range and calibration constants settings (7), data saving (8), velocity vs. displacement switch (9), frequency axis settings (10) and signal input settings (11) [119].

The coupled electromechanical response, i.e., voltage output generated by plucking the PEH free end, is acquired by using an Agilent® DSO-X 2012A oscilloscope [3], connected in parallel to the PEH electrodes via a TE® 1051 resistance decade box [196], where the optimal load resistance for the respective PEH is set. A Metrolaser® Vibromet 500V laser Doppler vibrometer [130] is utilized, in this frame, to assess the initial displacement of the plucked PEH free end. The procedure consists of acquiring the voltage corresponding to the velocity of the tip, by using the aforementioned laser Doppler vibrometer combined with the respective NI LabVIEW® virtual instrument (VI) [141], whose graphical interface is shown in Figure 4.2. Due to accuracy issues inherent to the conversion method used by the DAQ VI, the laser signal voltage is converted to velocity via a set of calibration constants and, finally, into the value of the displacement by integration using the ENDAQ® VibrationData MATLAB® toolbox [51].

The schematic representation of the overall FUC setup is shown in Figure 4.3a, where all the essential components, as well as the position of the tested PEH are marked. Figures 4.3b and 4.3c display, on the other hand, the above described setup components denoted as: 3D printed PEH clamping base (1), rotor equipped with plectra (2), DAQ - oscilloscope (3), laser Doppler vibrometer (4), tested PEH (5), and resistance decade box (6). The basic technical data of the setup components are listed in the Tables 4.5., 4.6., and 4.7.

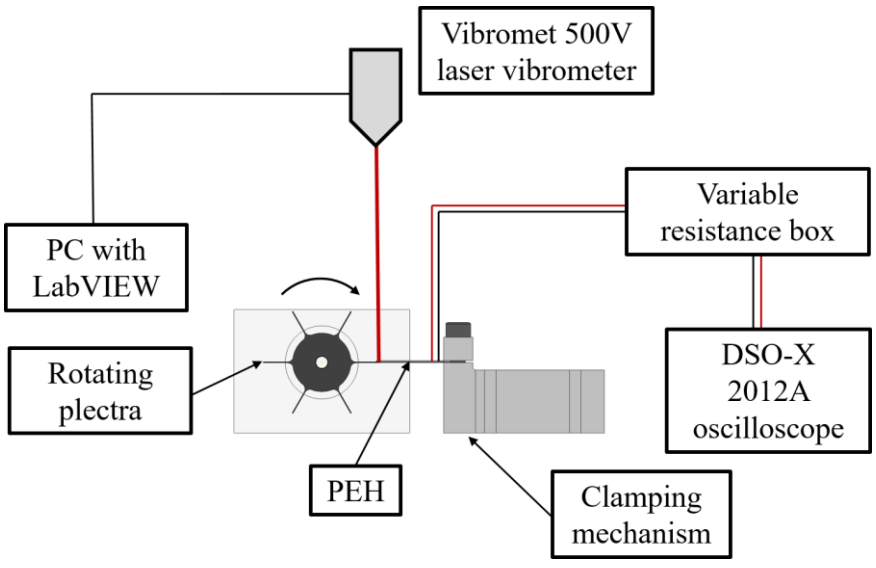

(a)

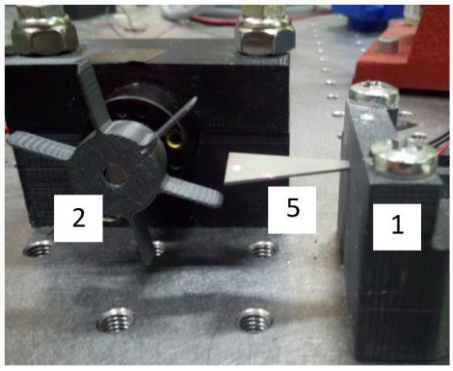

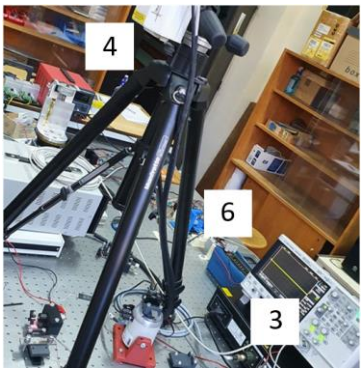

(b) (c)

Figure 4.3. Schematic representation of the FUC experimental setup (a), plucking excitation components (b), and data acquisition components (c).

Table 4.5. Faulhaber 2233.A0459 018S DC motor technical data [59].

Faulhaber 2233.A0459 018S	
Nominal voltage	4.5 ... 30 V
Torque up to (max.)	5.9 mNm
No-load speed	9,000 min^{-1}
Stall torque	20.2 mNm
Terminal resistance	25 Ω
Torque constant	18.8 mNm/A
No-load current	5 mA
Gearhead ratio	28

Table 4.6. Vibromet 500V Laser Doppler Vibrometer technical data [130].

Vibromet 500V Laser Doppler Vibrometer	
Velocity range	5 μm/s to 1000 mm/s
Vibration frequency range	DC to > 20 kHz
Working distance	1 cm to 5 m
Movement range	0.1 nm to 10 mm
Laser	780 nm, <15 mW, Class Illb 650 nm, <1 mW, Class II

Table 4.7. Agilent InfiniiVision DSO-X 2012A oscilloscope technical data [3].

Agilent InfiniiVision DSO-X 2012A oscilloscope	
Analogue Channels	2
Bandwidth (upgradable)	100 MHz
Waveform update rate	50,000 waveforms per second

4.2. Coupled model of electromechanical PEH behaviour – a short overview

Numerous analytical and numerical techniques aimed to model the coupled electromechanical behaviour of piezoelectric energy harvesters have been suggested and used in available literature [25], starting with the rather simplified one degree-of-freedom (1-DoF) lumped parameters method aimed at an initial understanding of the dynamically excited PEH system, which, due to the simplification to a single DoF, introduces significant errors and cannot be used to accurately predict the behaviour of a real physical system [169, 211]. The later developed discretized Rayleigh-Ritz energy approach with spatially distributed parameters, providing approximate results [49, 184], in addition to the Euler-Bernoulli method coupled with the fundamental piezoelectric equations [6], along with the 1-DoF lumped parameters method, also displays several shortcomings in terms of not considering the resonances, not including higher vibration modes, the incorrect interpretation of the excitation, the simplification of the electromechanical coupling and of the viscous damping effects, as well as of representing dynamical problems by using static terms [25, 56].

The comprehensive fully distributed parameters method based on the Euler-Bernoulli cantilever equation, i.e., the "coupled modal electromechanical distributed parameter model" (CMEDM), developed by Erturk and Inman in 2009, provides the most accurate predictions of PEH behaviour. This method also takes into account the material viscous damping as well as the effect of the fluid the PEH is oscillating in, the backward coupling effects, the influence of the tip mass and the system's electrical domain. The CMEDM model was thoroughly experimentally validated and overcomes most of the issues found in previous methods [25, 55-56]. The resulting output voltage amplitude α_s of the piezoelectric energy harvester can hence be described as [55]:

$$\alpha_s(\omega) = \frac{\sum_{r=1}^{\infty} \frac{j\omega\kappa_r\sigma_r}{\omega_r^2 - \omega^2 + j2\zeta_r\omega_r\omega}}{\frac{1}{R_L} + j\omega\frac{C_{\tilde{p}}}{2} + \sum_{r=1}^{\infty} \frac{j\omega\kappa_r\chi_r^s}{\omega_r^2 - \omega^2 + j2\zeta_r\omega_r\omega}} e^{j\omega t}, \tag{4.2}$$

where j represents the imaginary unit, ω (s^{-1}) is the excitation frequency near the eigenfrequency of the PEH, i.e., ω_r (s^{-1}), κ_r is the forward coupling term, σ_r the translational excitation component, ζ_r is the mechanical damping, R_L (Ω) represents the external electrical load connected to the system, $C_{\tilde{p}}$ (F) is the capacitance of the piezoelectric material and χ_r^s represents the modal coupling term [55].

Despite the CMEDM currently being the most accurate analytical method to predict the behaviour of PEHs, certain disadvantages innate to the model need to be considered. The most

significant constraint of the model is that it is limited to a constant rectangular cantilever cross-section, which makes it unsuitable for the development of new and improved PEH shapes [55, 71]. With that in mind, a 3D numerical modelling approach needs to be employed to study the effects of different geometries on the PEH response. The basic numerical model and the subsequently employed analyses will thus be thoroughly described in the following subsections [103, 210, 220].

4.3. Numerical model and finite element types

For the purpose of studying the effects of different geometries on the response of bimorph PEH devices clamped at one end, a numerical 3D model is developed in ANSYS® - a numerical analysis software package widely accepted in available literature as a viable tool for modelling piezoelectric phenomena [103, 210, 220]. The APDL (ANSYS® parametric design language), in combination with the graphical interface, is used in this frame. The 3D geometry model is generated by using a conventional 3D CAD software in the manner that every individual layer, i.e., the substrate and the piezoelectric, is represented as a separate body. Such a geometry is then imported into ANSYS® in the form of volumes, and the respective material and piezoelectric properties are assigned to the respective layers. The dimensions of the 3D model correspond to the commercially available conventional rectangular PEH, manufactured by Piezo.com® [153], and are listed in Table 4.8. The material properties of the stainless steel substrate and the PZT-5A (lead zirconate titanate) piezoelectric material, selected for its high conversion efficiency, compared to other available materials, as well as for its temperature stability [135, 173] are also provided in Table 4.8., along with the thicknesses of their respective layers. The imported volumes, i.e., PEH layers, can be connected at this point by utilizing the “glue volumes” tool, although the connection of the layers can also be achieved after meshing by using the “merge nodes” tool. The effects of each of the chosen approaches on the PEH modal response will be studied below. Meshing is the process of discretization applied to the studied body, i.e., the body is modelled as a mesh of finite elements (FE) that are connected at their nodes [143]. Interpolation models are introduced within the finite elements to specify the approximate expressions for the unknowns. This is generally done in terms of the nodal values. The global equilibrium equations are obtained by assembling the equilibrium equations of the finite elements [143]. The respective physical conditions, i.e., the loads and constraints, are then applied as the boundary conditions of the global set of equilibrium equations [143].

Table 4.8. Piezo.com® rectangular PEH - dimensions and material properties [153].

Dimensions			
Length – overall / free end	l_0 / l	30 / 23	mm
Width	w	15	mm
Piezoelectric layer - PZT-5A (3195HD)			
Elastic modulus	E_{PZT}	52	GPa
Poisson ratio	ν_{PZT}	0.31	-
Density	ρ_{PZT}	7800	kg/m^3
Piezoelectric strain coefficients	d_{31}	390	pC/N
	d_{33}	-190	pC/N
Polling / connection	33 mode / parallel		
Piezoelectric layer thickness	t_p	0.254	mm
Substrate layer - stainless steel			
Elastic modulus	E_s	193	GPa
Poisson ratio	ν_s	0.29	-
Density	ρ_s	7800	kg/m^3
Substrate layer thickness	t_s	0.15	mm

A careful consideration and selection of the finite elements' type according to their properties is essential if the behaviour of the considered physical system is to be realistically represented [187]. The piezoelectric layers of the studied PEH are thus modelled using the standard three dimensional coupled-field solid prismatic finite element SOLID226, available in the ANSYS® FE database (Figure 4.4a). In fact, the SOLID226 element, possessing 20 nodes with up to 6 DoFs per node, allows the interpretation of several material properties including the piezoelectric, piezoresistive and thermoelectric properties [5]. On the other hand, the substrate layer is modelled by using the standard three-dimensional structural solid prismatic finite element SOLID186. The latter exhibits a quadratic displacement behaviour and supports several material models, and it possesses 20 nodes and 3 DoFs for each node. The elements of the FE model can also be formed as tetrahedral-shaped elements (Figure 4.4b) [5].

In order to model the electromechanical coupling, another finite element type, the CIRCU94 one (in Figure 4.4c), is introduced and connected to the piezoelectric layers (SOLID226 element nodes) by using the respective VOLT degrees of freedom (Figure 4.5a), thus simulating the electrodes and electrical connections. CIRCU94, a circuit finite element, used to simulate the basic linear electric circuit components, e.g. a resistor, an inductor or a capacitor, which can be directly connected to the piezoelectric FE domain [5], possesses two or three nodes used to define the circuit component along with one or two DoFs, for modelling the response of the

circuit [5].

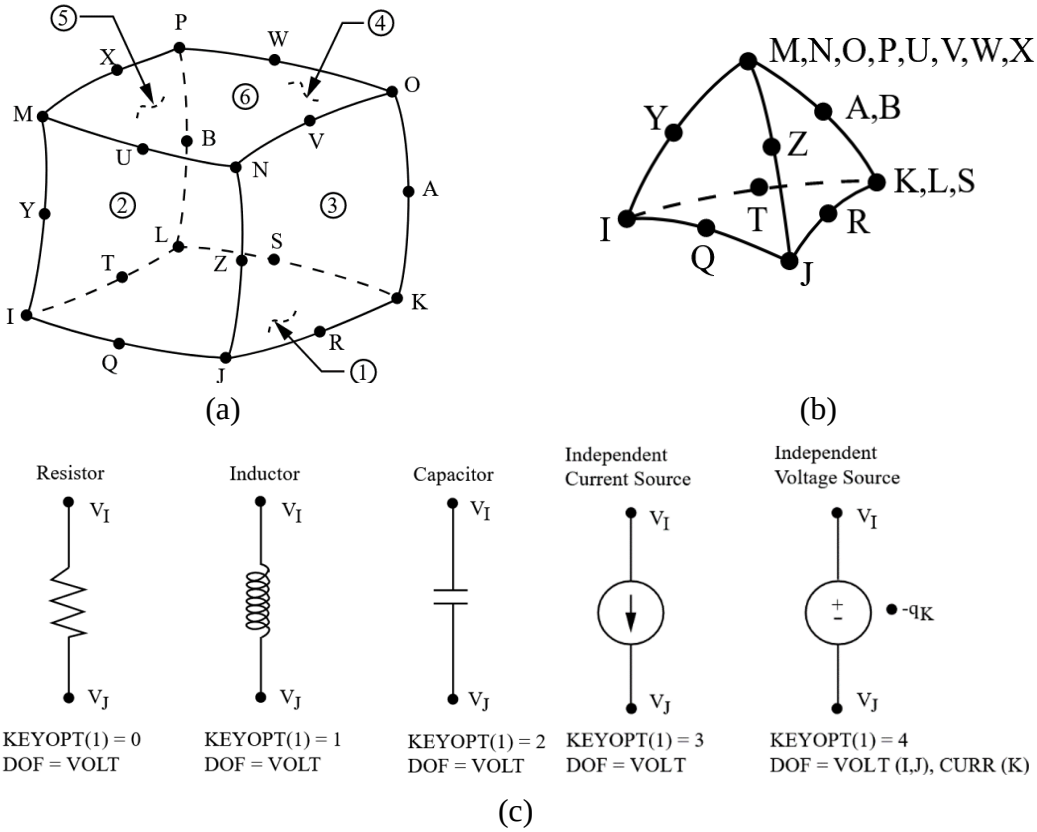

Figure 4.4. 3D representation of the SOLID186 and SOLID226 finite elements in the prismatic form (a) and in the tetrahedral form (b), and the symbolic representation of the CIRCU94 finite elements (c) [5].

The boundary conditions present at the clamped end are introduced as movement constraints, i.e., zero-value displacements, in all three planes, applied to all the nodes belonging to the areas that correspond to the surfaces on which the physical PEH is clamped (Figure 4.5b), a well-known method, commonly employed in available literature [64, 135].

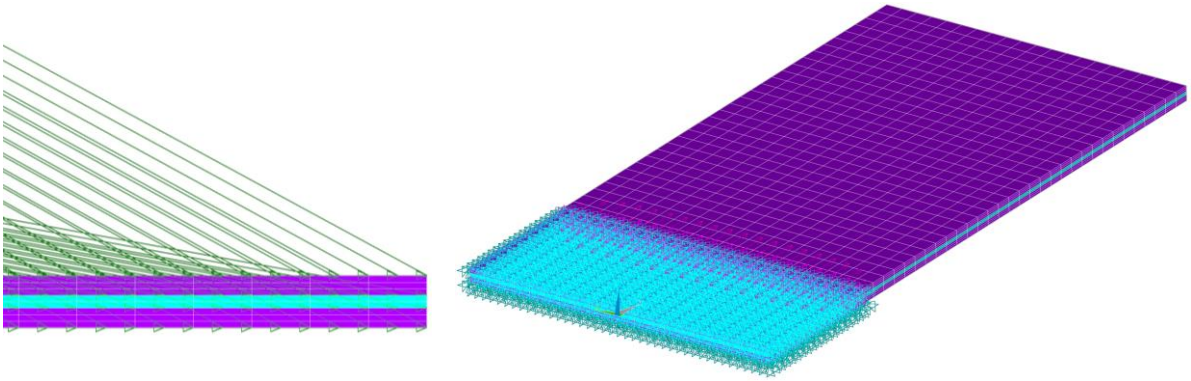

(a) (b)

Figure 4.5. Boundary conditions applied to the FE model: connection of the piezoelectric layers using VOLT DoFs (a) and constraints at the clamped end (b).

Before introducing the numerical analyses types used within this work, it should be pointed out that finite element modelling represents an approximate method of analysis, and the thus attained results need to be considered with due discretion [187]. In general, two main classes of errors occur within FE analyses, i.e., modelling and numerical errors can be obtained. Modelling errors are typically the result of inaccurate data input, e.g. material properties or boundary conditions, although they can also originate from compromises in the meshing process, e.g. the rounding of sharp edges. On the other hand, numerical errors mainly occur due to round-offs and truncations [143]. In both cases, a practical approach to assessing FE errors is the comparison of two different meshes, the second being a refinement of the former [143].

4.4. Finite element analysis

The study of the different aspects of PEH behaviour requires different approaches. A stress analysis needs to be carried out in order to limit the stress levels within the piezoelectric layers. Modal analyses are, in turn, used to assess some of the boundary conditions needed for the subsequent harmonic analyses. The latter generate voltage responses for the studied PEHs. Transient analyses are utilized in this work for simulating the process of plucking the PEH free end, and thus providing the respective voltage responses. In this manner, the behaviour of a PEH subjected to both harmonic and FUC excitation can be studied. In order to minimize the errors, as well as to optimize the computational times, a comprehensive mesh sensitivity analysis is conducted. In the following subsections, the aforementioned methods will be described in the case of a conventional rectangular PEH.

4.4.1. Mesh sensitivity analysis

It is well known that the finite element model (FEM) accuracy is significantly influenced both by the selected element type as well as by the size of the elements themselves, i.e., the density of the mesh [143]. By reducing the size of the elements, the density of the mesh increases, and the accuracy of the results, generally, increases as well. However, the increased number of elements results also in a larger number of equations, and thus a longer computation time [143, 187]. An analysis of the mesh sensitivity is, therefore, needed in order to balance these effects. In this frame, the mesh sensitivity analysis is carried out for two separate types of finite elements, i.e., the above hexahedral – brick or cube, and the tetrahedral elements. A gradual variation of mesh density is, in turn, achieved by varying the length of the element edge between 0.25 and 2 mm with 0.25 mm increments, as it can be seen in Figure 4.6. Additionally,

two different methods of volume bonding available in ANSYS® are utilized to join the hexahedral elements within the piezoelectric layers with those in the substrate, i.e., the "glue volumes" function and the merging of neighbouring nodes, and their effect on the accuracy of the results is analysed as well.

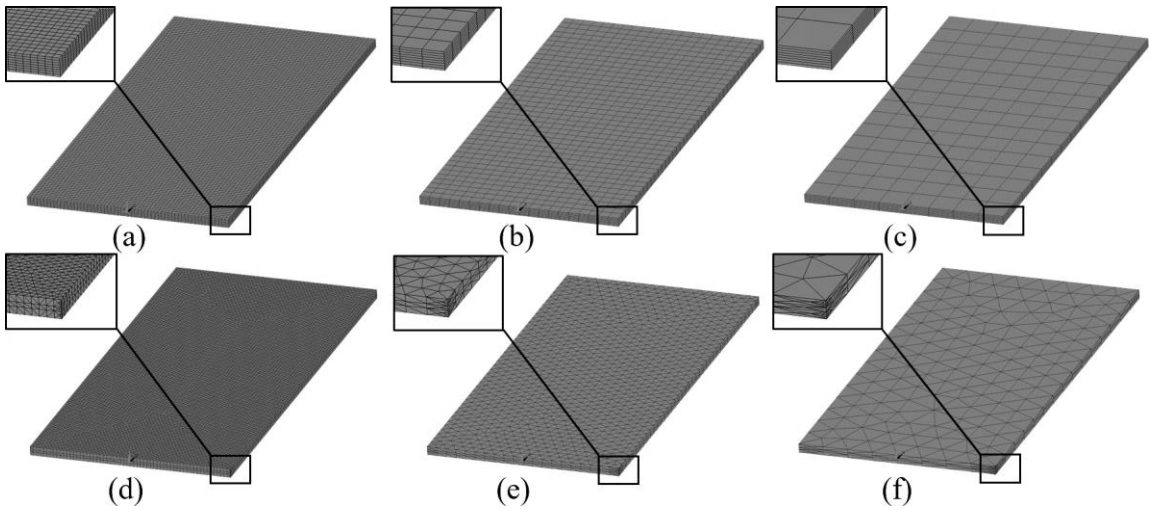

Figure 4.6. Meshes using hexahedral elements with different edge lengths: 0.25 mm (a), 0.75 mm (b) and 2 mm (c) as well as tetrahedral elements with different edge lengths: 0.25 mm (d), 0.75 mm (e) and 2 mm (f).

The modal analysis, described in more detail in the following subsections, is used here to generate a modal response, i.e., to assess the first vibration mode, as well as the first eigenfrequency f_1 of the studied structure for different element types, mesh densities and volume bonding methods. The thus obtained solutions are, in turn, compared to the values determined via experimental measurements, both by the free end ($f_{1\text{base}}$ = 539.38 Hz, σ_{sd} = ± 1.47 Hz) as well as via the base excitation ($f_{1\text{FreeEnd}}$ = 535.15 Hz, σ_{sd} = ± 1.04 Hz), and the respective relative errors e_{r} are calculated. The minor difference in the first eigenfrequency values attained experimentally via the two excitation methods, i.e. 0.79%, can be attributed herein to errors in the PEH clamping implementation, which can significantly affect the response. The comparison of the results for hexahedral elements with merged nodes, along with the relative errors for both excitation methods, $e_{\text{r\_Base}}$ and $e_{\text{r\_FreeEnd}}$, are displayed in Table 4.9., while those obtained by using hexahedral nodes with glued volumes can be seen in Table 4.10. The mesh sensitivity analysis data for the tetrahedral elements with glued volumes is, finally, shown in Table 4.11. When this analysis data is considered, it can be concluded that the results most accurately correlating with the experimental results can be achieved with an element edge length in the range from 0.5 up to 0.75 mm. Furthermore, it should be noted that the utilization of elements with edges shorter than 0.5 mm will, in the case of the herein studied geometries, result in extensive

computation times.

Table 4.9. Mesh sensitivity analysis for hexahedral (brick) elements with merged nodes.

Element length, mm	Elements	Nodes	f_1, Hz	e_{r_Base}, %	$e_{r\_FreeEnd}$, %
2	960	5629	503.32	6.91	6.13
1.75	1296	7471	532.69	1.25	0.46
1.5	1600	9119	540.11	0.14	0.93
1.25	2304	12907	544.05	0.86	1.65
1	3600	19819	525.13	2.68	1.89
0.75	6400	34618	534.79	0.85	0.06
0.5	14400	76519	534.28	0.95	0.16
0.25	52620	300619	539.45	0.01	0.80

Table 4.10. Mesh sensitivity analysis for hexahedral (brick) elements with glued volumes.

Element length, mm	Elements	Nodes	f_1, Hz	e_{r_Base}, %	$e_{r\_FreeEnd}$, %
2	960	5629	503.62	6.86	6.07
1.75	1296	7471	532.5	1.28	0.49
1.5	1600	9119	540.11	0.14	0.93
1.25	2304	12907	544.05	0.86	1.65
1	3600	19819	525.13	2.68	1.89
0.75	6400	34618	534.79	0.85	0.06
0.5	14400	76519	534.28	0.95	0.16
0.25	52620	300619	539.45	0.01	0.80

Table 4.11. Mesh sensitivity analysis for tetrahedral elements with glued volumes.

Element length, mm	Elements	Nodes	f_1, Hz	e_{r_Base}, %	$e_{r\_FreeEnd}$, %
2	2590	5593	567.97	5.16	5.95
1.75	3362	7218	554.15	2.70	3.49
1.5	4107	8763	542.6	0.60	1.39
1.25	6060	12738	538.63	0.14	0.65
1	9234	19238	544.35	0.92	1.71
0.75	16435	33955	543.65	0.79	1.58
0.5	37750	76496	542.04	0.49	1.28
0.25	148727	300558	543.66	0.79	1.58

In terms of element types, it can be observed that the hexahedral elements result in a somewhat better match with the experimental data ($er_{\_FreeEnd}$ = 0.06% @ 0.75 mm), compared to the tetrahedral ones ($e_{r\_FreeEnd}$ = 1.58% @ 0.75 mm), with identical element edge lengths. It should also be noted that the volume bonding method has no significant effects on the results when element sizes smaller than 1.75 mm are used.

Considering the above reported data, the finite elements selected to be used in the following FE analyses are the hexahedral ones, with an element edge length of 0.75 mm, which results, in turn, in an overall finite element number of 6400, comprising a total of 34618 nodes. In terms of thickness, three layers of brick elements form the piezoelectric material, while the substrate is formed by two layers. In the cases when a specific geometry makes it necessary due to its complex contours, e.g. the introduction of stress concentrators, tetrahedral elements of the same size will be utilized. In order to connect the neighbouring layers, the "glue volumes" method is chosen, since it represents a much simpler and quicker approach with no significant effects on the results.

4.4.2. Stress analysis

A typical PEH, collecting and converting ambient kinetic energy, normally operates in dynamical working conditions which, in turn, cause dynamical stresses to occur within the brittle ceramic material of the piezoelectric layers. As it can be seen from the previously covered state-of-the-art given in Section 2, the fatigue lifetime of PEH devices is rarely considered in the available literature, meaning that the common criteria of maximum power and voltage output are only relevant when the application of such devices is intended for a limited number of operational cycles [15, 80, 110]. When, in turn, a bimorph PEH is designed for wearable technology, or any other dynamical environment application, the aforementioned criteria of maximum voltage and power can be considered viable only in case when the stresses occurring within the piezoelectric layers are below the bending fatigue limit of the respective piezoelectric material. The fatigue limit for PZT-5A, the piezoelectric material used in this work, was determined by Okayasu et al. in their extensive experimental study of PZT fatigue failure characteristics, conducted in 2010, to be R_d = 55 MPa [146]. Although not corresponding exactly to the load cases studied in this work, this value represents the best possible fatigue strength approximation available to date. The stress analysis is used in this framework as a tool for assessing the maximal allowable free end displacement in case of the FUC excitation, as well as for determining the largest applicable tip mass in the case of harmonic excitation, while always keeping the stress levels below the thus defined PZT-5A fatigue limit - therefore ensuring a long-term operation of the device. In order to assess the maximal displacements, the meshed model is then fixed at one end, as described in the previous subsections, while a displacement δ_z, ranging from 0.05 to 1 mm, is introduced at the free end of the considered bimorph, resulting in various stress levels (Figure 4.7a). The maximum bending stress levels within the piezoelectric layers, as derived via the FE analyses, are hence graphically represented in Figure 4.7b. To facilitate the

assessment of the maximum allowable deflection of the considered device, the bending fatigue limit R_d of the piezoelectric material is also marked on the graph. It can be, thus, clearly seen that a tip deflection $\delta_z \sim 1$ mm represents the upper limit for the considered rectangular device. Such a limitation of the initial plucking deflection, assures, therefore, the safe and long-lasting operation of the PEH device.

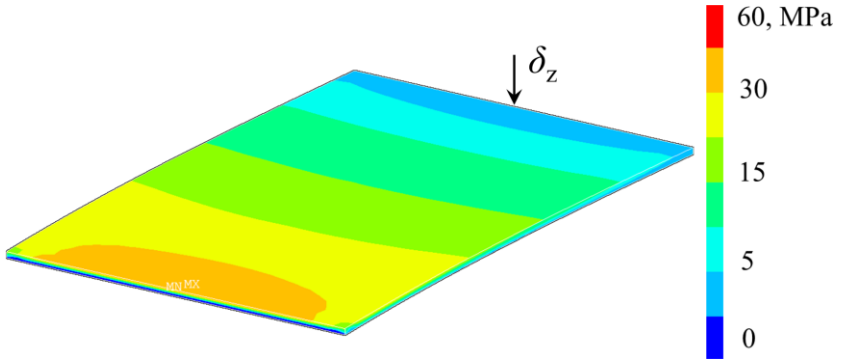

(a)

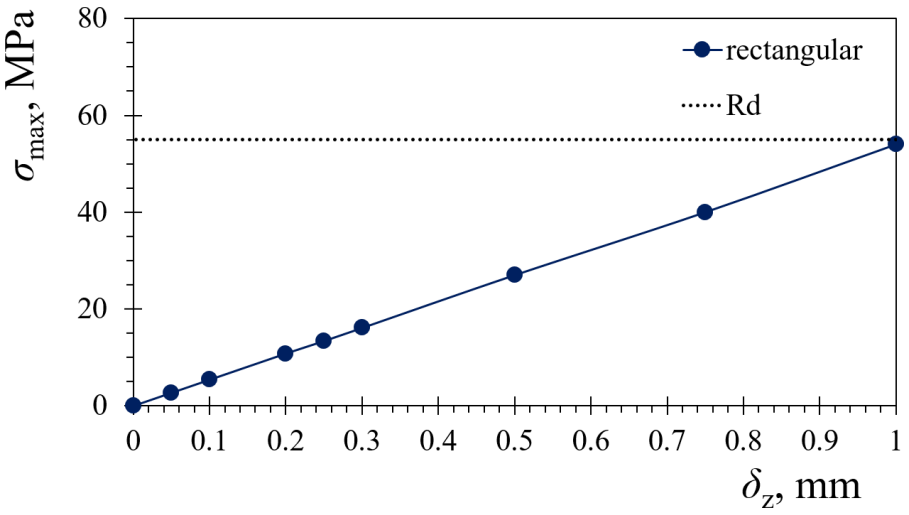

(b)

Figure 4.7. FE stress levels in the PEH piezoelectric layer at $\delta_z = 0.5$ mm (a) and stress levels vs. the free end displacements δ_z (b).

Additionally, stress FE analyses are also beneficial when a tip mass is introduced, in order to determine the largest tip mass a considered PEH can withstand, whilst satisfying the fatigue safety criterion. In this case, the rectangular PEH, equipped with varying tip masses, is subjected in the performed analyses to a harmonic excitation at a 1 *g* acceleration. The thus occurring stress levels are assessed, and the optimal mass value, corresponding to the PZT-5A fatigue limit, is determined. The results of the analyses for the rectangular PEH shape, displayed in Figure 4.8., show that the device is able to securely withstand tip masses of up to $m = 25$ g. It should, however, be noted here that such a tip mass, even if it is made from a high density

material, e.g. tungsten, cannot, due to the resulting size, be suitable for the limited volumes available in wearable applications.

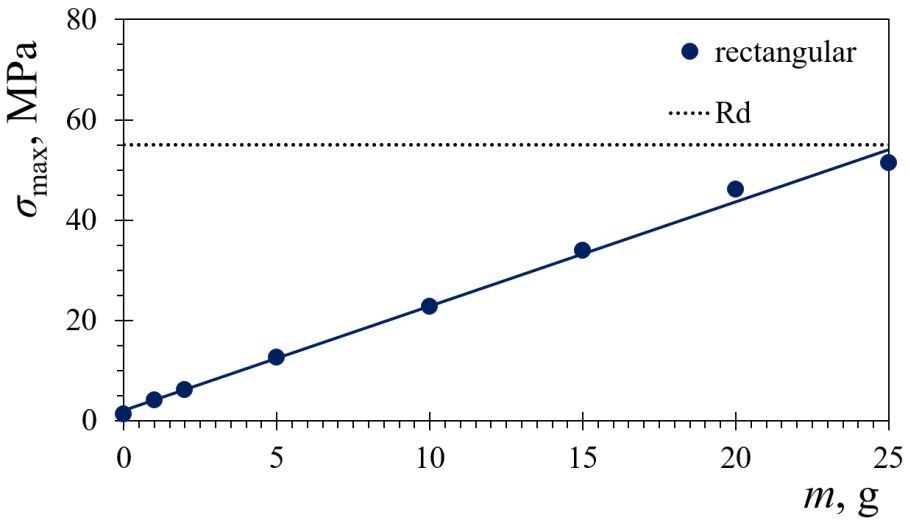

Figure 4.8. FE stress levels corresponding to the respective tip mass values.

4.4.3. Modal analysis

The finite element modal analysis produces the modal response of a studied structure, i.e. the structure's modes of vibration as well as the respective eigenfrequencies. These values, in turn, provide an essential input for the subsequent harmonic analyses in terms of the frequency sweep range, as well as the basis for the assessment of the Rayleigh damping coefficients [27, 68, 220]. Furthermore, the modal response is utilized for the validation of the numerical model via the comparison with the experimental results. Since the largest deformations of the considered PEHs, and thus the highest achievable voltage outputs, occur at the first vibration mode [55, 128, 205], it will be the one mainly considered in this work.

The purely mechanical, i.e., the uncoupled modal response is then achieved by eliminating the effects of electromechanical coupling, by setting to zero the piezoelectricity coefficient e_{31} within the material properties of the piezoelectric layers. As per ANSYS® recommendations, the sparse direct matrix solver - the most robust and least cumbersome solver type available in ANSYS® [22, 55], is employed for this purpose [68]. Additionally, the block Lanczos eigenvalue extraction method, based on the block shifted Lanczos algorithm, is selected, since it is recommended for large and symmetric eigenvalue problems. For the extraction of the requested eigenvalue number, the herein used analysis method employs an automated shift strategy, in combination with the Sturm sequence checks [5]. The model of the PEH is then clamped at one end, the number of modes to extract is selected along with the desired frequency range, and the first two flexural vibration modes, shown in Figure 4.9., as well as their respective uncoupled

eigenfrequencies f_{1_mech} = 534.8 Hz and f_{2_mech} = 3315 Hz are generated. The utilization of these results as inputs for the harmonic analysis and for the purpose of model validation will be described in the following subsections.

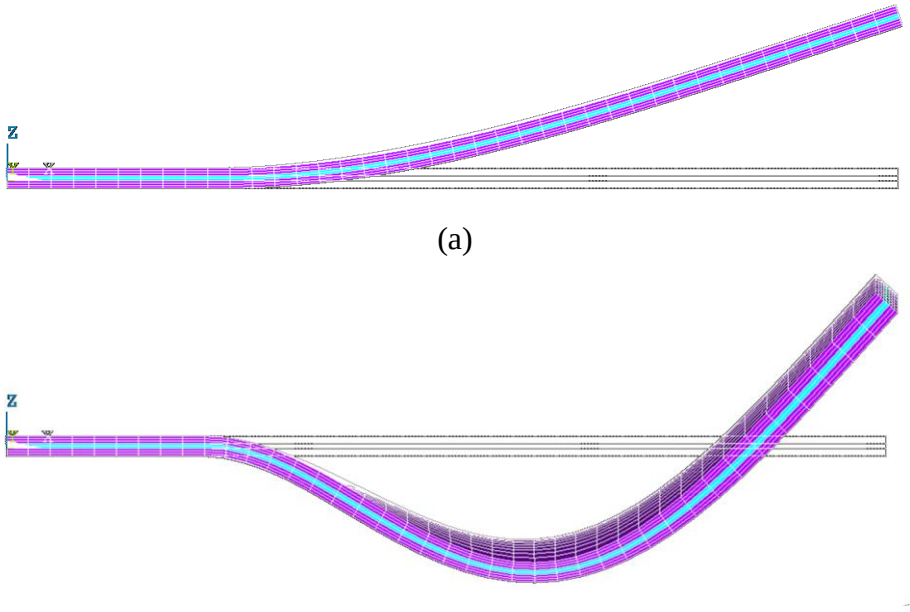

(a)

(b)

Figure 4.9. Rectangular PEH FE modal response: first vibration mode at f_{1_mech} = 534.8 Hz (a) and second vibration mode at f_{2_mech} = 3315 Hz (b), with the reference undeformed shape.

4.4.4. Harmonic analysis

A coupled harmonic analysis, solving the time-dependent motion equations for linear structures undergoing steady-state vibrations [5], is carried out subsequently to the modal one in order to assess the coupled electromechanical response, i.e., the coupled frequency response functions (FRFs) of the studied bimorph PEHs. For this purpose, the same boundary conditions as in the modal analysis are applied to the FE model at the clamped and the free end, with the addition of the previously removed piezoelectricity coefficient e_{31}. The load is introduced in the form of a 1 *g* acceleration along the vertical *z* axis, and a frequency sweep around the first uncoupled eigenfrequency f_{1_mech} = 534.8 Hz, previously determined via the modal analysis, i.e., from 480 Hz up to 600 Hz is, thus, utilized. The introduction of a CIRCU94 finite element, to serve the function of a variable resistor (electrical load), coupled to the piezoelectric layers using the aforementioned VOLT DoFs, simulating a parallel connection, enables the obtainment of the voltage outputs, as shown in Figure 4.10., with the boundary conditions at one of the two nodes set to zero before initializing the analysis [25, 68]. The resistance value at the CIRCU94 finite element is set in a way that it matches the internal resistance of the PEH, i.e., the optimal load resistance, R_{Lopt} = 5 kΩ, thus maximizing the PEH's conversion efficiency as

well as its power output [160]. This value is assessed, due to the complex effects induced by the forward and the backward electromechanical coupling effects, via the well-established practice of performing multiple harmonic analyses with varying load resistance values [20, 71, 78, 134]. The known approximate equation for the assessment of optimal resistance [144, 231], results, in turn, in a value for a single work-point, i.e., a single set of working conditions, and it is, therefore, not used in this work.

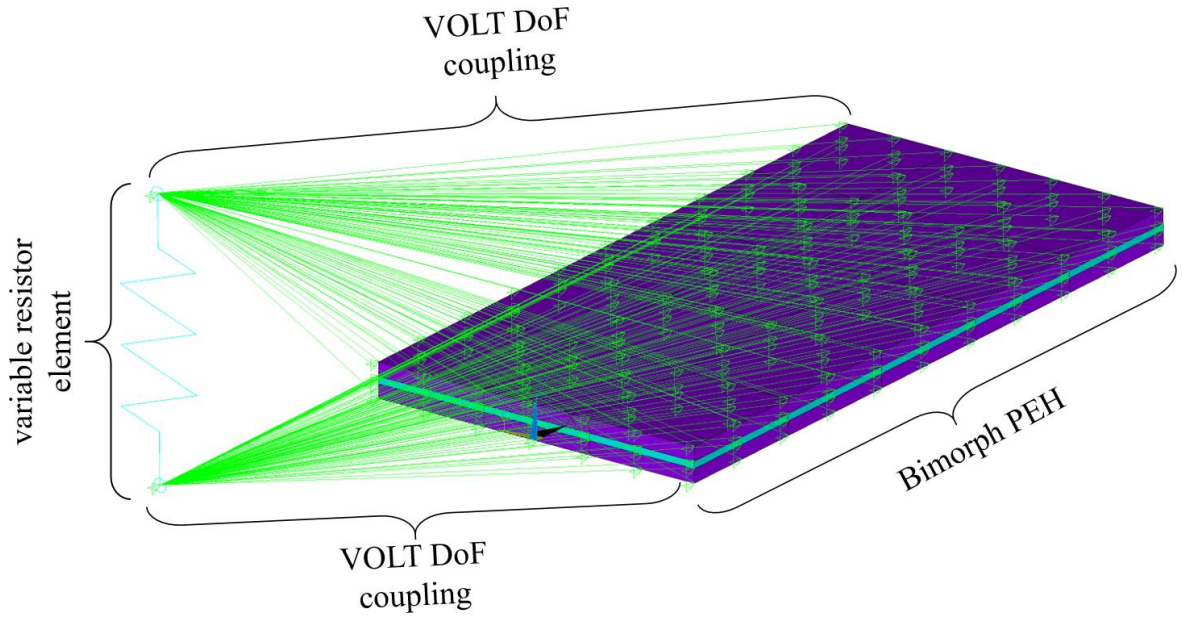

Figure 4.10. FE rectangular PEH model coupled with the variable resistor element.

In order to carry out the harmonic analysis, the damping present in the studied system needs to be defined as well. This very complex phenomenon can be approximated, due to the not yet entirely explored energy dissipation problem, utilizing the Rayleigh damping model, commonly employed in FE analyses [191]. Rayleigh damping is therein defined by the damping matrix $\mathbf{B}_d$, a sum of the mass $\mathbf{M}$ and stiffness $\mathbf{K}_S$ matrices, which are, in turn, multiplied by the damping constants α and β, respectively, as shown in the following expression [5, 68, 191]:

$$\mathbf{B_d} = \alpha\mathbf{M} + \beta\mathbf{K_s} \tag{4.3}$$

The damping constants α and β are calculated from the experimentally assessed damping coefficient ζ and the first two uncoupled eigenfrequency values f_{1_mech} and f_{2_mech} as determined from the modal analysis, using the following expressions [5, 68, 191]:

$$\frac{\alpha}{4\pi f_{1\_mech}} + \beta\pi f_{1\_mech} = \zeta \tag{4.4}$$

$$\frac{\alpha}{4\pi f_{2\_mech}} + \beta\pi f_{2\_mech} = \zeta \tag{4.5}$$

The experimental assessment of the damping ratio is done by measuring and recording the

pure mechanical response of the bimorph PEHs. In this work, two different excitation methods are used in order to generate and acquire the response data, i.e., the excitation by plucking the harvester free end, as well the excitation of the clamped base. In the first case, the PEH is excited by plucking the free end, and it is then left to oscillate at its eigenfrequency. On the other hand, the base excitation process, offering a better control of the excitation process, is achieved by using an electrodynamic shaker with a 3D printed PEH fixture, operating at the eigenfrequency of the studied PEH. At a certain moment, the shaker is stopped and the bimorph PEH is left to oscillate freely, similarly as in the previous case. A Metrolaser® vibrometer [130] is used in both approaches to capture the displacement of the PEH free end, and the PEHs are not connected to an electrical load, thus ensuring an uncoupled, i.e. pure mechanical response. An example of the uncoupled response for a plucked rectangular PEH is shown in Figure 4.11.

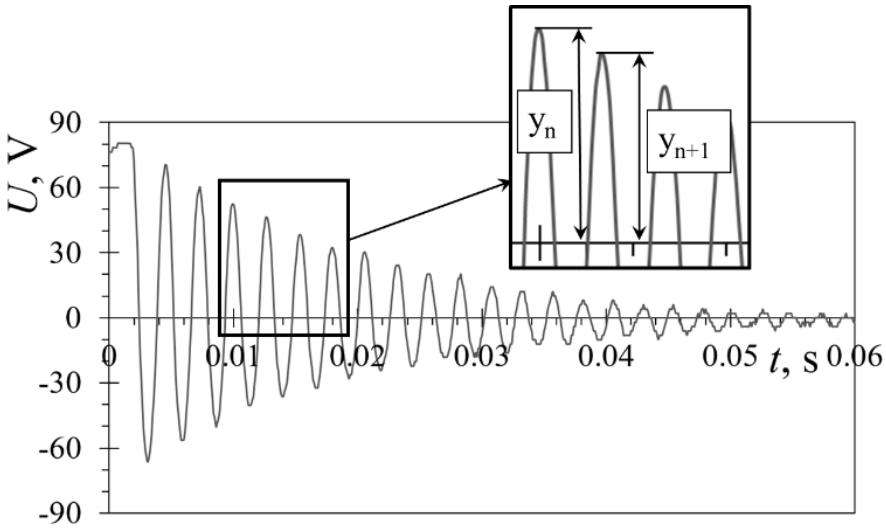

Figure 4.11. Typical mechanical response obtained by plucking the PEH free end.

The thus acquired data is then used to assess two consecutive response peaks y_n and y_{n+1}, as shown in Figure 4.11., enabling the calculation of the logarithmic decrement δ_{log} as [5, 128]:

$$\delta_{log} = \ln\left(\frac{y_n}{y_{n+1}}\right) \tag{4.6}$$

The damping ratio ζ can, in turn, be calculated by using the following expression:

$$\zeta = \frac{\delta_{log}}{\sqrt{4 \cdot \pi^2 + \delta_{log}^2}} \tag{4.7}$$

When comparing the damping ratios for the herein studied rectangular PEH, obtained by the two different approaches, i.e. by plucking the free end and via base excitation using the shaker, a small difference of 3% is detected, i.e., $\zeta = 0.031$ ($\sigma_{sd} = \pm 0.0089$) for the plucking approach, and $\zeta = 0.03$ ($\sigma_{sd} = \pm 0.0064$) when the PEH is excited using a shaker. These values are, in turn,

utilized for the calculation of the previously described Rayleigh damping constants, to be used in the FE coupled harmonic analysis. The resulting coupled harmonic response of the studied rectangular PEH, i.e., the electromechanical FRFs attained via the FE harmonic analysis, can be seen in Figure 4.12., where a maximum voltage output of U_{max} ~ 1.39 V is generated at a coupled eigenfrequency of f_{1_coup} = 544 Hz.

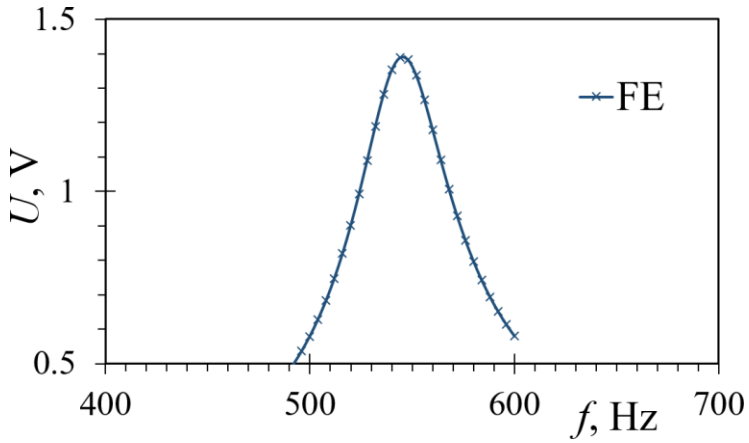

Figure 4.12. FE coupled electromechanical response of the studied rectangular PEH at its optimal load resistance.

The significant difference (~ 10 Hz) between the coupled and the uncoupled eigenfrequencies is expected and it is to be attributed to the effects of electromechanical coupling, i.e., to the influence of the electrical parameters on the mechanical response of the considered device. The described method and the attained results will be used for validating the numerical model, by comparing them with the experimental coupled harmonic responses. The experimentally validated model will, then, be utilized for the assessment of the optimal load resistance values for all the optimized PEHs with varying geometries [20, 78, 134]. The same basic FE model, together with its boundary conditions, i.e., the used material properties, the clamping, the electromechanical coupling and the load resistances, will also be used in the subsequent transient FE analysis.

4.4.5. Transient analysis

To simulate the process of plucking PEH excitation and generate the respective coupled responses, a transient analysis solution method is used. This method models the dynamical responses of the harvester under forced excitation in precisely defined discrete time increments, and it hence generates steady state results for every time iteration [27]. The PEH model is, again, very similar to the previous analyses, having the same basic geometry, material properties and boundary conditions, i.e., the clamping and coupling conditions, but differing in the excitation method. The excitation of the studied device model is, induced in this case through

three transient analysis steps, as shown in Figure 4.13.

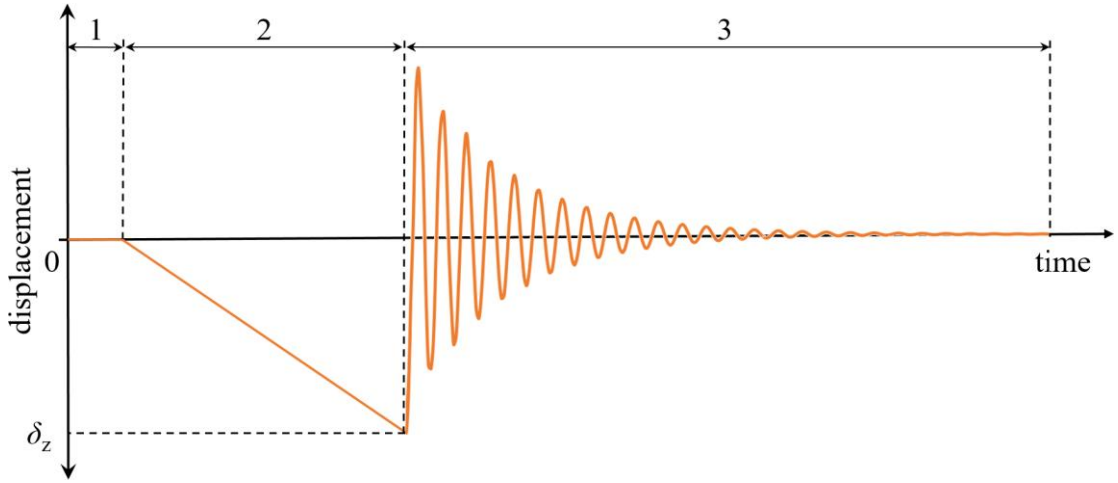

Figure 4.13. FE coupled transient analysis load steps: initial (approach) start time step (1), free end displacement ramped load (2), and transient response (3).

After a short initial start time step (1), representing the plectrum approach, a displacement along the vertical *z* axis, δ_z = 0.6 mm, is gradually introduced, i.e., the load is ramped over a pre-set time period denoted as (2), simulating the gradual bending of the PEH free end using a plectrum. The lower than optimal tip displacement is selected in order to avoid overstressing the PEH due to the extensive adjustments and tuning of the plucking experiments. At the end of this time interval, the load is removed, i.e., the displacement is set back to zero, and the PEH model is left to oscillate freely at its eigenfrequency within a time interval marked as (3), longer than the oscillation period of the PEH itself, in order to capture the entire response. The analysis time step Δt = 0.0001 s is set close to the value suggested in literature [5], calculated via:

$$\Delta t = \frac{1}{20 \cdot f_{\max}}, \tag{4.8}$$

where f_{max} is the frequency of the highest mode of interest, i.e., in this case the first eigenmode.

Damping is, in turn, defined again through the same Rayleigh damping constants α and β, introduced in the FE model as the damping coefficients ALPHAD and BETAD. The 2nd order transient integration parameters ALPHA and DELTA, together with the 1st order transient integration parameter THETA, required by the analysis algorithm, are defined based on the ANSYS® piezoelectric analysis recommendations, i.e., they are accordingly set as 0.25, 0.5 and 0.5 [5, 27, 68]. The coupled electromechanical response, i.e., the voltage output for the studied rectangular PEH, is acquired at the nodes of the variable resistor element, set at the PEH optimal load resistance value of R_L = 5 kΩ, and it is displayed in Figure 4.14. The thus attained FE results show a maximum peak-to-peak voltage $U_{p\text{-}p\_FE}$ = 21.26 V, generated at the beginning of the 0.05 s oscillation period. The average power output, based on the generated RMS voltage,

can then be calculated by using the expression [28]:

$$P = \frac{U^2}{2R_{\mathrm{L}}}, \quad \text{where } P = \frac{U_{\mathrm{RMS}}^2}{R_{\mathrm{L}}} \text{ and } U_{\mathrm{RMS}} = \frac{U}{\sqrt{2}} \tag{4.9}$$

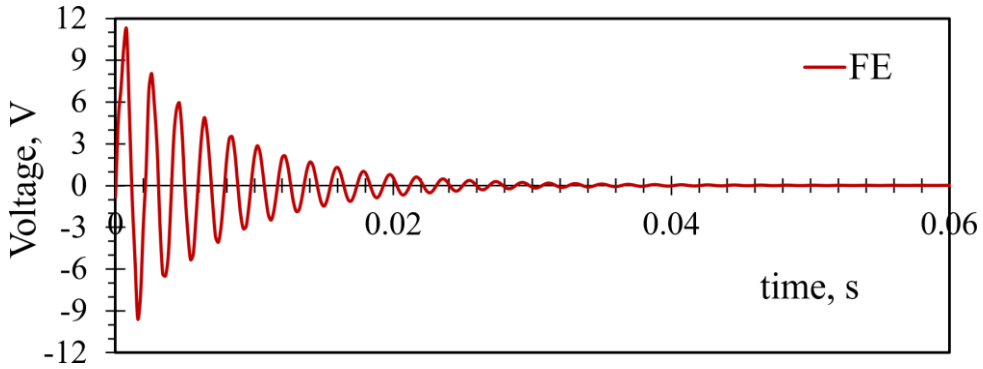

Figure 4.14. FE coupled electromechanical transient response for a plucked rectangular PEH.

The average power generated within the cited time interval is $P_{\mathrm{av\_FEA}}$ = 0.454 mW, while the maximal attainable power output, generated at the beginning of the oscillation period is found to be $P_{\mathrm{max\_FEA}}$ = 12.53 mW. These results are, in turn, used for the experimental validation of the numerical model, as well as for the subsequent comparison with the optimized PEH shapes. In addition, a comparison between a linear and nonlinear transient analysis is also carried out for the rectangular PEH, with no significant difference in their respective responses [68].

4.4.6. Clamping conditions and effects

Numerous approaches to the clamping of cantilever-type structures have been extensively studied and used in the past. A comprehensive overview of the commonly utilized clamping methods was given by the National Physics Laboratory in 1956 [140]. Although the paper is focused on the leaf-spring elements of flexure pivots, the same guidelines can be applied to the clamping of piezoelectric bimorph cantilevers. A generic example of clamping plates is displayed in Figure 4.15a, representing the most common fastening method. In this case, special care needs to be taken in order to ensure the flatness of the clamping surfaces. Rough and unequal surfaces could affect the free working length of the cantilever, thus exceeding the length measured from the clamping point to the cantilever tip [140]. This would, in turn, significantly affect the PEH response in terms of its eigenfrequency, as well as of the voltage outputs. Alternative clamping methods, based on clamping plates, are shown in Figures 4.15b and 4.15c. In both of the alternative approaches the clamping plate contacts the cantilever at its front edges,

ensuring, thus, that the free length is as close as possible to the nominal value. Such methods typically employ set screws for clamping, and dowel pins for accurate location [140].

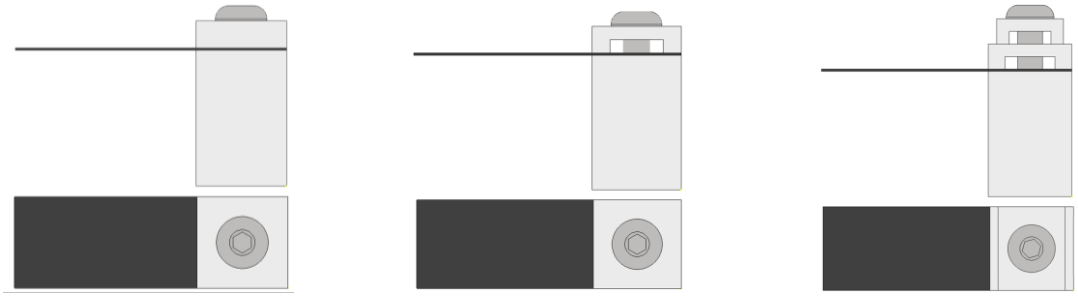

(a) (b) (c)

Figure 4.15. PEH fastening methods using conventional clamping plates (a), alternative clamping plates using a single clamp (b), and double clamps (c) [140].

Additional clamping methods, aimed at applications where the rigidity of the clamped cantilever is not of critical importance, are also possible [140], e.g. clamping by deformation, inserting a wedge in the slot or filling the slot with solder. It should be noted that it is impossible to avoid the creation of a solder fillet, which could affect again the free working length of the clamped cantilever [140]. Due to the pronounced PEH sensitivity to the cantilever free end length, these methods are not suitable for piezoelectric energy harvesting applications. Given these considerations, a clamping method closely resembling the approach illustrated in Figure 4.15b is employed in this work in the form of specially designed 3D printed clamping plates. The stress induced in the piezoelectric layers due to the pressure applied during clamping is not considered in this work and it should be taken into account in future research.

This section provided a comprehensive description of the numerical and experimental methods used in this work for the development of an optimized PEH device. A short chronological outline of the most prominent mathematical models was given, and a complex numerical modelling approach, comprising stress, modal, harmonic, as well as transient analyses was presented. The section also provided a detailed description of the harmonic and FUC experimental setups, employed within this work, as well as covered the essential characteristics of their main components. Issues concerning the clamping area and the effects of different clamping conditions were also addressed.

The optimization process applied to the design parameters of bimorph PEHs will be described next. The initial studies of the suggested novel PEH shapes, as well as the detailed portrayal of the DoE optimization process and its results will also be included. A comprehensive stress analysis will also be carried out to determine the maximal allowable mechanical loads applicable to the optimized PEH shapes, while assuring fatigue safety and long-term operation.

5. PEH DESIGN PARAMETERS ANALYSIS AND THEIR INFLUENCE ON PERFORMANCE

The charge generated within the piezoelectric layers of a kinetic energy harvester, resulting in the device's voltage output, occurs because of the mechanical strain caused by a bending moment, which is, obviously, linearly decreasing from the clamping point towards the free end of the bimorph [97, 160, 197]. It is, therefore, possible, according to recent literature [22, 84, 121, 150], to positively affect the performance of a PEH by altering the shape of the device. Based on the conclusions emerging from the state-of-the-art, thoroughly covered in Section 2, an innovative approach to the design of miniaturized PEHs combining the methods of segmenting a device into multiple differently tuned cantilevers and topology optimization of the individual segments is devised. This is achieved by optimally dividing a rectangular bimorph cantilever into two trapezoidal and one inverted trapezoidal shape. An additional shape is also suggested, comprising an optimized triangular notch at the clamped end of a rectangular PEH. In both cases, the FUC, i.e. plucking excitation method, in the form of a compact wearable (watch-like) mechanism, is selected in order to overcome the issues arising from random human motion (cf. Section 2). This section will thus thoroughly cover the study of PEH geometrical design parameters and their influence on the performances of the piezoelectric energy harvesters through the complex numerical modelling described in Section 4, coupled to an optimization procedure based on DoE algorithms. Initial studies of novel segmented and notched PEH shapes will therefore be performed to test the viability of the suggested design approach, i.e. the combination of segmentation, topology optimization and FUC excitation. The optimization process and the FE analyses will result in two separate optimized PEH designs. Additionally, extending the current state-of-the-art and complementing it with a crucial, yet generally neglected aspect, the stress analysis of all the devised shapes will be carried out to ensure that the stress levels within the piezoelectric layers do not exceed the dynamic limits of the utilized material, thus providing a significant design and scientific contribution to the field of study of optimized PEH configurations.[4]

[4] Part of the work described in this section was published by the author of the thesis and his collaborators in a peer-reviewed scientific paper [70], as well as an international conference paper [69], produced and published as part of the obligations foreseen in the curriculum of the doctoral study of the Faculty of Engineering of the University of Rijeka, Croatia, and hence this section is based, partly directly derived and cited from this work. All the numerical and experimental data, relevant for this work, is available online at https://repository.riteh.uniri.hr/islandora/object/riteh:2274.

5.1. Initial studies

The limited volume, typically available in miniaturized wearable devices, strongly favours energy sources with a higher energy density. With that in mind, and building upon previous research reported in literature [20, 22, 68, 102, 119], a novel approach to PEH design is suggested in this work, embracing a multiple cantilever harvester segmented into optimized shapes, excited via a FUC mechanism. The herein proposed innovative approach comprises the merger of three design paths promising notable increases in performance, i.e. segmenting the device into multiple cantilevers [121], topology optimization of the individual segments using different shapes [22, 84, 150] and stress concentrators [24] as well as excitation via a frequency up-conversion mechanism [156, 159, 219], previously not used in combination. A small size conventional rectangular PEH, suitable for integration into a compact watch-like wearable device, serves as a basis for the processes of segmentation and optimization, while also providing a reference frame in terms of performances and forming a size limiting design framework. For the purpose of initial evaluation of the suggested design approach, three PEH variations are generated from the rectangular device (Figure 5.1a), thus having a similar overall surface area [54], i.e. a device segmented into two trapezoidal and one inverted cantilever (Figure 5.1b), a rectangular PEH with a V-shaped notch added at the clamped end as a stress concentrator (Figure 5.1c) as well as a segmented PEH with added stress concentrators (notches) (Figure 5.1d).

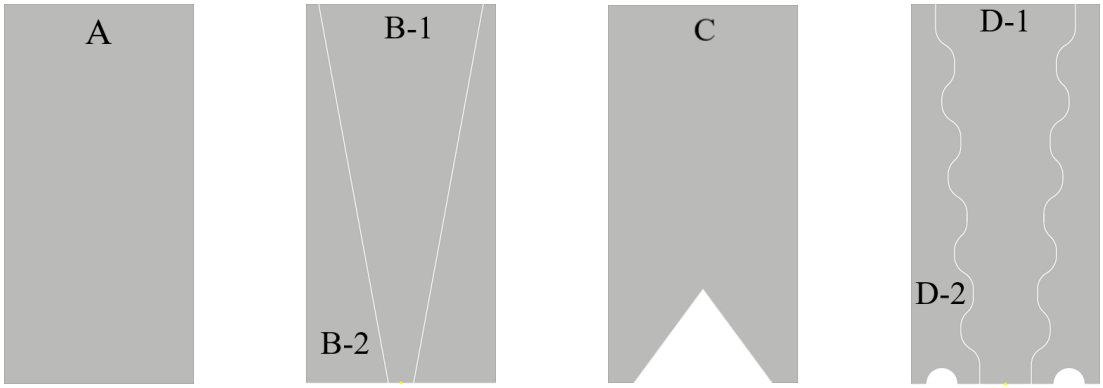

Figure 5.1. Conventional rectangular PEH shape a) and the geometry variations derived from it: segmented PEH shape b), notched PEH shape c) and the segmented shape with added stress concentrators d).

According to the strength of materials theory, the trapezoidal shape displays an almost uniform stress distribution and thus a higher charge (voltage) generation [22, 197]. Counterintuitively, it was shown that, due to the increased stress levels around the narrow clamped end, an inverted shape is able to provide an even higher voltage output [22]. The innovative approach

presented in this work aims to utilize the advantages of both trapezoidal and inverted shapes, packed into a rectangular footprint, comparable to that of a conventional device.

In order to study their respective performances and thus the viability of the proposed design approach, these devices are tested using the modal and harmonic FE analyses (cf. Section 4), while maintaining constant boundary conditions, i.e. clamping, coupling and a sinusoidal excitation at 1 g, as well as the previously selected 0.75 mm finite elements. The preliminary results are displayed in Figure 5.2. in terms of specific power, i.e. power normalized over the surface area of the respective device (e.g. B-1 power output over the B-1 surface area), as evidenced in Section 2, since the layer thicknesses are identical for all the considered PEHs. The performances of the novel shapes are shown in comparison with the rectangular one denoted as (A) cf. Figure 5.1. The summed up outputs of all three segments (B1+2B2 and D1+2D2) are not displayed in the graph since the individual segments oscillate at different eigenfrequencies.

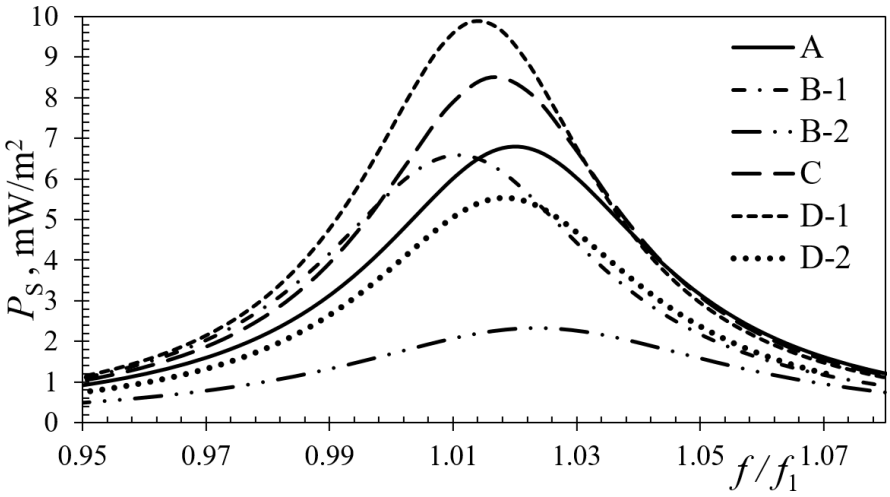

Figure 5.2. Preliminary specific power outputs of the proposed PEH shapes compared to the conventional rectangular shape.

A general trend showing performance gains can thus be observed from these results, namely that the straight-edged inverted trapezoidal shape, denoted as (B-1), displays a slightly lower output, comparable to that of the rectangular shape. What is more, when the relatively low outputs of the two additional trapezoidal shapes, denoted as (B-2), are added to the inverted shape, the overall performance of the design solution proposed in Fig. 5.1b shows a notable improvement over the conventional rectangular shape. The notched shape, denoted as (C), displays an evident trend in performance gain compared to the rectangular shape, as well as to the straight-edged segments. When the segments with added stress concentrators are considered, the inverted shape (D-1) clearly outperforms the rectangular shape, while the output of the trapezoidal one (D-2) is slightly below it. When, however, the performance of the two trapezoidal segments is added to that of the inverted one, a further performance gain can be observed. The

preliminary results presented above confirm the claims presented in recent literature, thus supporting the conclusions arising from the state-of-the-art analysis, provided in Section 2. The distinct trend in performance improvement, achievable via the suggested novel design approach, can be observed, justifying, therefore, the need for further research and a thorough analysis of the PEH design parameters via optimization of their geometrical proportions as well as the introduction of FUC excitation as the means to overcome the issues related to random excitation by human motion, which will be presented in the subsequent subsections.

5.2. DoE and optimization

To maximize the energy density, and thus the power output of the studied devices, the proportions of the segments, and of the notch, i.e., of the respective defining dimensions need to be optimized. To facilitate the optimization process and reduce computation requirements, the well-known symmetry conditions are applied to the segmented shape, performing the calculations only on one half of the overall structure. In each of the studied cases, i.e., the segmented and notched shape, two defining dimensions are then selected. In the case of the segmented shape, the selected variables *x* and *y* define the angle of the diagonal cut delineating the division of the constituting shapes, i.e., the shape and the size of the two segments, as illustrated in Figure 5.3a.

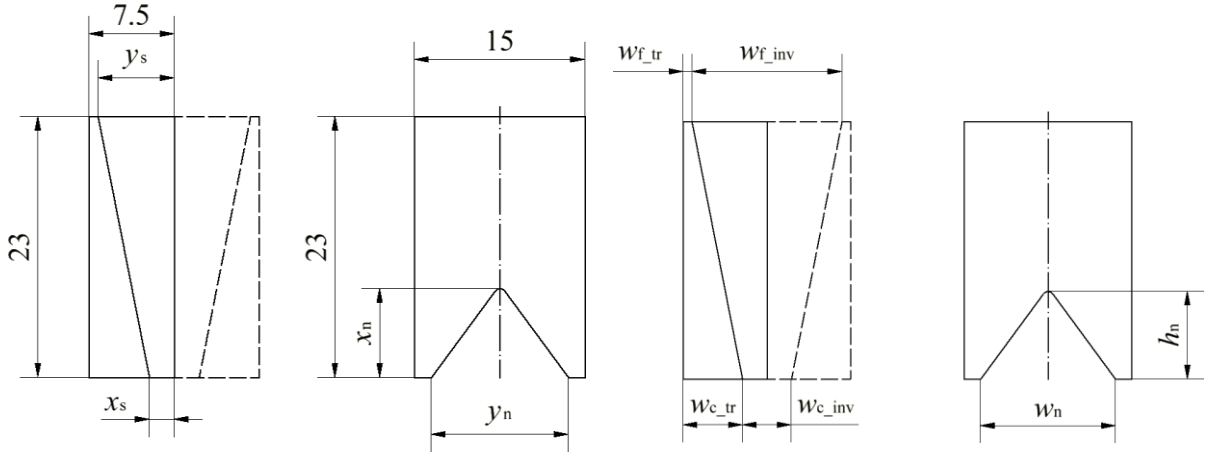

Figure 5.3. Dimensions defining the proportions of the proposed shapes: segmented a) and notched b) [73] and the resulting dimensions of the optimized segments c) and notch d).

When the notched shape is considered, the *x* and *y* variables define, in turn, the width and heights of the V shaped notch at the clamped end, as shown in Figure 5.3b. The starting point for the optimization process is a commercially available rectangular bimorph cantilever consisting of a t_S = 0.15 mm thick stainless steel substrate layer and two t_{PZT} = 0.254 mm thick

piezoelectric layers made from the PZT-5A piezoelectric ceramic material [153]. The overall dimensions of the rectangular bimorph are w = 15 and l_0 = 30 mm, with 7 mm being used for clamping, resulting in a free end length of l = 23 mm. The material properties of both the PZT-5A and the stainless steel are provided in Table 4.5. given in Section 4. The continuous x and y variables are then subjected to an optimization approach combining, as will be described below, a design-of-experiments (DoE) central composite design, the response surface methodology and the previously described harmonic FE analyses.

5.2.1. Design-of-experiments

Design-of-experiments (DoE) is a methodology used to investigate any system with a response varying as a function of one or several variables [123]. It allows the study of complex problems, with multiple variables affecting the response, and interacting with each other [123], while concurrently aiding the reduction of the possibility of bias and systematic errors through the process of randomization [39]. The response surface methodology (RSM) is, in turn, utilized to study the way the response of a system depends on some influencing quantitative factors, as well as to experimentally determine the region of the response where the conditions close to the optimal ones are achieved, i.e., to estimate the minimum or the maximum response of a studied system [32, 33]. The shape of the response can often be approximated by a quadratic function, and the estimation of the variables, i.e. those defining the size of the segments and notches, leads to the identification of the extreme. If this point falls outside of the considered variable ranges of the influencing parameters, additional work is required, since the extrapolation is not considered reliable due to the sensitivity of the utilized model [39]. As the number of required experiments rapidly increases with the number of influencing factors (dimensions of the design space), RSM is typically applied, especially when used in industrial applications, to a smaller number of factors [32-33]. The most commonly used RSM variants include the Box-Behnken design [39-40] and the central composite design (CCD) [39-40]; the latter is able to fit a full quadratic model, and is thus utilized in the herein considered case, since the effects of only two factors are being considered [33, 99].

5.2.2. Optimization using DoE

For each of the considered shapes, a CCD for two continuous factors is used to generate random combinations of the x and y variables, i.e., of the shape-defining dimensions. For this purpose, a continuous range of values needs to be defined for each factor, with particular attention devoted to their upper and lower limits, so that an adequate space may be ensured for

clamping at the base, as well as for securing the tip mass at the free end [73]. A 3D model is then created for each of the random *x* and *y* combinations using a modelling software, and several FE studies using ANSYS® are performed, comprising the above described modal and harmonic analyses, as well as the numerical assessment of the respective optimal resistance values for each individual shape. These studies provide, in turn, the maximum power output values, generated by each variation of the segments and of the notch size, at their optimal load resistance values. By pairing the thus attained results with the appropriate random combinations of *x* and *y*, response surfaces can be created, and regression equations can thus be generated for each of the studied cases [73]. It should be noted here that, in case of the segmented shape, two separate models are used for every *x* – *y* combination, representing each individual segment and the respective optimal resistance value, and the maximal power output is assessed for both of them [73]. These two separate output values are then summed up before being paired with the respective *x* – *y* combination, representing the combined total power generated by the studied segmented shape [73]. The resulting regression Equation 5.1, representing the segmented shape, as well as Equation 5.2, representing the notched shape, portray, therefore finally, the quadratic models describing the influence of the *x* and *y* dimensions on the power output of the studied PEH. The determination coefficient obtained for the model describing the segmented shape R^2 = 81.42%, shows a relatively high predictive accuracy of the quadratic model, describing thus more than 81% of the studied parameters' variance, while the determination coefficient for the notched shape is even higher, R^2 = 96.46%. The most significant residual plots for both cases are shown in Figure 5.4.

$$P_{\text{seg}} = 26.5 + 7.95x + 15.2y - 2.17x^2 - 0.97y^2 - 0.974xy \tag{5.1}$$

$$P_{\text{notch}} = 125.73 + 3.42x - 0.42y - 0.3012x^2 + 0.331y^2 + 0.042xy \tag{5.2}$$

The residuals represent the difference between the measured data and the data predicted (fitted) by the regression model [48, 123]. The frequency of residuals plot for the segmented shape (Figure 5.4a) displays a close to normal distribution with a slight skew to the left, while in the case of the notched shape the plot (Figure 5.4c) also shows a close-to-normal distribution, and it seems to be more centred. When the residuals vs. fitted values plots are analysed, in both cases (Figures 5.4b for the segmented shape and Figure 5.4d for the notched shape) a random distribution of points is obtained. Based on these observations, it can be concluded that the quadratic models describing the behaviour of the studied PEHs, are not distinctly biased, i.e. the models do not favour one portion of the analysed data [48, 123].

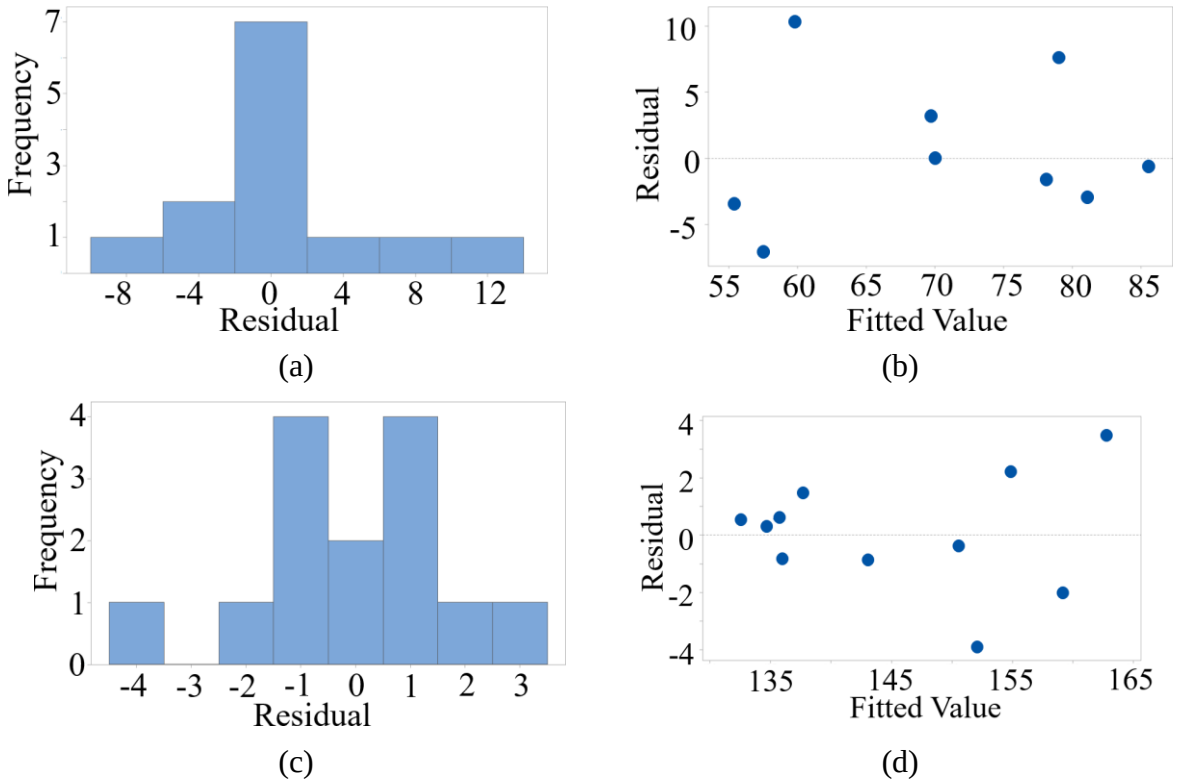

Figure 5.4. Residual plots for the segmented shape: frequency vs. residuals (a), and residuals vs. fits (b), and for the notched shape: frequency vs. residuals (c) and residuals vs. fits (d).

An optimization algorithm, using the Generalized Reduced Gradient (GRG2) code-based optimization algorithm [138], is then applied to the above listed regression equations, aimed at ascertaining the combinations of the *x* and *y* variables resulting in the maximum output power generated by the respective PEHs. The resulting response surface plots, showing the influence of the studied design parameters on the PEHs' power outputs, are displayed in Figure 5.5a for the segmented shape and in Figure 5.5b for the notched one [73].

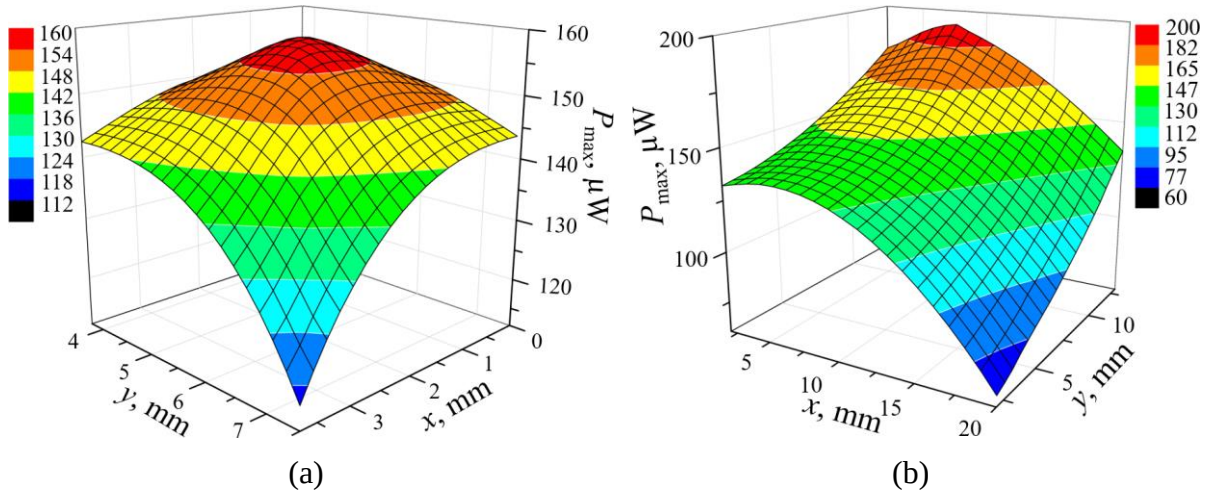

Figure 5.5. Response surface plots of the maximum power output of the segmented PEH (a) and of the notched PEH (b) [73].

In the case of the segmented shape, a clear maximum can be observed, while for the notched shape the maximum clearly occurs outside of the considered variables' range. The reason for this arises in the need to ensure enough space for clamping the device, which is reflected in the limited width of the V shaped notch [73].

The optimal values x_s = 1.5 mm and y_s = 7 mm are thus determined for the segmented shape, shown in Figure 5.3a [73], resulting in the wide, i.e., free end width of w_{f_inv} =14 mm, and in the narrow, i.e., clamped end width of w_{c_inv} = 3 mm for the inverted trapezoidal segment, denoted as (B-1). For the trapezoidal segment, denoted as (B-2), the width of the narrow, i.e. free end is w_{f_tr} = 0.5 mm, while the width of the wider, i.e. clamped end is w_{c_tr} = 6 mm (Figure 5.3c). When the notched shape, displayed in Figure 5.3b, denoted as (C), is considered, the optimal values of x_n and y_n directly define the dimensions of the notch, resulting in a width of w_n = 11 mm and the respective height h_n = 6.5 mm (Figure 5.3d) [73].

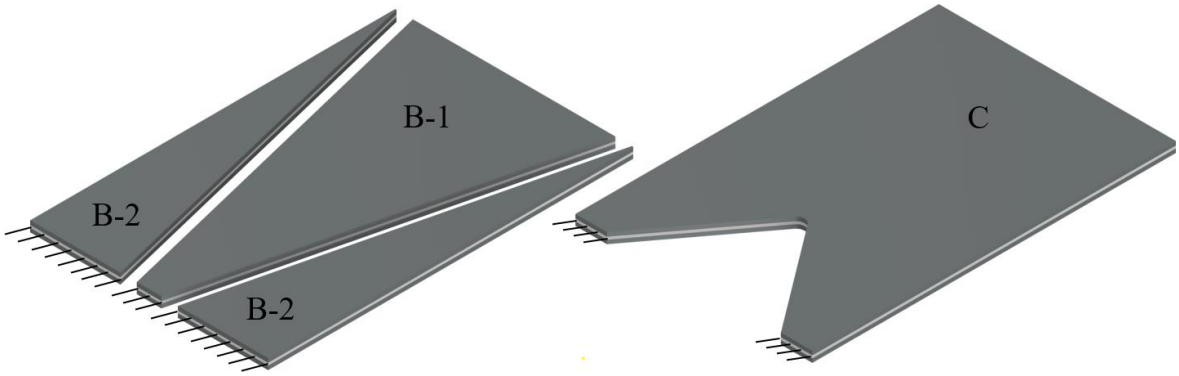

(a) (b)

Figure 5.6. PEH shapes generated via the optimization process: segmented PEH shape (a) and notched PEH shape (b).

3D models of the optimized PEH shapes are generated next and the FE analyses, including modal, coupled harmonic and coupled transient are carried out. The maximum and specific power outputs for both segments of the segmented PEH, where the values for the trapezoidal segments comprise the sum of the power outputs of both such segments, as well as for the notched PEH, obtained via the coupled harmonic analyses at their respective optimal resistance values, are listed in Table 5.2., where they are also compared with the values obtained with the conventional rectangular shape. As it can be observed from the provided data in terms of maximum power P_{max}, the notched PEH noticeably outperforms the rectangular one, while the inverted segment displays a comparable performance. The power generated by the trapezoidal segments, although being significantly lower than those of the rectangular PEH, should be seen as an addition to the power generated by the inverted segment, thus resulting in total in a sizable

improvement in performance. When considering the specific powers P_S, normalized over the respective PEH surface area, both the notched shape and the inverted segment by itself clearly outperform the conventional rectangular device. As in the previous case, the underperforming trapezoidal segments should be seen as an addition to the inverted one, further improving the performance of the segmented shape [73].

Table 5.1. FE modal and harmonic analyses results for the studied PEH shapes [73].

	R_L, kΩ	P_{max}, μW	P_S, mW/m^2
Trapezoidal	7	26.3	175.5
Inverted	12	131.5	672.7
Notched	7	168.9	545.9
Rectangular	5	141.3	409.5

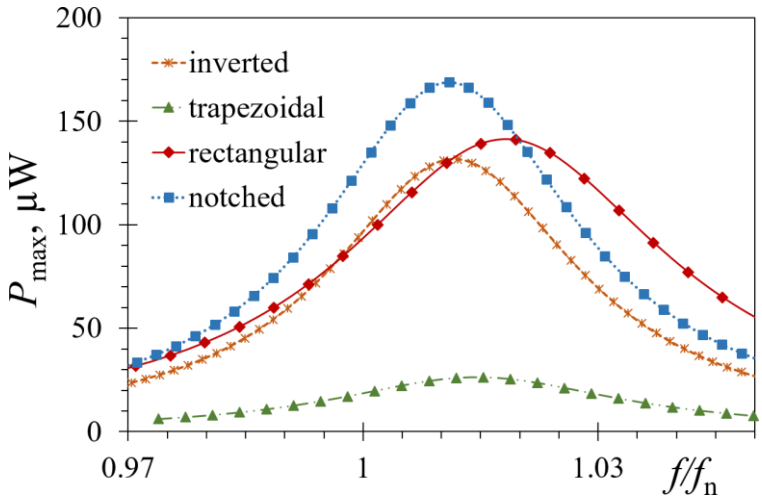

(a)

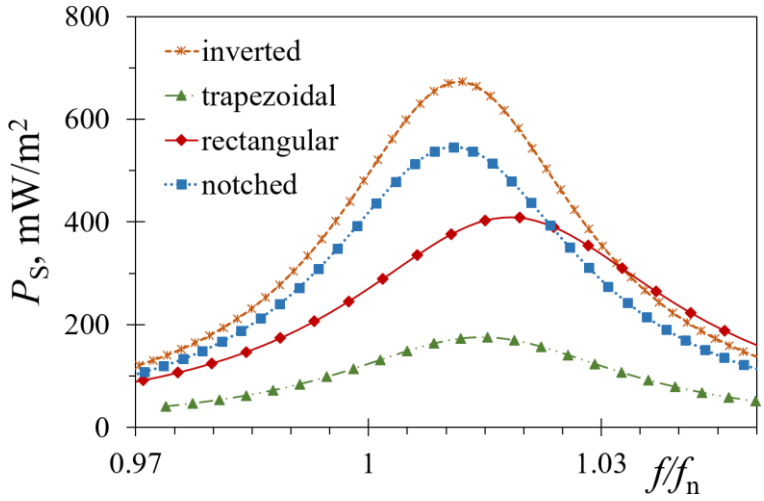

(b)

Figure 5.7. Optimized PEHs' performances compared to those of the conventional device in terms of the maximal (a) and specific power outputs (b) [73].

The PEH performance comparison in terms of the maximal output powers is graphically represented in Figure 5.7a, while the one showing the specific powers is given in Figure 5.7b.

Transient analyses of each optimized shape are also performed, aiming to simulate the mechanism of plucking the PEH free end. The study of the effects of the FUC excitation mechanism on the response of the optimized PEHs is thus enabled [73]. As described in Section 4, in the transient analyses the boundary conditions and the material properties are kept the same as in the modal and harmonic ones, with the load being introduced as a δ_z = 1 mm deflection of the free end along the vertical *z* axis, applied to all the considered cases. After the desired deflection has been achieved, the PEHs are left to oscillate at their respective eigenfrequencies. The resulting coupled transient voltage responses for both segments of the segmented device, as well as for the notched PEH, are displayed in Figure 5.8. in comparison with the conventional rectangular shape [73]. In terms of the peak-to-peak voltage $U_{p\text{-}p}$, the performances of the inverted segment ($U_{p\text{-}p}$ = 137.6 V), shown in Figure 5.8c, are comparable to that of a rectangular shape, displayed in Figure 5.8a ($U_{p\text{-}p}$ = 161.5 V) [73]. What is more, when the voltage generated by the two trapezoidal segments, shown in Figure 5.8b, ($U_{p\text{-}p}$ = 94.3 V for each segment) is added to that of the inverted one, the segmented shape displays a significant increase in the voltage output [73]. The peak-to-peak voltage output generated by the notched PEH ($U_{p\text{-}p}$ = 133.3 V), shown in Figure 5.8d, while being comparable to the inverted shape, is somewhat lower than that of the rectangular PEH [73].

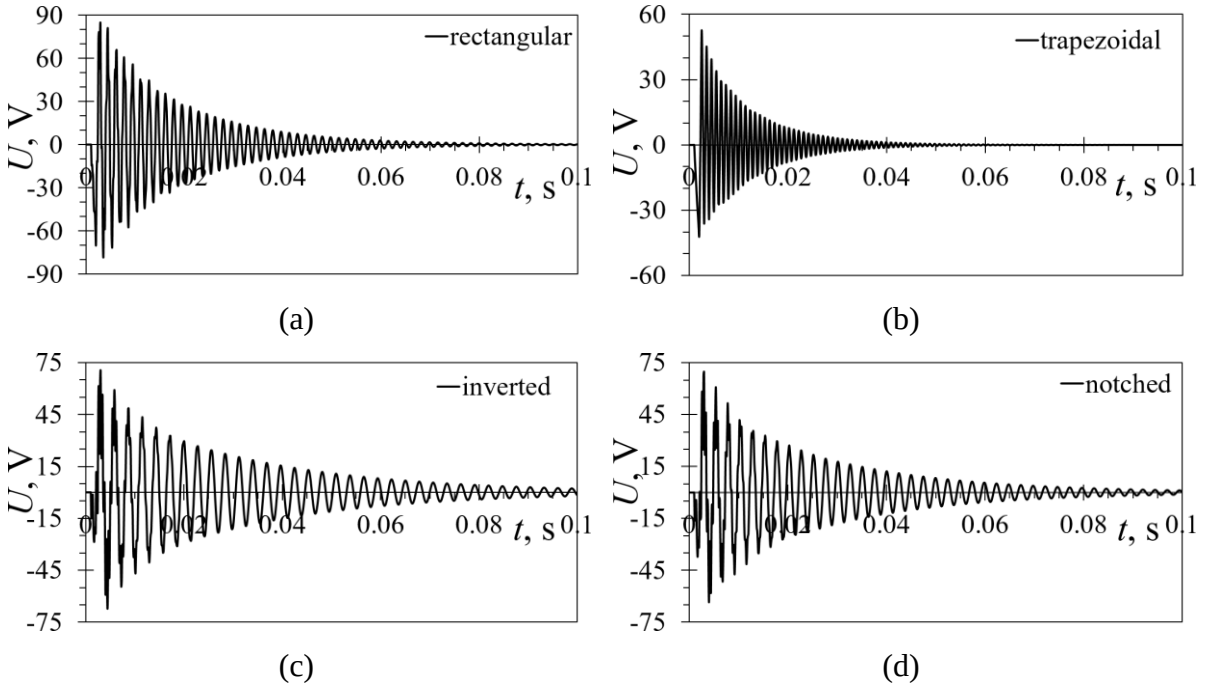

Figure 5.8. Transient voltage responses of a rectangular PEH (a) in comparison with the optimized PEH shapes: trapezoidal (b), inverted trapezoidal (c) and notched (d) [73].

These results clearly support, thus, the viability of PEH geometry optimization aimed at performance improvement, but also shows the functionality of FUC excitation applied to optimized segmented devices, as well as the viability of such a combination for overcoming the issue of random excitation.

5.2.3. Strength analysis of the optimized PEH shapes

The dynamical working conditions present during regular operation of all kinetic energy harvesters induce dynamical stresses in the brittle piezoelectric ceramic material used in the piezoelectric layers of the PEH bimorphs. If an autonomous PEH powered wearable device is to be employed in real life applications, and thus it is expected to operate over a fairly long time period, special attention should be devoted to the fatigue lifetime of the PEHs subjected to dynamical loads, typically neglected in available literature. In fact, available literature [15, 80, 110] generally refers to maximal performances in terms of voltage and power outputs as the only criteria for PEH design and analysis, which can be significant only in cases when a very small number of operational cycles is required for a specific application. When PEHs are used for practical applications, e.g. for powering wearable or other devices operating in dynamical working conditions, the aforementioned criteria of maximum voltage and power no longer suffice, and stress levels occurring within the piezoelectric layers need to be taken into account in order to ensure a long-term operation of the device. For that purpose, the fatigue limit R_d = 55 MPa for the piezoelectric material PZT-5A, utilized in all the herein studied devices, is introduced as a design criterion [146]. The primary aim of the stress analyses performed in this frame using ANSYS®, described in more detail in Section 4, is the assessment of the maximal loads, i.e., of the maximal free end displacements and tip masses, applicable to the optimized PEHs while keeping the stress levels below the fatigue limit. A variation of the segmented shape, comprising wavy contours, i.e., notches along the edges of the optimized segments, as it is depicted in Figure 5.9., is also introduced here.

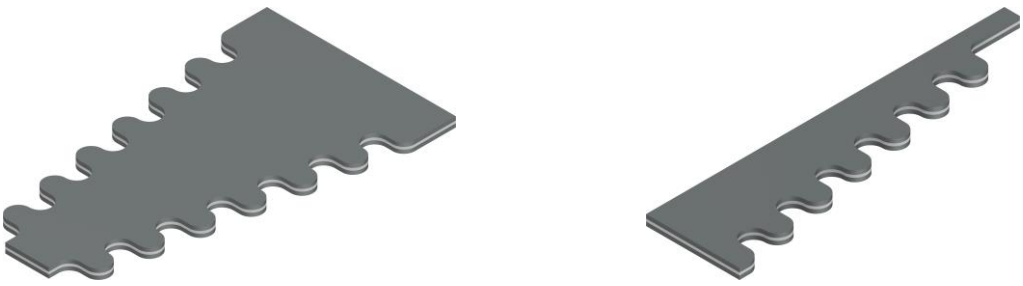

(a) (b)

Figure 5.9. Stress concentrators applied to the edges of the optimized inverted trapezoidal (a) and of the optimized trapezoidal segments (b).

These notches should, as it was implied by the results presented in the initial studies, allow a further increase in performances of the optimally segmented PEHs. It is thus assumed that the performance gain in terms of voltage and power will be induced by an increased charge generation within the piezoelectric layers due to an increase in the localized stress levels and to the increased compliance. The increased local stress supports, in turn the need for a further comprehensive strength analysis. As in the rest of the herein performed FE analyses, the boundary conditions and material properties are kept constant, as described in Section 4, for all the studied PEH shapes, while a displacement load, in the form of a free end deflection δ_z ranging from 0.05 up to 1 mm along the vertical *z* axis, is introduced to simulate the initial free end deflection occurring during the plucking process. The distribution of the thus obtained stresses across the studied PEH shapes, for a free end deflection of δ_z = 0.5 mm, is shown in Figure 5.10.

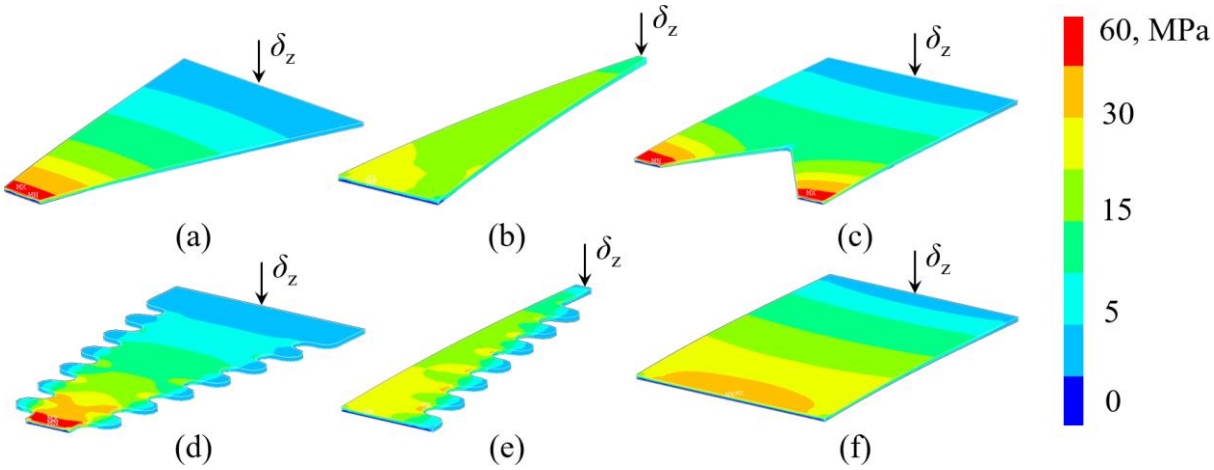

Figure 5.10. FE calculated stresses in the piezoelectric layers of the PEHs for a δ_z = 0.5 mm free end deflection: inverted (a), trapezoidal (b), notched (c), wavy inverted (d), wavy trapezoidal (e), and conventional rectangular shape (f).

In all the considered cases, the highest stress levels occur near the clamped end, i.e. around the fixture. A more uniform stress distribution can, in turn, be observed along the trapezoidal segments shown in Figures 5.10b and 5.10e, with clearly visible locally elevated levels present around the stress concentrators, moving away from the clamping area. The maximum bending stresses σ_{max} obtained for the respective PEH shapes via the performed FE analyses are then displayed in Figure 5.11. in relation to varying deflections of the free end δ_z. The fatigue bending limit of the used piezoelectric material PZT-5A is also marked on the graph in order to facilitate the assessment of the maximal allowable tip deflections for all the studied shapes. It is thus established that, if the stress levels are to be kept below the fatigue limit, a maximal tip deflection of ~ 0.5 mm can be safely applied to the notched shape. The inverted trapezoidal shape is able to withstand safely a tip deflection of ~ 0.6 mm, both with and without stress

concentrators. The largest tip deflection, applicable to both the trapezoidal shape with stress concentrator as well as to the conventional rectangular shape, is found to be ~ 1 mm, while the straight-edged trapezoidal shape is able to withstand an even larger tip displacement, i.e., up to ~ 1.4 mm. If the initial deflections, used in the process of plucking the PEH free end, are limited to the above given values, the fatigue safety of the piezoelectric layers is therefore ensured, thus enabling a long-term operation of the overall device. The impact of the herein given considerations on the performances of the studied devices will be clearly visible in the FUC results presented in the following section.

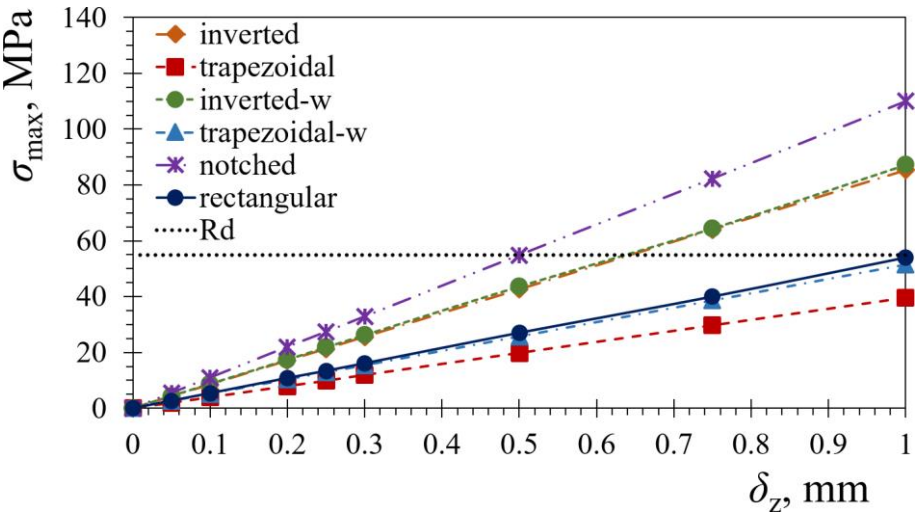

Figure 5.11. Piezoelectric material bending stresses for the considered PEH shapes vs. the tip deflections δ_z.

Additional FE analyses are carried out to study how the addition of various tip masses influences the stress levels within the piezoelectric layers of optimized PEHs, subjected to a 1 *g* harmonic excitation. The optimal values for tip masses can thus be determined for each of the considered PEH shapes. The FE results, showing the maximum stresses in relation to the tip mass values, are given in Figure 5.12., where it can be seen that the largest tip mass that can be applied to the trapezoidal shape is m = 9 g. The inverted trapezoidal shape, is, on the other hand, able to withstand a significantly smaller tip mass of only m = 4 g, while a slightly larger mass m ~ 4.5 g can be safely attached to the inverted trapezoidal shape with added stress concentrators. Both the notched and inverted shape with added concentrators can withstand a tip mass of m ~ 6 g, while a m = 25 g can be used with the rectangular shape, as it is shown in Figure 4.9. in Section 4. However, such a mass cannot possibly be packed in a volume suitable for the limited space available in a practical wearable watch-like device, even if it was manufactured using high-density materials, such as tungsten. As every variation of tip mass values results in a significant change in PEH behaviour, supplementary harmonic FE analyses are carried out

next for all the considered PEH shapes with respective optimal tip masses attached at their free ends.

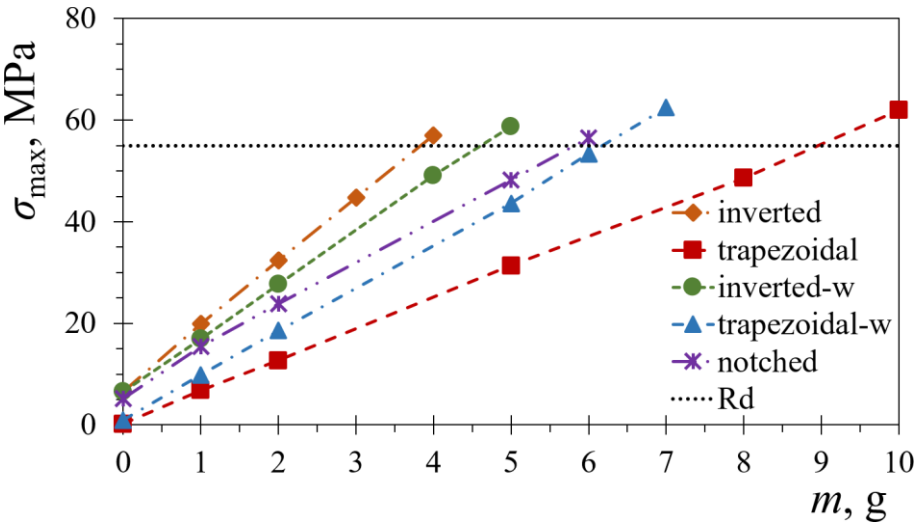

Figure 5.12. Piezoelectric material bending stresses of the considered PEH shapes vs. the tip masses m, for PEHs subject to a 1 g harmonic excitation.

Optimal load resistance values are then determined by sweeping through the R_L values ranging up to 125 kΩ, and the respective maximal power outputs P_{max}, mW are assessed for each individual shape, as shown in Figure 5.13a. These power values are then normalized by the tip mass value P_S, mW/g (Figure 5.13b), and by the respective PEH surface area P_S, mW/mm^2 (Figure 5.13c). As it is clear from Figure 5.13., the highest performances in terms of the maximal powers P_{max} (Figure 5.13a) are achievable with the rectangular shape equipped with a m = 25 g tip mass; however, as it was already pointed out, such a configuration would be unsuitable for wearable applications due to the excessive volume of the said tip mass. In terms of generated power, only the rectangular and the combined trapezoidal PEHs, both equipped with fairly large tip masses, are able to generate enough power to meet the ~ 5 mW required by the device suggested in Section 3. When the power outputs normalized over the tip mass values are considered (Figure 5.13b), the best performances are shown to be achieved by combining the output of the two trapezoidal segments, with the output of a single trapezoidal segment being comparable to that of the rectangular shape. The overall behaviour of the studied devices remains similar when the power values are normalized by the surface area of the respective PEHs (Figure 5.13c), i.e., the highest output values are, again, found to be generated by the combination of the two trapezoidal shapes. Figure 5.13a also shows that the performances of most of the optimized shapes, i.e., the inverted trapezoidal, the notched and both the variants with added stress concentrators, are smaller compared to the rectangular shape, which can be attributed to the limited ability of these shapes to withstand heavier tip masses during long-term operation.

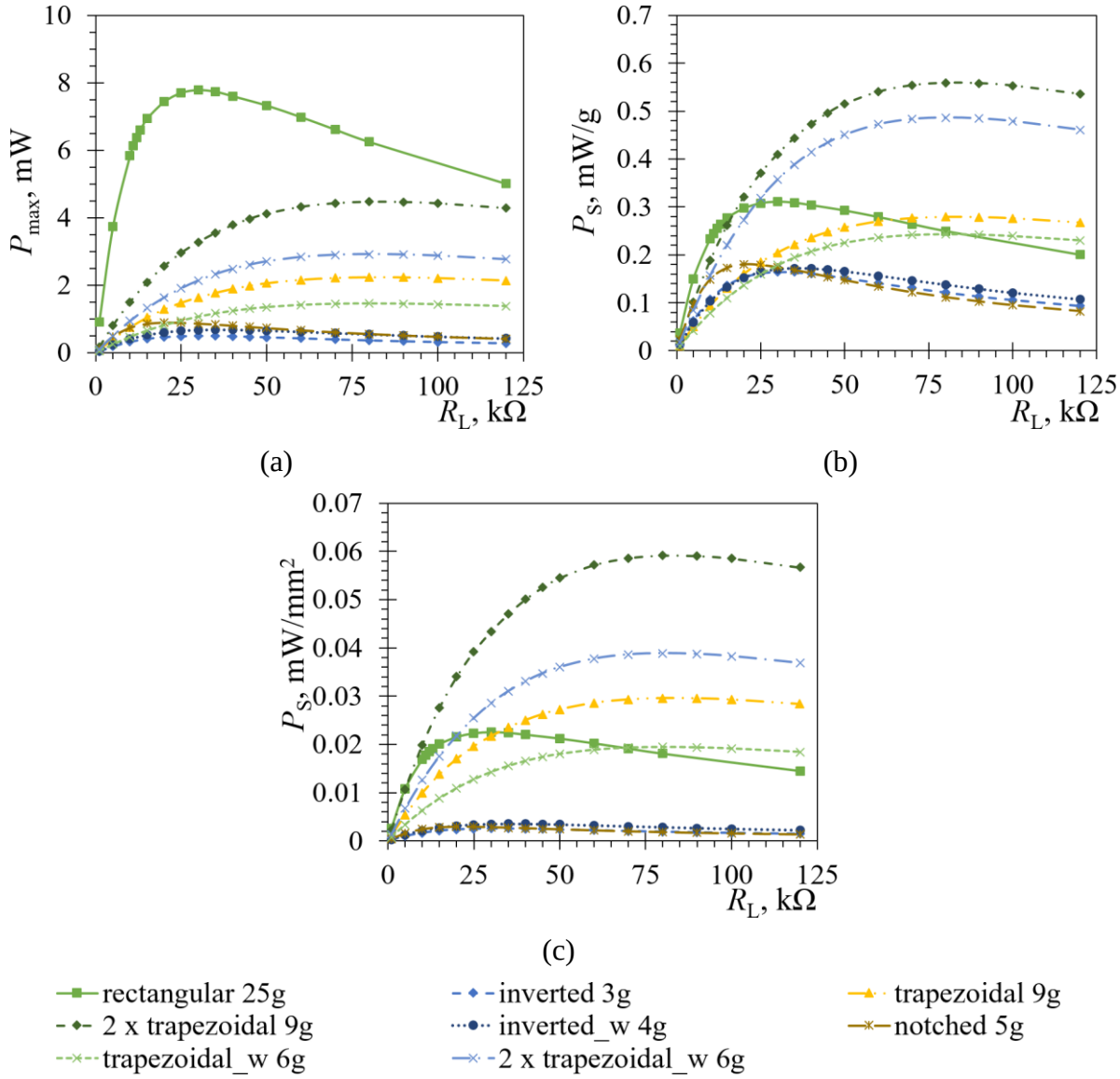

Figure 5.13. Coupled harmonic responses of the various PEH shapes with optimal tip masses m vs. R_L: P_{max} (a), P_S normalized by m (b), and P_S normalized by the PEH surface area (c).

It is in any case clear that, when the specific design requirements of practical wearable PEHs are taken into account, in terms of the required high power density with, concurrently, low masses and volumes, as well as the limited tip deflections, the segmented PEH shape could certainly represent a viable solution for power generation. The studied optimized devices with power output ranges of up to several mW could, with a careful approach to the selection of electronic components, e.g. selecting an economical communication protocol combined with a smart power management design that makes use of periodical data transfer, potentially provide enough power for an autonomous wearable device, e.g. ~ 5 mW, as required by the example presented in Section 3.

This section provided a comprehensive representation of the PEH shape optimization process based on the analysis of the design parameters and their influence on PEH responses. Initial studies of novel PEH shapes were covered, paving the way towards more detailed analyses. The basics of the utilized DoE methodology were provided and a detailed step-by-step description of the optimization process was given, including the definition of variables, the used DoE randomization, the subsequent FE analyses, as well as the creation of the resulting response surfaces and the extraction of the respective regression equations, to which the optimization algorithm was applied. The resulting optimized shapes were analysed using the complex FE approach comprising modal, harmonic and transient analyses, and the thus attained responses were compared to the conventional rectangular shape, showing a significant improvement in performances. A stress analysis was also carried out to determine the maximal allowable free end displacement and tip mass values for each considered shape, ensuring in this way that the stress levels within the piezoelectric layers did not exceed the fatigue limits of the material.

In the subsequent section, the experimental validation of the used FE models will be provided. Additionally, EH devices, manufactured according to the previously determined optimized dimensions, will be studied and their performances in terms of output voltages and powers will be experimentally assessed, considering the stress limits of the utilized piezoelectric material. A comparison with the conventional rectangular PEH will also be given, providing, thus, the means for the critical analysis of the attained results.

6. EXPERIMENTAL MEASUREMENTS

If the results of a numerical model are to be considered reliable, an experimental validation needs to be carried out. Experimental measurements of the responses of the rectangular PEH are performed by using the two setups described in Section 4 and the thus attained results are compared to those obtained via the FE analyses. The 3D models used in these FE analyses are corrected according to the measurement of the commercially available PEH layer thicknesses. The energy harvesting devices developed by using the optimization process and the now validated model, are manufactured from commercially available rectangular PEHs using a precision cutting technology. Their responses are experimentally assessed via the aforementioned setup, and compared to FE results. The devices are then compared among themselves as well as to the reference rectangular PEH in terms of the maximal, average and specific power outputs[5].

6.1. Experimental validation of the FE model

The experimental validation of the herein used numerical models is performed by experimentally assessing the modal, harmonic and transient responses of the commercially available rectangular PEH, manufactured by Piezo.com [153] using the two setups (see Section 4) and comparing them to the results obtained via the FE analyses. The 3D models used in these analyses have to be corrected in terms of layer thicknesses, described in detail in the following subsection, in order to bring them as close as possible to the actual dimensions of the PEHs used in the experiments.

6.1.1. Layer thickness measurement

In order for the PEH behaviour to be accurately modelled, a precise measurement of the thickness of the substrate and the piezoelectric layers are carried out at the Precision Engineering Laboratory [200]. The Olympus® SZX16 optical stereomicroscope [164], equipped with a digital camera [46], as shown in Figure 6.1a, is thus employed to acquire a set of images, using

[5] Part of the work described in this section was published by the author of the thesis and his collaborators in a peer-reviewed scientific paper [70], produced and published as part of the obligations foreseen in the curriculum of the doctoral study of the Faculty of Engineering of the University of Rijeka, Croatia, and hence this section is based, partly directly derived and cited from this work. All the numerical and experimental data, relevant for this work, is available online at https://repository.riteh.uniri.hr/islandora/object/riteh:2274.

a 180x magnification. The images are, in turn, analysed via a calibrated image analysis software [45]. An example of such an image is shown in Figure 6.1b.

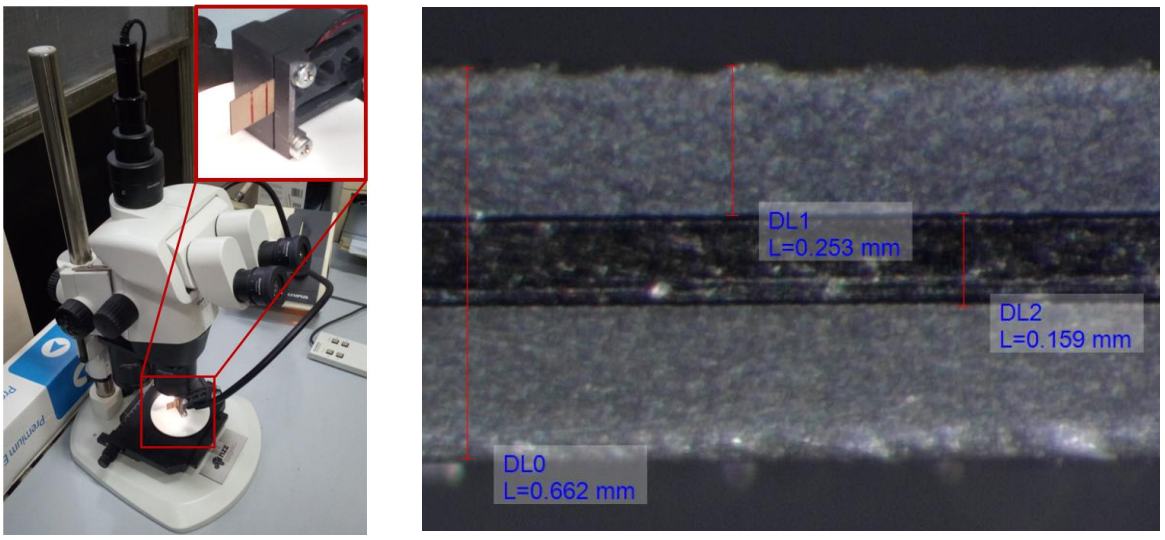

(a) (b)

Figure 6.1. PEH thicknesses image acquisition using the Olympus® SZX16 optical stereomicroscope (a), and an example of an image used for layer thickness measurements (b).

Based on a simple statistical analysis, it is hence concluded that a bimorph PEH model with a metallic substrate layer thickness t_s = 0.163 mm (σ_{sd} = ± 0.0043 mm) and a piezoelectric layer thicknesses t_{PZT} = 0.251 mm (σ_{sd} = ± 0.0045 mm) display an adequate accuracy in simulating the behaviour of the studied devices. A small discrepancy in layer thickness is, however, noticed when the results are compared with the nominal values provided for the commercial PEH, as reported in Section 5, i.e., t_S = 0.15 mm and t_{PZT} = 0.254 mm [153]. Due to an exponential correlation between the PEH thickness and the respective area moment of inertia of its cross-section, this has a noticeable impact on the device's dynamical response [75, 118].

6.1.2. Model validation

The first step in validating the numerical models describing the behaviour of a PEH is to perform a modal analysis. For this purpose, one end of the PEH is clamped to a fixed and rigid base, while the free end is subjected to an impact excitation and it oscillates at its eigenfrequency. The device is not connected to a load, to avoid the effects of electromechanical coupling [55]. The mechanical or uncoupled eigenfrequency of the PEH is assessed using the Metrolaser® Vibromet 500V laser Doppler vibrometer [130] (see Section 4) in combination with the respective NI LabVIEW® VI [141]. The thus obtained results, compared to the FE analysis modal responses, are listed in Table 6.1., where a close match can be observed. In fact, the

numerical value of $f_{1\_mech\_FEA}$ = 534.8 Hz is shown to differ from the experimentally assessed value of $f_{1\_mech\_EXP}$ = 535.1 Hz (σ_{sd} = ± 1.04) by only 0.056%.

Table 6.1. Rectangular PEH uncoupled eigenfrequency values

	$f_{1\_mech\_FEA}$, Hz	$f_{1\_mech\_EXP}$, Hz	Diff.
Rectangular PEH	534.8	535.1 (σ_{sd} = ± 1.04)	0.056%

As it was described in Section 4, a harmonic analysis consists of inducing a sinusoidal excitation at the clamped base of the PEH, while sweeping through an excitation frequency spectrum around the previously determined first uncoupled eigenfrequency of the studied device, while keeping a constant acceleration. The boundary conditions (excitation, clamping distance and parallel coupling) present in the model are set as close as possible to the experimental ones, with the assumption that the electrical connections and the electrodes have zero resistance, i.e., they are considered ideal. Several harmonic analyses are then performed with varying load resistance values, with the goal of determining the optimal R_L value resulting in the highest generated power. From the graphical representation of the thus obtained data (Figure 6.2.), it can be deduced that for the studied rectangular PEH shape subjected to a sinusoidal excitation of 1 *g*, the maximum power is generated at the optimal load resistance value of R_{L_opt} = 5 kΩ.

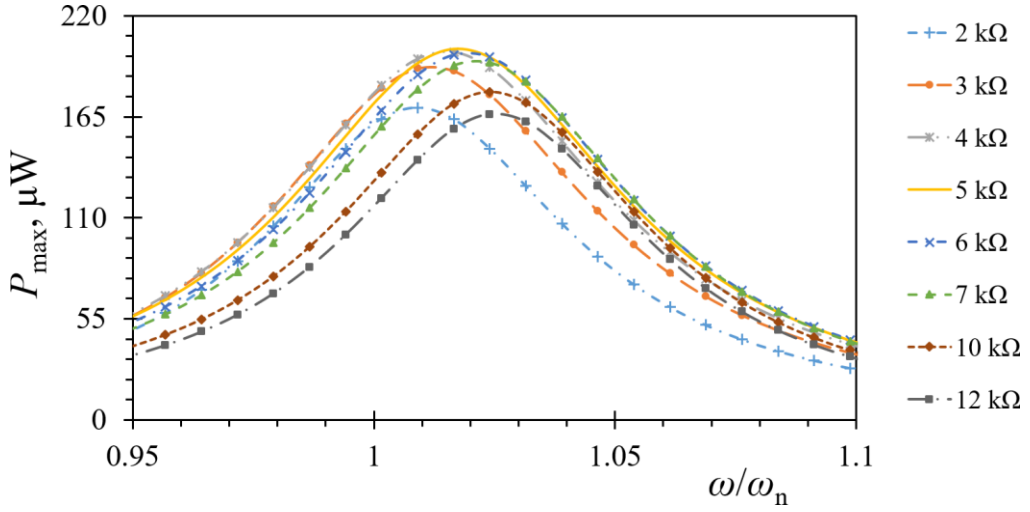

Figure 6.2. FE obtained powers at various load resistance values.

The experimental harmonic response obtained at the optimal load resistance using the setup described in Section 4, is displayed, in comparison to the respective FE data, in Figure 6.3a, where a close match can be observed in terms of the maximal voltage and the coupled eigenfrequency. The highest voltage, generated by the device during the experiments, U_{max_EXP} = 1.41 V is shown to be about 1.4% higher than the FE obtained maximum voltage value U_{max_FEA}

= 1.39 V, both achieved at a coupled eigenfrequency f_{1_coup} ~ 544 Hz. Regardless of the reasonably close match, certain discrepancies can be noticed in the overall shape of the response curves, more expressed as the excitation frequency moves away from the coupled eigenfrequency value. Such a divergence could occur due to slight experimental excitation control errors or inaccuracies in clamping the fixed end of the PEH, i.e., because of a small difference in cantilever length that can have a considerable influence on the responses of a bimorph EH device. Furthermore, the numerical results can be influenced, to some extent, by errors in the damping ratio evaluation, translated into the Rayleigh damping coefficients, as well as various limitations of the employed analysis software - ANSYS® in this case, in accurately modelling the effects of electromechanical coupling [220].

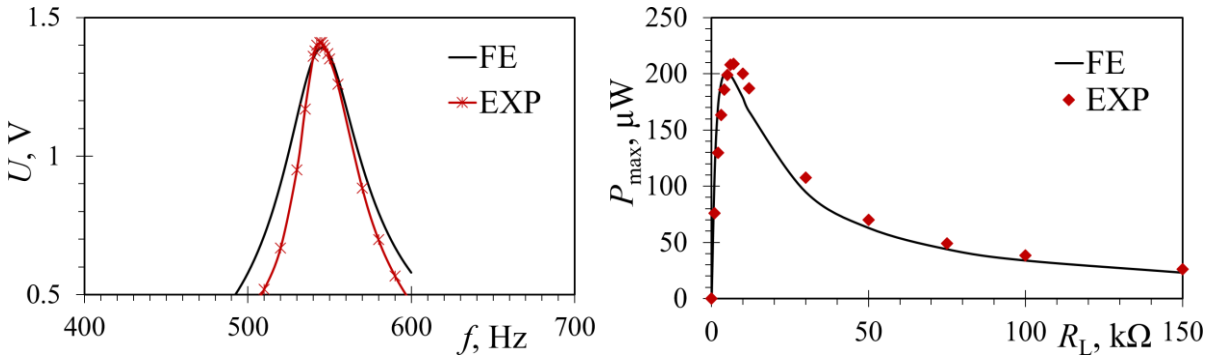

(a) (b)

Figure 6.3. Experimental vs. FE voltage output values a) and experimental versus FE power outputs in relation to R_L b) for a harmonically excited rectangular PEH.

In order to study the PEH behaviour over a wider range of load resistance values, additional harmonic analyses are conducted with a varying R_L value ranging from 1 to 150 kΩ. The respective maximum power values are displayed in Figure 6.3b vs. the load resistance values. Again, a relatively close match can be observed between the experimental and the numerical results, i.e., there is a mere ~ 3.5% difference in maximum power values. It can be noticed, however, that the peak of the experimentally assessed power curve slightly shifts towards a higher load resistance value of R_L = 6 kΩ. These slight discrepancies could possibly be caused by inaccuracies innate to a non-ideal experimental setup, e.g. clamping and excitation control, as well as by additional resistances present in the experimental system, neglected in the FE model. Subsequently, the validation of the FUC modelling approach is conducted by assessing the transient response of the studied PEH by plucking the free end and letting it oscillate at its eigenfrequency. As it was the case with the harmonic and modal analyses, the boundary conditions (clamping and coupling) in the FE models are constant in this instance too, while the load

is applied to the PEH free end as a displacement δ_z along the *z* axis (see Section 4). For validation purposes, the free end displacement is set as δ_z = 0.6 mm, to avoid overstressing the bimorph due to considerable adjustments required to adequately tune the setup. The voltage responses for the studied rectangular PEH, obtained both experimentally and via FE analysis at the optimal load resistance of R_L = 5 kΩ, are graphically displayed in Figure 6.4a, where the numerical data exhibits a close match with the experiment. The matching of the results is especially pronounced in the initial five cycles, where the maximal experimentally measured peak-to-peak voltage is $U_{p\text{-}p\_EXP}$ = 20.1 V, differing by ~ 5% from the numerical results of $U_{p\text{-}p\_FEA}$ = 21.26 V. These initial cycles are of particular significance since, due to the highest voltage levels, they result in the majority of the power generated by the device. When the subsequent cycles are considered, the difference in voltage ranges from ~ 1% to ~ 9%, which could be mitigated by tuning the damping coefficients via the damping ratio, with a pronounced negative influence on the foremost section of the response, increasing the mismatch of the results.

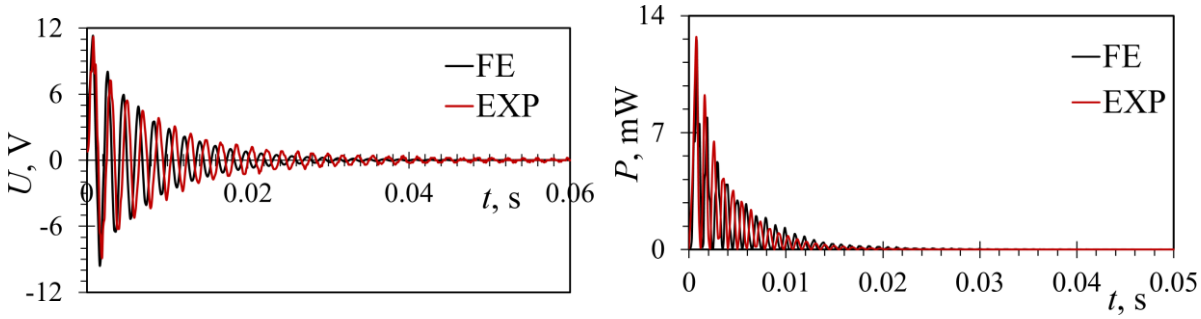

(a) (b)

Figure 6.4. Experimental vs. transient FE FUC voltage responses (a), and respective power outputs at an optimal load resistance (b) for a plucked rectangular bimorph PEH.

The experimental and numerical power outputs of the FUC excited rectangular PEH, generated at its optimal load resistance, calculated from the respective maximal voltage values, are shown in Figure 6.4b, where it can be observed that the numerical data, P_{max_FEA} = 12.53 mW, matches closely the experiments P_{max_EXP} = 12.42 mW, exhibiting a minor difference of 0.88%. The average power is, in turn, calculated from the average voltage values over a 0.05 s time interval, resulting in ~ 3% difference between the numerical (P_{av_FEA} = 0.454 mW) and the experimental (P_{av_EXP} = 0.468 mW) values. The above presented results show, therefore, a close match between the numerical and the experimental results for both considered methods of excitation.

6.2. Experimental measurements of optimized PEH performances

The optimized devices designed using the combined approach comprising the DoE methodology and the experimentally validated modelling described above, are then manufactured by cutting the optimal shapes from the commercially available rectangular devices, as shown in Figure 6.5a [153]. A precision waterjet device is used for this purpose at the RWS Waterjet Service GmbH in Germany [170]. It is important to note here that the individual segments of the segmented shapes are manufactured separately to facilitate their individual experimental analysis. These optimized shapes, shown in Figures 6.5b to 6.5f, are then experimentally tested using the two previously described setups, and their responses in terms of voltage and power outputs, are critically analysed.

(a) (b) (c) (d) (e) (f)

Figure 6.5. Rectangular (a) and optimized PEH shapes manufactured using waterjet technology: inverted trapezoidal (b), trapezoidal (c), inverted trapezoidal with stress concentrators (d), trapezoidal with stress concentrators (e) and notched (f).

6.2.1. FUC excitation measurements

The optimized devices are subjected to free end excitation via plucking, using the experimental setup described in Section 4. Initially, the first uncoupled eigenfrequencies $f_{1\_mech\_EXP}$ of each individual shape are obtained via tip excitation, and the thus assessed results are compared to the FE data ($f_{1\_mech\_FEA}$), displaying a good match, as it can be observed in Table 6.2. The measured eigenfrequency values of the optimized shapes range from $f_{1\_mech\_EXP}$ = 324.7 Hz (σ_{sd} = ± 0.46 Hz) for the inverted trapezoidal shape up to 934.1 Hz 1 (σ_{sd} = ± 1.63 Hz) in the case of the trapezoidal one. The closest match between the experimental and FE data (< 0.1% difference) can be seen in both inverted trapezoidal shapes, i.e., the shapes with and without stress concentrators, while the most pronounced difference of ~ 4% can be observed in the case of the trapezoidal shape with stress concentrators. The latter could be attributed to clamping

inaccuracies due to the small size and the geometrical complexity of this particular harvester, as well as to its very narrow tip where the laser beam of the vibrometer is aimed at.

Table 6.2. Optimized PEHs uncoupled eigenfrequency values.

	$f_{1\_mech\_FEA}$, Hz	$f_{1\_mech\_EXP}$, Hz	Diff.
Trapezoidal	930.2	934.1 (σ_{sd} = ± 1.63)	0.44%
Inverted	324.5	324.7 (σ_{sd} = ± 0.46)	0.065%
Notched	374.1	374.6 (σ_{sd} = ± 0.79)	0.14%
Trapezoidal with stress concentrators	762.5	793.7 (σ_{sd} = ± 2.98)	4.09%
Inverted with stress concentrators	333.5	333.6 (σ_{sd} = ± 0.6)	0.033%

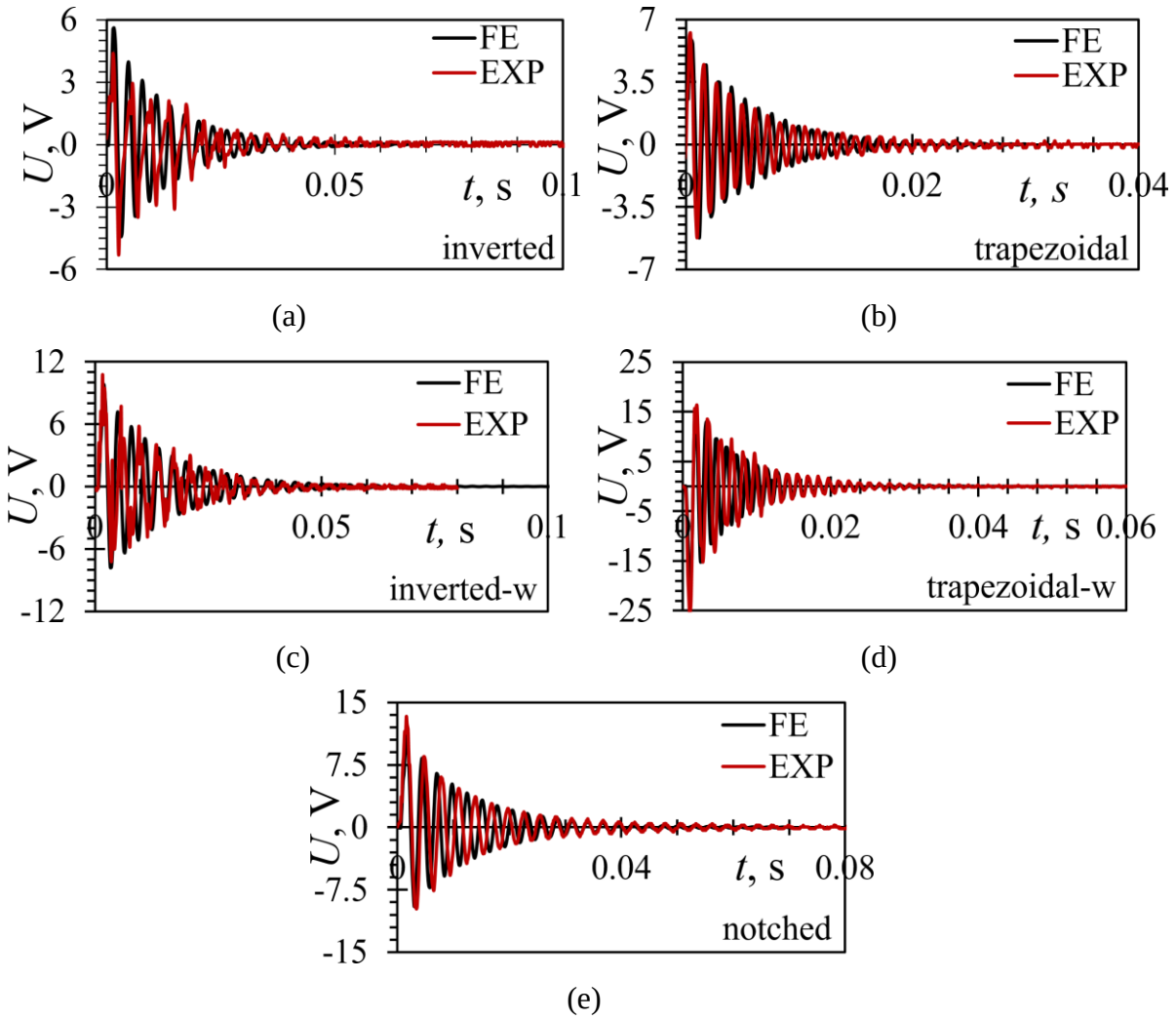

Figure 6.6. Comparison of experimental and transient FE responses of the PEHs excited by plucking for: an inverted trapezoidal (a), a trapezoidal (b), an inverted trapezoidal with stress concentrators (c), a trapezoidal with stress concentrators (d) as well as a notched (e) bimorph PEH.

The straight-edged trapezoidal and the notched shape, in turn, both show differences between the numerical and the experimental data of less than 0.5%. The studied devices are then connected to a variable resistance box set to their respective optimal resistance values, the voltage responses for each of the individual PEHs are assessed by plucking their free ends, and the resulting power outputs are calculated. The thus attained responses are graphically represented in Figure 6.6., in comparison with the numerical responses obtained via the transient FE analyses. The initial deflection of the free end, resulting in the excitation of the PEHs, is achieved by plucking the cantilevers with a rectangular 3D printed plectrum attached to a DC motor, while its rotating speed is kept constant. This deflection is measured via the previously describe laser vibrometer, to adhere to the limitations established in Section 5 due to piezoelectric material fatigue strength considerations.

The voltage output of the inverted trapezoidal segment, generated by an initial deflection of δ_z = 0.27 mm at an optimal load resistance value of R_{L_opt} = 13 kΩ, is displayed in Figure 6.6a. The maximum peak-to-peak voltage, measured in in the experiment is $U_{p\text{-}p\_EXP}$ = 9.66 V, differing from the respective numerical FE result $U_{p\text{-}p\_FEA}$ = 10.04 V, by ~ 3.8%. Both the numerical and experimental responses display an oscillation period of T ~ 0.06 s.

Figure 6.6b shows the voltage responses for the trapezoidal segment. The displayed response is achieved with a 0.2 mm initial free end deflection and at an optimal load resistance of R_{L_opt} = 7 kΩ. The highest measured peak-to-peak voltage is $U_{p\text{-}p\_EXP}$ = 11.46 V, which, when compared to the numerical voltage $U_{p\text{-}p\_FEA}$ = 11.07 V, shows a difference of ~ 3.5%. Due to a more rigid design, and thus an elevated first eigenfrequency, the oscillation period of T ~ 0.03 s is shorter than in the previous case.

The voltage responses for the inverted trapezoidal segment with added stress concentrators, resulting from an initial free end deflection of δ_z = 0.48 mm, measured at the optimal load resistance of R_{L_opt} = 12 kΩ, is displayed in Figure 6.6c. A difference of ~ 1.6% can be observed between the maximal peak-to-peak voltage measured in the experiment, $U_{p\text{-}p\_EXP}$ = 17.9 V and the numerically obtained results $U_{p\text{-}p\_FEA}$ = 17.61 V. The oscillation period in both cases is T ~ 0.06 s.

The voltage generated by the trapezoidal segment with added stress concentrators, excited by an initial tip deflection of δ_z = 0.38 mm, at an optimal load resistance of R_{L_opt} = 13 kΩ, is shown in Figure 6.6d. A maximal peak-to-peak voltage $U_{p\text{-}p\_EXP}$ = 41.62 V is measured, which, in comparison with the numerical response, displays a difference of ~ 1.5%. As in the case of the straight-edged segments, the oscillation period is significantly lower, i.e. T ~ 0.03 s.

Finally, Figure 6.6e shows the response for the notched PEH shape, generated by an initial

free end deflection of δ_z = 0.47 mm at the optimal load resistance of R_{L_opt} = 7 kΩ. A ~ 7.5% difference is noticed between the experimentally assessed maximal peak-to-peak voltage $U_{p\text{-}p\_EXP}$ = 23.1 V and the respective results obtained via the FE transient analysis, $U_{p\text{-}p\_FEA}$ = 21.4 V. The oscillation period is similar in both cases, i.e. T ~ 0.08 s.

In all the above reported cases, a close match between the experimental and the numerical data can be observed, showing, once more, the viability of using the FEA approach. Table 6.3. lists, in turn, the above reported maximal peak-to-peak voltage values along with the average voltages, calculated over the oscillation periods of the respective devices. Furthermore, the average P_{ave}, the maximal P_{max}, and the specific powers P_s normalized over the surface area of the respective PEH, are also shown in Table 6.3., providing a more detailed insight in the experimental results achieved under the above reported conditions of initial tip deflection and optimal load resistance values. Since the initial tip deflection, significantly affecting the PEH response, differs in the reported experiments, these results cannot be reliably compared. For that purpose, a suitable figure of merit will be introduced in the following subsections in terms of voltage outputs normalized over the initial deflection value, thus facilitating the comparison.

Table 6.3. Experimentally obtained results for optimized and rectangular

	$U_{max\_p\text{-}p}$, V	P_{av}, µW	P_{max}, mW	P_s, µW/mm^2
Trapezoidal	11.46	71	2.79	37
Inverted	9.66	25	1.1	6
Notched	23.12	411	12.66	42
Trapezoidal with stress concentrators	41.62	442	31.95	43
Inverted with stress concentrators	17.9	148	4.74	24
Rectangular	20.1	468	12.42	36

6.2.2. Optimized PEH power outputs

The FUC experimental setup employed in in this work enables, as mention above, deflecting the PEH free end by the initial displacement δ_z via a constantly rotating 3D printed plectrum, thus achieving the plucking effect. The excited device is then let to oscillate at its eigenfrequency. Since the value of the initial deflection δ_z strongly depends on the properties, i.e., the shape and the stiffness of the individual PEH, as well as those of the plectrum, it cannot practically be precisely predicted and controlled. What is more, due to electromechanical coupling the properties of the PEH are affected by the electrical load itself, while the mechanical properties of the 3D printed plectrum are found to be uneven as a result of the printing orientation

as well as the filament layer delamination effects [12, 35, 62, 92]. This, in turn, results in different δ_z values for each experimentally studied PEH shape (cf. Table 6.3.), thus making a comprehensive comparison difficult. With this in mind, a comparison in terms of the voltage or power outputs normalized by the initial deflection δ_z of the respective PEH, is introduced. The thus normalized peak-to-peak voltages $U_{n\_max\_p\text{-}p}$, V/mm and powers P_{n_xx}, mW/mm for the optimized shapes, as well as for the reference rectangular one, are reported in Table 6.4.

Table 6.4. Experimentally obtained results normalized by the respective δ_z values.

	$U_{n\_max\_p\text{-}p}$, V/mm	P_{n_av}, mW/mm	P_{n_max}, mW/mm	$P_{n\_s\_max}$, μW/mm²/mm
Trapezoidal	45.83	1.13	44.57	590
Inverted	36.46	0.36	15.43	80
Notched	49.18	2.087	57.33	188
Trapezoidal with stress concentrators	52.03	0.69	49.92	670
Inverted with stress concentrators	37.3	0.641	20.57	106
Rectangular	33.4	2.49	34.8	101

By normalizing the output voltages, it can thus be observed that, when subject to plucking excitation and compared to the rectangular shape, all the optimized shapes exhibit significantly improved performances in terms of the peak-to-peak voltages. As it is graphically represented in Figure 6.7a, the highest voltage is then generated by using the trapezoidal segment with stress concentrators, $U_{n\_max\_p\text{-}p}$ = 52.03 V/mm, while the lowest, close to the values generated by the rectangular shape $U_{n\_max\_p\text{-}p}$ = 33.4 V/mm, is achieved by the inverted trapezoidal segment ($U_{n\_max\_p\text{-}p}$ = 36.46 V/mm). What is more, an increase in output voltage can be observed in both PEH segments with added stress concentrators in comparison with their straight-edged counterparts, confirming thus the assumptions made in the initial studies (see Section 5). In terms of the average power, measured over the oscillation period of the individual devices, the rectangular shape displays the highest output P_{n_av} = 2.49 mW/mm, with the optimized shapes showing lower but comparable values, especially when the outputs of all the segments comprising the segmented PEH are summed up. When these values are normalized over the surface areas of the respective devices, as shown in Figure 6.7b, both trapezoidal segments show significantly higher specific normalized average power values compared to the rectangular shape. The values generated by the notched PEH are somewhat (~ 5%) lower but comparable to those of the conventional rectangular device. The specific normalized average power generated by the inverted trapezoidal segments, both with and without added stress concentrators, is lower than that of the rectangular PEH, but, as it was previously mentioned, it should be perceived as an addition

to the trapezoidal segments, constituting the overall segmented device. The maximum power outputs, obtained from the normalized voltages divided by the surface area of the respective shapes, are displayed in Figure 6.7c. A significant increase in performances can be observed in case of both trapezoidal segments, i.e., $P_{n\_s\_max}$ = 590 μW/mm^2/mm for the straight-edged shape and $P_{n\_s\_max}$ = 670 μW/mm^2/mm for the one with added stress concentrators, when compared with the output of the rectangular PEH ($P_{n\_s\_max}$ = 101 μW/mm^2/mm). The notched shape shows a less pronounced but still noticeable gain in performances ($P_{n\_s\_max}$ = 188 μW/mm^2/mm) in comparison with the rectangular device. The specific normalized maximum power output comparable to that of the rectangular PEH is, in turn, achieved by both inverted trapezoidal shapes. The inverted segment with straight edges generates then a somewhat lower output ($P_{n\_s\_max}$ = 80 μW/mm^2/mm), while its counterpart with added stress concentrators shows slightly better performances ($P_{n\_s\_max}$ = 106 μW/mm^2/mm).

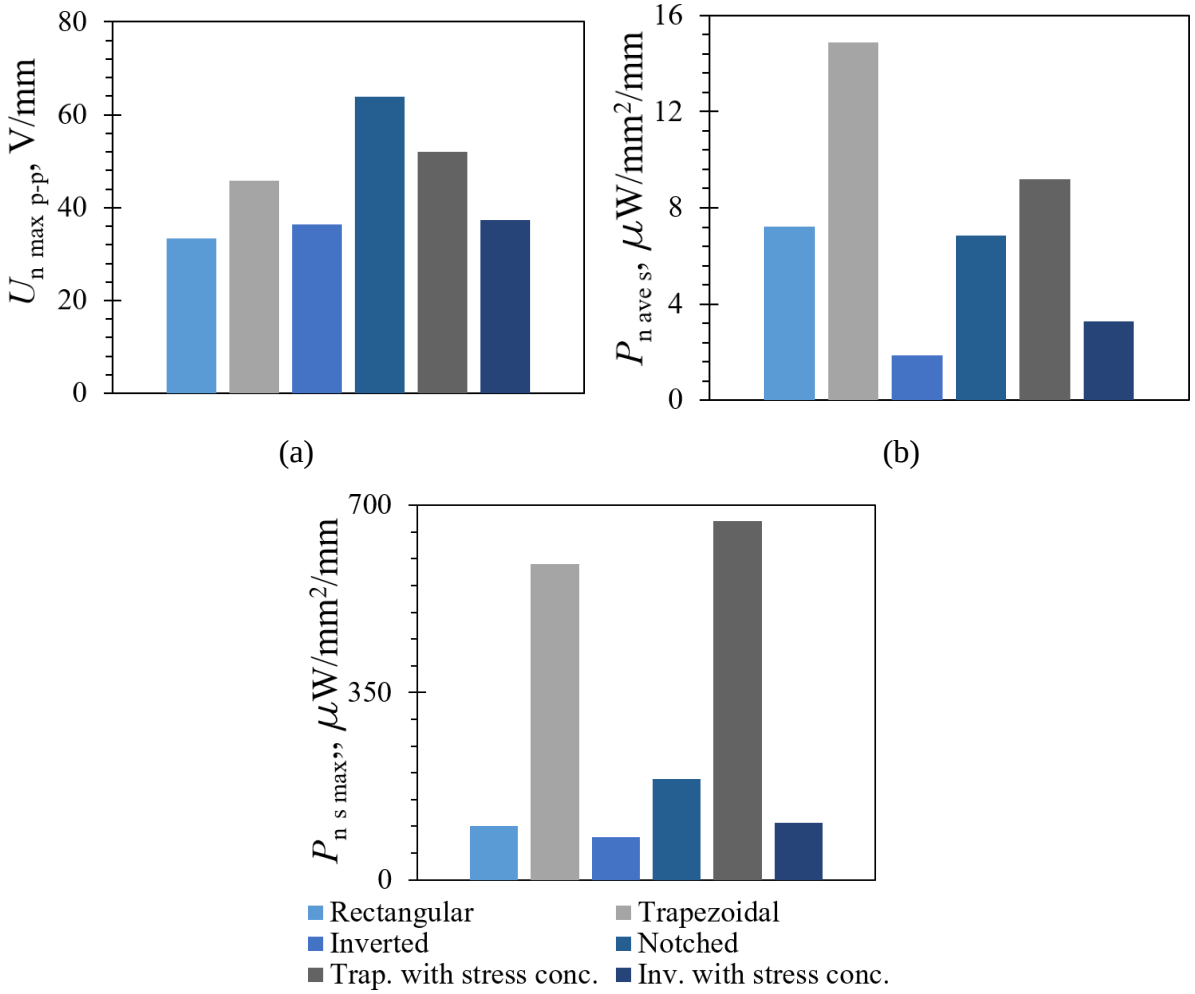

Figure 6.7. Normalized maximal voltages (a), as well as the respectively calculated specific average (b) and specific maximal (c) power outputs for the considered bimorph PEH shapes.

These values should, as it was repeatedly pointed out, seen as an addition to the power outputs of the respective trapezoidal segments. It should also be noted here that, as with the maximal voltage values, a measurable gain in performances in terms of normalized specific maximal powers, can be achieved if the stress concentrators are added to an optimally segmented piezoelectric EH device. The maximal power values reported in Table 6.3. are the result of an initial tip deflection smaller than the maximum allowable values determined in Section 5 (see Figure 5.11.), and therefore do not represent the best performances achievable by the suggested optimized devices when excited by the respective maximal allowable deflection δ_{z_max} (corresponding to the deflection that produces a stress close to the fatigue limit). The maximal and average powers generated during the reported oscillation period, achievable by the suggested devices when excited at the respective δ_{z_max} deflections, are therefore assessed for each individual shape based on the normalized power values, and reported in Table 6.5.

Table 6.5. Power outputs achievable by the optimized PEHs at the maximal displacements.

	$P_{max\_\delta z\_max}$, mW	$P_{av\_\delta z\_max}$, mW
Trapezoidal	62.4	1.58
Inverted	9.26	0.22
Notched	28.7	1.04
Trapezoidal with stress concentrators	49.9	0.69
Inverted with stress concentrators	12.3	0.38
Rectangular	34.8	2.49

When the maximal achievable power outputs for the straight-edged segments that are part of a segmented device are summed up, the maximum power output, achievable by such a device observed as a whole, is $P_{max\_\delta z\_max}$ = 134.06 mW. The average power, generated over the oscillation periods reported for both segment types is, in turn, $P_{av\_\delta z\_max}$ = 3.38 mW. Both values represent a significant improvement in performances, when compared to the conventional rectangular device excited at its maximal allowable tip deflection. When the segments with added stress concentrators are considered, the overall maximum power output $P_{max\_\delta z\_max}$ = 112.1 mW, while being lower than the variant without stress concentrators, clearly outperforms the rectangular shape. In terms of the average power, however, the rectangular PEH displays a better performance than the segmented device with stress concentrators, i.e., $P_{av\_\delta z\_max}$ = 2.49 mW vs. $P_{av\_\delta z\_max}$ = 1.76 mW. This could be attributed to the limited allowable initial tip deflection caused by the increased stress levels around the added stress concentrators. Similarly, excessive stresses around the notch could be the reason behind the relatively low maximal achievable performances of the notched device, both in terms of the maximal and the average powers,

$P_{max\_\delta z\_max}$ = 28.7 mW and $P_{av\_\delta z\_max}$ = 1.04 mW, respectively. The results pertaining to the segmented shapes with added stress concentrators, as well as those for the notched PEH, show thus that a compromise should be made between the benefits of increased voltage outputs and the increased stress levels, i.e. the reduced lifespan of a PEH, depending on the design requirements of a particular device and its application.

6.3. Critical analysis and assessment of the results

The results of the experimental measurements performed by using the described experimental setup and compared to the numerical data obtained from the experimentally validated FE models, clearly show the performance improvements, both in terms of the voltages and powers, up to 5 times, achieved via the optimization of the piezoelectric EH devices excited by plucking. Furthermore, the viability of the herein utilized DoE-FE approach in optimized PEH design is also confirmed. When a single trapezoidal segment, as a part of the segmented device, is compared to the reference rectangular shape, a 484% increase in specific maximal power outputs, as well as a 28% increase in the absolute maximal power, is observed. The specific power output of the optimized notched device is, in turn, found to be 86% (~ 65% in case of the maximal power) higher than that generated by the conventional rectangular bimorph. Further improvements are obtained by introducing stress concentrators along the edges of the segments, in comparison to the respective straight-edged shapes. This is exhibited as an increase in specific power output of 14% and 12% for the maximal power in case of the inverted trapezoidal shape. In case of the trapezoidal segment, the addition of stress concentrators results in a 32.5% increase in the specific power and a 33.3% increase in terms of the maximal power. Compared to the rectangular shape, the trapezoidal segment with added stress concentrators displays, in turn, a 563% increase in specific power and a ~ 45% gain in the maximal power output. A relatively low specific power output is observed in the case of the inverted trapezoidal segments. While both variation show performances comparable to the rectangular PEH, the inverted segment with added stress concentrators slightly outperforms it. Such relatively low performance can be attributed to the narrow cross-section of these particular shapes near the clamped end, which limits the allowable initial free end deflection. The power generated by the inverted segments, should, however, be viewed as a portion of the overall power output generated by the segmented device, and are to be added to the outputs of the two trapezoidal segments.

When the absolute power values potentially achievable by exciting the optimized PEHs with

the maximal allowable free end deflections are considered, a relatively wide range of results is obtained, i.e., a substantial output of $P_{max\_\delta z\_max}$ = 134.06 mW is observed for the overall straight-edged segmented PEH, with the inverted trapezoidal segment, by itself, producing only $P_{max\_\delta z\_max}$ = 9.26 mW. The highest output in terms of the average power, attained within the oscillation periods of the individual shapes, is generated by the complete segmented device without stress concentrators, i.e., $P_{ave\_\delta z\_max}$ = 3.38 mW. As in the previous case, the lowest average power is generated by the inverted straight-edged trapezoidal segment ($P_{ave\_\delta z\_max}$ = 0.22 mW). When compared to the output generated by the conventional rectangular PEH with the same overall surface area ($P_{max\_\delta z\_max}$ = 34.8 mW and $P_{ave\_\delta z\_max}$ = 2.49 mW), the segmented device with straight edges displays again significantly improved performances.

It is important to note that the PEH performance results obtained by excitation via equal tip deflections applied to all the studied shapes, without any consideration of fatigue strength limitations, i.e., as it is done in the majority of the available literature as well as in the initial studies, show a substantial difference in comparison to those where such considerations are taken into account. The difference is observed both in the overall trends as well as in the obtained performances. If the strength is not considered, and the same deflection is used for all PEHs, the output of the inverted trapezoidal shape is then significantly higher than that of the trapezoidal segment, while, if the initial deflection is limited to reduce the stress levels, the trapezoidal shape clearly outperforms the inverted one. With this in mind, whenever PEH performances are presented in literature, without any considerations given to fatigue strength, the reports should therefore be viewed with a due caution and foresight.

When the above reported power outputs are compared to the power levels required by the miniaturized wearable medical device, presented in Section 3, it can be noted that, in terms of maximum power, i.e. 134.06 mW, the segmented PEH without stress concentrators, excited by the largest allowable tip displacement, is able to supply enough power needed by the proposed device, i.e. ~ 115 mW, without considering the duty cycles of the respective components. When, on the other hand, the duty cycles are taken into account, the reduced power requirements of the wearable device, i.e. ~ 5 mW, can easily be achieved and exceeded by a single segmented PEH. What is more, if two straight-edged segmented PEHs are used alongside each other, their combined output in terms of average power, i.e. ~ 6.8 mW is more than enough to power the proposed wearable device.

The process of experimentally validating the FE models used in this work was thoroughly described in this section. The layers of a commercially available PEH were measured and a corrected 3D model was made. By comparing the modal, harmonic and transient FE responses

to the respective experimentally assessed values, the FE models were validated, exhibiting a very good match. The process of manufacturing the optimized shapes was shortly touched upon, and the modal responses were assessed for each one of them. By utilizing the FUC experimental setup, the optimized shapes were excited by a tip deflection limited due to strength considerations, and the voltage responses were obtained, matching the respective numerical ones. The performance figures were then assessed for all the optimized shapes in terms of the maximal and specific powers and the outputs were normalized by the tip deflections to facilitate their comparison. The maximum potentially achievable performances by exciting the PEHs by the larges allowable tip deflections were also determined for each of the considered shapes, and the overall results were critically analysed. It was shown that a ~ 500% increase in performance can be achieved by segmenting a rectangular PEH into optimized trapezoidal and inverted segments and subjecting it to plucking excitation, while considering the fatigue strength of the piezoelectric layers. Moreover, it was also demonstrated that such a device, i.e. optimally segmented plucked PEH, is capable of providing more than enough power, i.e. 134.06 mW, for the operation of a wearable medical device aimed for autonomous health monitoring, i.e. ~ 5 mW, while two segmented PEHs used in tandem, are able to exceed that requirement even in terms of average power, i.e. ~ 6.8 mW.

The next section will provide a short outline of the additive manufacturing technologies, particularly those used within this work. An extensive experimental study and optimization of the 3D printed plectra properties will be conducted, providing valuable insights for the design of the factual FUC mechanisms and, finally, a comprehensive description of the development of a watch-like wearable device based on the optimized segmented PEHs excited by plucking via a FUC mechanism will be presented.

7. CONCRETIZATION OF A WEARABLE FUC EXCITATION MECHANISM

A FUC mechanism suitable for wearable applications needs to be developed next, aimed at deflecting the free end of the optimized segmented device, thus inducing the needed excitation. Such a mechanism should adhere to the principles of simplicity and reliability, while taking the least possible space in the limited volume of a wearable device. In this frame it is planned to manufacture the device prototype by using additive technologies, i.e., the fused deposition modelling (FDM) modality. A short outline of the FDM technology is thus also provided in this section. An extensive experimental study of 3D printed plectra used for plucking excitation is conducted in this section, by employing the DoE methodology. The effects of several design parameters, i.e., the plectrum material, the plectrum length l, mm the respective area moment of inertia I_x, mm^4, as well as the rotating speed n, min^{-1}, are studied and their optimal combination is determined.

7.1. Additive manufacturing

Additive manufacturing (AM), popularly referred to as 3D printing, is defined, according to American Society for Testing and Materials (ASTM) as a process of joining materials to make objects from 3D model data, usually layer upon layer, as opposed to subtractive manufacturing methodologies. Given its versatility, as well as its applicability in rapid prototyping to produce complex parts, adaptable to verifying various design variants, AM will be used in the herein considered framework to produce a variety of plectra intended for the subsequently presented experimental study, as well as a concept of a wearable watch-like device, aimed for medical applications. As it can be seen in Figure 7.1., the process begins with a 3D model of the desired part. The 3D geometry is then converted to an intermediary neutral format, used to translate data between different CAD systems [36], and processed by introducing construction elements, e.g. supports, as well as parameters characteristic for the manufacturing process and the used 3D printing machine itself. The 3D geometry is then divided into 2D layers and a toolpath for the 3D printer is generated [65]. The majority of commercial systems is still based on melting a polymer material using a heated extruder, thus allowing it to flow through a delivery system, i.e., an extrusion based systems. The most common of such processes is the fused deposition modelling (FDM) method, extruding the molten material through one or multiple nozzles [65].

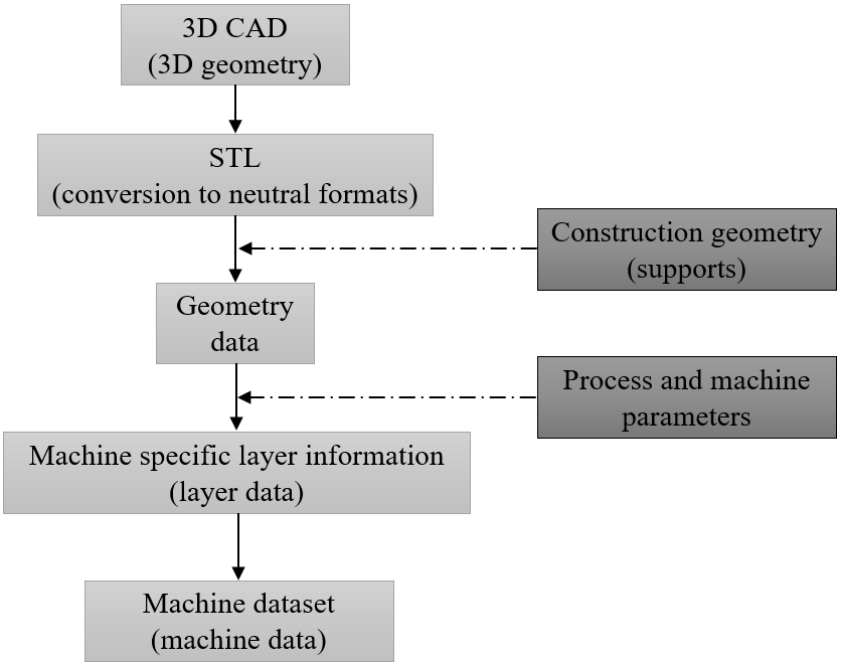

Figure 7.1. Simplified representation of a generalized data path for AM [65].

The material is pushed therein through the nozzle in filament form, i.e., that of a prefabricated wire-shaped thermoplastics [46, 48]. The schematic representation of a typical FDM extruder head is shown in Figure 7.2. The filament is pushed via the feed mechanism into a heated chamber, i.e., a liquefier, where it is melted. The molten polymer is then pushed through the moveable nozzle, controlled by the software that transposes the geometry of the manufactured part into the coordinates of the respective motion, thus forming a material layer, which solidifies due to heat dissipation. The extruder assembly can be positioned along two horizontal and one vertical axis, using conventional precision positioning components, e.g. stepper motors, belt drives, leadscrews and linear guide rails [65]. FDM technology allows the utilization of a wide range of materials, e.g. polyamide (PA), polycarbonate (PC), acrylonitrile butadiene styrene (ABS) and polylactic acid (PLA), and thus the manufacturing of parts with different mechanical properties aimed for a variety of applications. According to the data provided by manufacturers, no irritants or toxic vapours harmful to humans are present during the process, which makes office operation possible [65]. What is more, the strength of the structures manufactured using FDM is significantly higher than that of other polymer-based AM technologies [67]. On the other hand, one of the major limitations of FDM is the build speed, limited by the inertia of the extruder heads along with issues in terms of accuracy and material density. What is more, the nozzles used in all FDM systems are circular, making it difficult to achieve sharp edges and corners, both external and internal. Also, the use of belt drives instead of leadscrews in lower cost systems, strongly affects the accuracy of the 3D printers, due to the flexing occurring in

the belts [67].

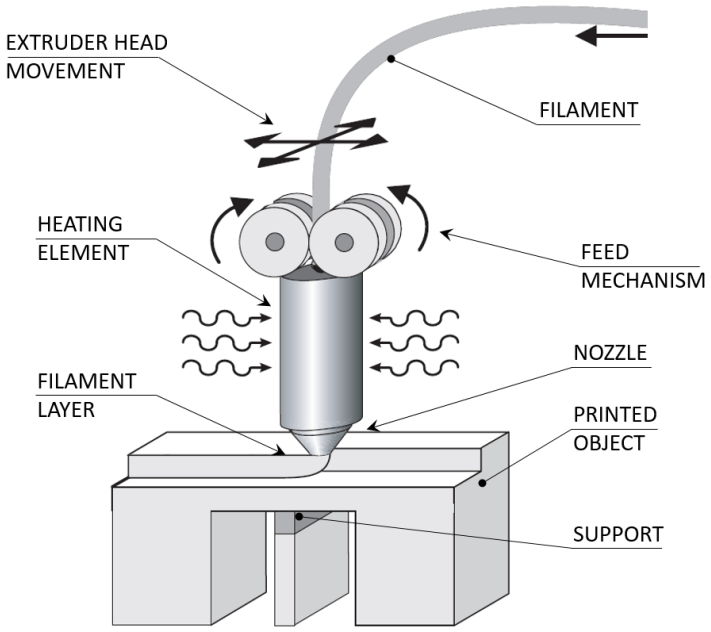

Figure 7.2. Schematic representation of an FDM extruder head [65].

Various patterns, e.g. hatch and honeycomb, can be employed to fill the interior of the part, reducing the amount of the used material and increasing the build speed, especially when the mechanical strength of the manufactured part is not crucial [67].

Moreover, different orientations of the parts during the manufacturing process result in different mechanical properties. For example, the tensile strength of a part will be higher if the direction of the force acting on it is parallel to the direction in which the layers are deposited, while a significant decrease in strength occurs if the force cuts in a perpendicular direction [12, 35, 48, 62, 92]. Despite the relatively quick solidification of the deposited material, supports, i.e., automatically generated segments are required to produce parts with projecting sections, as well as for creating the base of the printed model. Supports are either made from the same material as the model, or of a more brittle material, i.e., break-away or soluble supports [65]. Break-away supports (BASS), commonly used along with PC and PLA materials, allow an easy removal without the need for machining, while soluble supports, also known as water works supports (WW), used together with the ABS material, enable their fairly quick hands-free removal by dissolution in a mild caustic solution, such as e.g. sodium hydroxide (NaOH) [46, 201]. Two different FDM machines, both equipped with two separate extrudes, are used in this work, namely, the Stratasys® Fortus 250mc [189], employed for creating the prototype of the wearable device, and the Flashforge® Creator 3 [61], utilized for producing the plectra studied in the following subsection. The Stratasys® Fortus 250mc, shown in Figure 7.3a, is an industrial grade FDM 3D printer, able to simultaneously extrude both the build and the support material

inside a 203 x 203 x 305 mm heated work space, and it is limited to a single build material type - ABS. The manufactured part can be created within an accuracy of ± 0.241 mm, with three available layer thicknesses: fine = 0.178 mm, standard = 0.254 mm, and draft = 0.33 mm [202-203]. The Flashforge® Creator 3 is an FDM system aimed at professional as well as industrial applications, equipped with two 0.4 mm independent extruders (Figure 7.3b). The machine is able to utilize numerous build materials such as PLA, ABS and polyethylene terephthalate (PET), as well as fibre-reinforced polymers. The available working space is 300 x 250 x 200 mm, and the removable platform can be heated up to 120°C. The parts can be printed within an accuracy of ± 0.2 mm [171, 204]. The benefits of this flexible system are utilized in this work to create 3D printed plectra of different geometrical properties, made from four distinct materials, required for the extensive experimental study reported in the following subsection.

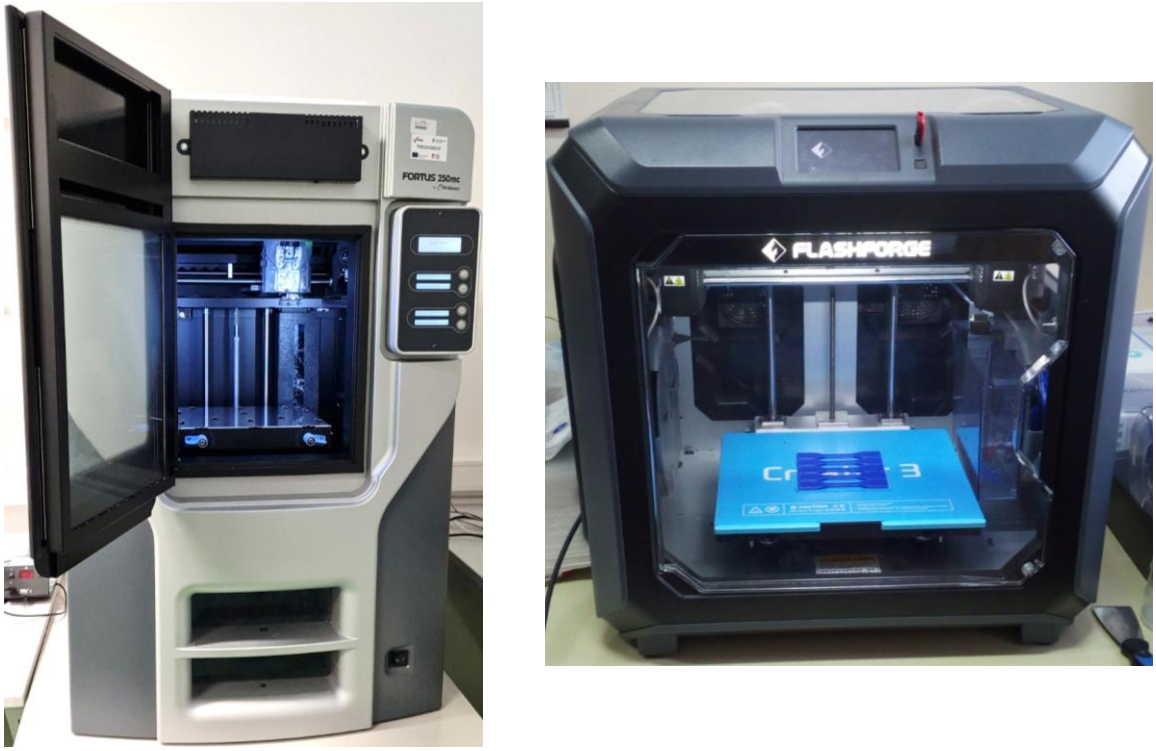

(a) (b)

Figure 7.3. 3D printers utilized in this work: Stratasys® Fortus 250mc [199] (a) and Flashforge® Creator 3 [200] (b).

Recently, with the improvements in laser technology, machine accuracy, speed, and cost, 3D printing machines able to use metals for additive manufacturing made a wider appearance on the market. The majority of such available machines utilize the point-wise method and metal powders as the input material. The metal powders are spread via an approach similar to the selective laser sintering (SLS) process, and are then melted by a high energy beam, i.e., a high energy laser or a beam of electrons. The powdered metal can also be delivered via a nozzle and

then melted, where the material coalesces with the laser and the substrate, enabling the use of this approach for repairing expensive metal parts, e.g. moulding tools and turbine blades [67].

7.2. Plectrum analysis and optimization

The geometric and mechanical properties of plectra, utilized for inducing the plucking excitation of the optimized PEHs developed above, are shown to significantly affect their responses [96]. This is particularly pronounced when the plectra are produced using AM technologies, due to their innate issues, e.g. variations in mechanical properties due to part orientation during the manufacturing process [13, 82, 117], porosity, distortion and layer delamination [65, 104]. To better understand these effects, and thus improve the design of the FUC mechanism, a thorough experimental study, based on the DoE methodology, is conducted, considering the geometry as well as the materials of the 3D printed plectra. Initially, three basic plectrum shapes, i.e., rectangular, elliptical and triangular, shown in Figure 7.4a, are taken into account. The studied plectra are produced as parts of a six-plectrum rotor, displayed in Figure 7.4b, which can be attached to a DC motor, enabling thus their controlled rotation and the periodical plucking of the PEHs. As the geometry of the plectrum is mostly affected by its stiffness, the range of the considered dimensions is set in a manner which results in a continuous and uniform range of plectrum stiffness values. Due to the relatively low accuracy of the herein used AM machines in terms of the final product dimensions, the thickness of all the studied plectra is limited to t = 0.7 mm, and it is kept constant throughout the study. The variation of the area moment of inertia I_x, mm^4, is thus achieved by altering the width of the plectrum, a dimension which is less affected by the accuracy of the 3D printing machine.

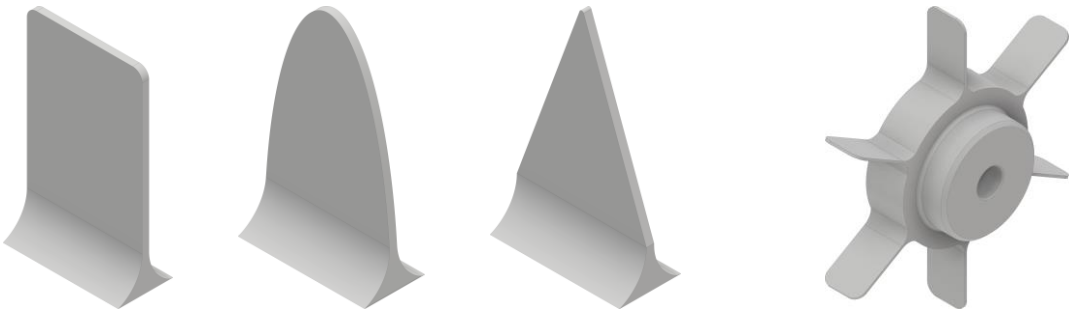

(a) (b)

Figure 7.4. Different shapes of the studied plectra (a), and the six-plectra rotor (b) [120]

The initial experiments aimed at studying the aforementioned plectrum shapes, are conducted by using the impact excitation experimental setup described in Section 4, i.e., by plucking the free end of a commercially available rectangular PEH [153] and assessing its resulting

voltage responses. In this case the setup comprises, as it is denoted in Figure 7.5., a DC motor (1) controlled via a laboratory voltage supply, the studied 3D printed plectrum (2), the commercially available rectangular PEH [153] (3), as well as the 3D printed clamping base (4).

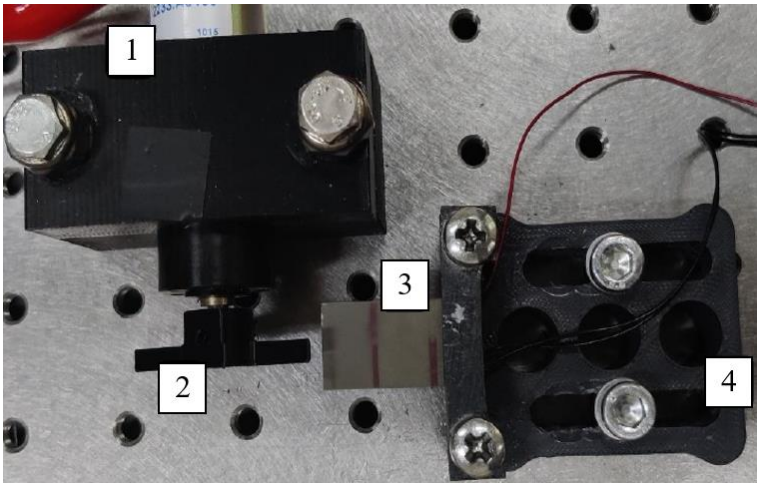

Figure 7.5. Experimental setup for generating plucking excitation [120].

The actual geometry of the triangular and elliptical 3D printed plectra is, however, found to be noticeably different from the respective computer-aided design (CAD) models, strongly affecting the stiffness of the structures. Such discrepancies in stiffness values cause, in turn, significant issues in terms of the resultant repeatability in the responses of the PEH. To mitigate these issues, only the rectangular plectrum shape, i.e., the one most accurately matching the respective CAD model, is singled out for the subsequent experimental analyses. An illustration of the rectangular plectrum with the denoted length and width is shown in Figure 7.6a, while the resulting shape achieved via AM is displayed in Figure 7.6b.

(a) (b) (c)

Figure 7.6. Illustration of the rectangular plectrum (a), 3D printed rectangular plectrum (b) and the symmetrical two-plectra rotor design (c) [120].

Due to the previously mentioned anisotropy issues, inherent to AM, manifested in the vari-

ation of the mechanical properties of a 3D printed object with respect to its position and orientation during the manufacturing process [12, 35, 62, 92], the arrangement of the plectra on the rotor also needs to be amended. The improved rotor, displayed in Figure 7.6c, is reduced to only two symmetrically placed rectangular plectra, printed in the same orientation, thus possessing the same mechanical properties. The use of the rectangular plectrum shape, in combination with the improved rotor design, allows achieving an adequate repeatability in the measured PEH response results. As the effects of several plectrum design parameters are being studied, namely the plectrum material, the area moment of inertia I_x, mm^4, and the length l, mm, of the plectrum, together with one influencing the plucking conditions, i.e., the rotating speed n, min^{-1}, of the DC motor, a DoE methodology is employed to reduce to required number of experiments. For that purpose, the Latinised centroid Voronoi tessellation (LCVT) DoE variant [19, 112, 122] is utilized to generate 20 random combinations of the selected parameters, defining the properties of a plectrum. The area moment of inertia and the length as the parameters representing the plectrum geometry, as well as the rotating speed of the DC motor, are then defined as continuous variables, varying within pre-set ranges listed in Table 7.1. On the other hand, the plectrum material is defined as a discrete variable; the herein considered materials are: PA, PC, ABS PLA. While possessing fairly comparable mechanical properties in terms of e.g. the tensile strength [46, 92, 94], these materials can vary significantly in terms of the respective surface roughness characteristics caused by the different behaviour of the materials when used as FDM filaments. This fact could, in turn, have a substantial impact on the plucked PEH responses [13, 42, 82, 96, 120]. The combinations of these variables, generated via the LCVT methodology, defines the 20 individual experiments, using 3D printed rotors made from different materials, each equipped with two symmetrical plectra.

Table 7.1. Ranges of values of the studied parameters [120].

Studied parameter	
$\boldsymbol{I_x}$**, mm^4**	0.25 – 0.5
***l*, mm**	9 - 13
$\boldsymbol{n_0}$**, min^{-1}**	60 - 200

The resulting rotors are then employed to subject the aforementioned rectangular PEH to plucking excitation, while measuring their respective RMS voltage outputs in an oscillation cycle generated at the optimal load resistance of the EH device, R_L = 5 kΩ [70]. The average power outputs resulting in each of the LCVT-based experimental points, calculated from the respective average voltages in five excitation cycles, are listed in Table 7.2., along with the plectrum material used in the specific experiment.

Table 7.2. Power output values for the DoE generated combination of variables [120].

Exp. No.	Material	*P*, mW	Exp. No.	Material	*P*, mW
1	PC	1.180	11	ABS	0.237
2	ABS	0.713	12	PA	0.308
3	PA	0.613	13	PC	0.482
4	ABS	0.789	14	PC	0.838
5	ABS	0.268	15	ABS	0.243
6	PA	0.827	16	PLA	0.155
7	PLA	0.764	17	PC	0.833
8	PC	0.631	18	PA	0.510
9	PA	0.268	19	PLA	0.662
10	PLA	0.823	20	PLA	0.313

As it can be observed in Table 7.2. the results vary, in terms of generated power, between P ~ 0.15 mW, generated by the 12.2 mm long PLA plectrum with an are moment of inertia I_x = 0.25 mm^4 rotating at n = 144.4 min^{-1}, all the way to P ~ 1.2 mW, which is generated by a 9 mm long plectrum made from PC, with the moment of inertia I_x = 0.33 mm^4, while rotating at a speed of n = 132.8 min^{-1}. The experimentally attained results are then paired with the corresponding combinations of variables devised via the LCVT DoE approach, and analysed using the response surface methodology [39-40, 123]. The resulting quadratic regression model [39-40, 123], described by Equation 7.1, provides, finally a comprehensive description of the effects of the studied variables on the PEH response, with a different set of constants representing different plectrum materials, as listed in Table 7.3. The thus obtained model is characterised by a coefficient of determination of R^2 = 99.4%, enabling the description of more than 99% of the variance of the analysed plectrum design parameters [120].

$$P = a - b \cdot I_x - c \cdot n_0 - 2.04 \cdot l + 15.3 \cdot I_x^2 + +4.2 \cdot 10^{-5} \cdot n_0^2 + 8.79 \cdot 10^{-2} \cdot l^2 + 0.1234 \cdot I_x \cdot n_0 + +1.305 \cdot I_x \cdot l + 2.92 \cdot 10^{-3} \cdot n_0 \cdot l \quad (7.1)$$

Table 7.3. Quadratic regression model constants for different plectrum materials [120].

Constant	PA	PC	ABS	PLA
a	23.5	16.7	23.9	19.2
b	17.1	2.17	18.8	8.9
c	0.098	0.083	0.095	0.086

The two plots of the corresponding residuals (cf. Section 5) [48], important in understanding the viability of the developed regression model, are shown in Figure 7.7. In Figure 7.7a a close to normal distribution can be observed in the frequency of residuals plot, with a clearly centred

maximum. The residuals vs. fits plot, displayed in Figure 7.7b, shows, in turn, that the points are distributed fairly randomly, i.e., there is no obvious trend. These observations indicate that the quadratic model describing the effects of the plectrum and plucking parameters is not distinctly biased, i.e. does not favour a specific portion of the analysed data [48].

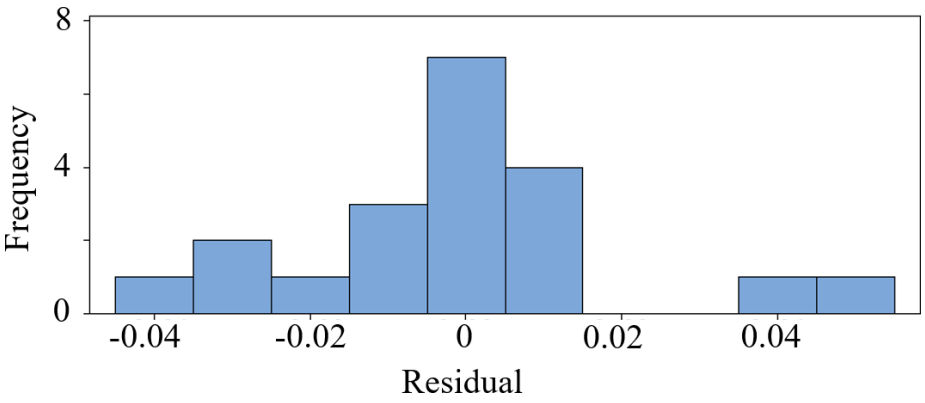

(a)

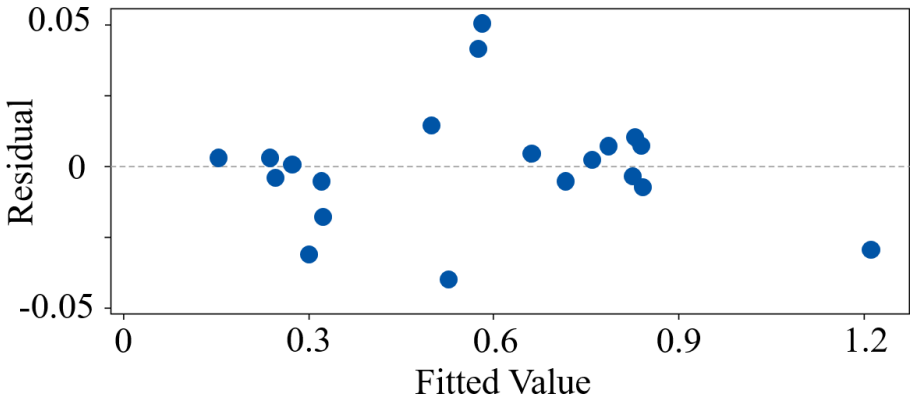

(b)

Figure 7.7. Plectrum model residual plots: frequency vs. residuals (a), and residuals vs. fits (b).

An optimization algorithm based on the Generalized Reduced Gradient (GRG2) code [138] is then applied to the quadratic model of Equation 7.1 to determine the optimal combination of the studied variable plectrum design parameters, within the limits given in Table 7.1., resulting in the highest achievable power outputs. As the plectrum material is defined as a discrete parameter, a separate optimization is carried out for each of the studied materials, by using the respective constants reported in Table 7.3. The maximum achievable power outputs paired with the respective combination of parameters are reported in Table 7.4., where it can be observed that, in this frame, the highest power output of $P_{max} \sim 5.1$ mW can be generated when the PEH is excited by a 9 mm long plectrum made from PC, with $I_x = 0.5$ mm^4, while rotating at $n = 200$ min^{-1}. What is more, it can also be noticed that in all considered cases the optimal values of the studied parameters, resulting in the highest power outputs, coincide with different combinations

of either the upper or the lower limits set for the plectrum area moment of inertia I_x and the rotating speed of the rotor n. When, in turn, the length of the plectrum is considered, it can be observed that, when the maximal power output is the primary requirement, the model shows a trend favouring shorter, and therefore stiffer, types of plectra.

Table 7.4. Maximal power and optimal parameters for different plectrum materials [120].

Material	**PA**	**PC**	**ABS**	**PLA**
P_{max}, **mW**	3.72	5.06	3.85	3.46
I_x, **mm^4**	0.25	0.5	0.25	0.5
l, **mm**	9	9	9	9
n_0, **min^{-1}**	60	200	60	200

As the optimal plectrum length corresponds with the lower limit of the considered range for all the studied cases, it can be regarded as a constant - l = 9 mm, enabling a graphical representation of the studied effects on the PEH performances. Four individual response surface graphs are then created for each of the considered plectrum materials (Figure 7.8.), showing the influence of the area moment of inertia I_x and of the plectrum rotation speed n of a 9 mm long plectrum on the power generated by the plucked rectangular PEH. By examining the thus attained response surface graphs, it can be seen that the maximum PEH performances in terms of the power outputs can be achieved by combining the parameter values coinciding with the limits of the considered variable ranges of values, concurring with the conclusions based on the data reported in Table 7.4.

Moreover, the graphs for all of the considered materials display a more or less distinct propensity to form a “saddle”, which could indicate the presence of multiple maxima, occurring outside of the herein studied ranges of the considered design variables. It is also evident that in the case of plectra made from PA and ABS, shown respectively in Figures 7.8a and 7.8c, the best performances are attained by combining low values of both the moment of inertia I_x and the rotating speed n. On the other hand, the plectra made from PC and PLA, displayed in Figures 7.8b and 7.8d respectively, show a different trend, being able to generate the maximum power output at high values of the moment of inertia I_x as well as of the rotating speed n [120]. These conclusions provide the basis and guidelines for further studies of the complex interaction of the plectrum parameters, as well as of their effects on the response of a plucked PEH. It is also shown that a significant reduction in the number of required experiments can be achieved by using the LCVT DoE methodology, while maintaining the coefficient of determination at values $R^2 > 99\%$, resulting in an unbiased quadratic model.

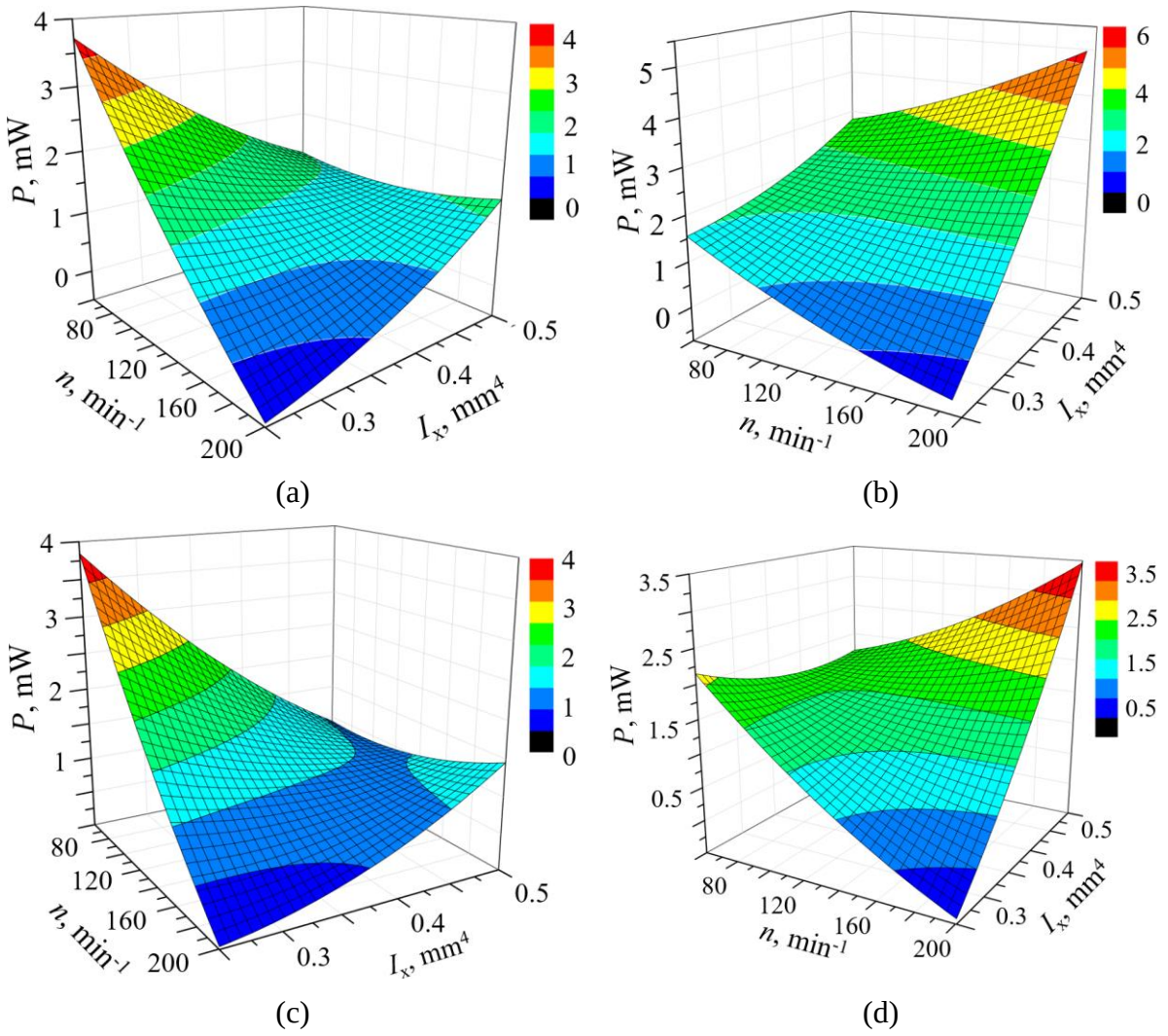

Figure 7.8. Power outputs resulting from the model of Equation 7.1 with a 9 mm long plectrum made from different materials: PA (a), PC (b), ABS (c), and PLA (d) [120].

The optimization results show that in all the considered cases the optimal values of the studied parameters tend to coincide with the limits of their respective ranges. The tendency to form a saddle, particularly evident in the case of PLA, but also observed for the remaining materials, suggests also that the quadratic model might have additional maxima occurring outside of the used ranges of the considered values.

7.3. Development of a wearable EH-FUC powered device

A major limiting factor in the design of wearable devices, as it is mention throughout this work, is the size of the device. In the herein presented frame, an upper limit of 50 mm in diameter is set for a compact wrist-worn watch-like device. In addition, the device should ideally be able to accommodate more than one miniaturized optimized segmented EH device. The therein

used PEHs need to be excited by deflecting their free ends via rotating plectra, with the rotation being provided by a rotating flywheel, collecting ambient kinetic energy and converting it into periodical excitation impacts. Ideally, the device should allow further developments and upgrades in terms of ambient energy collection (flywheel modifications), as well as in terms of the plucking process itself (plectra modifications). Following the results presented in Section 6, as well as the conclusions based on them, the best performing, i.e., the optimally segmented PEH device without stress concentrators (cf. Section 6) is therefore selected to be utilized for power generation in the herein proposed prototype of a wearable device. Two such PEH devices are, in turn, manufactured by cutting the optimized segments from the commercially available rectangular PEH [153] using waterjet cutting technology [170], to be implemented in the wearable device. Due to technological limitations of waterjet cutting in terms of the minimal jet diameter - implying the minimal width of the cut, the device differs slightly from the optimized segments presented above, in order to accommodate the two segments. The dimensions of the optimized device are in Figure 7.9.

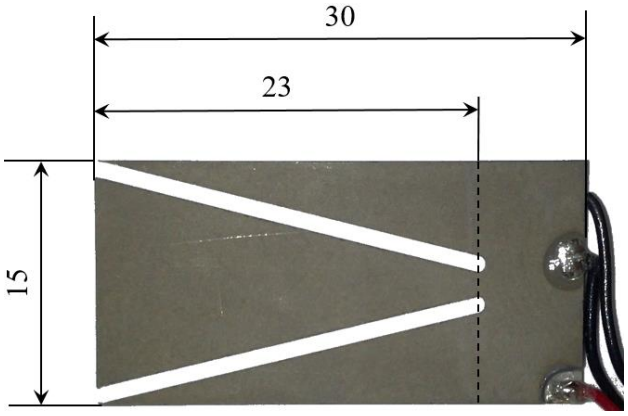

Figure 7.9. Overall dimensions and free end length of the optimized segmented PEH.

The basis of the herein proposed wearable device, shown in Figure 7.10a, comprises then an ergonomically designed platform aimed to be worn at the wrist, similarly to a regular watch, using standard bands attached to the designated areas. A pillar is located in the centre of the platform, along the flywheel axis of rotation, in order to accommodate the two SKF W617/3 R and W617/3 [198-199] ball bearings enabling the smooth rotation and positioning of the flywheel (Figure 7.10b). The two clamping mechanisms holding the PEHs are also affixed to the platform. In the proposed design configuration, the PEHs are fixed using two compliant clamping mechanisms, shown in Figure 7.11a, attached to the platform. The optimized PEHs are inserted between the clamping plates (Figure 7.11b), and held in place by the force applied via the clamping bolts deforming the mechanism and bringing the plates closer to each other.

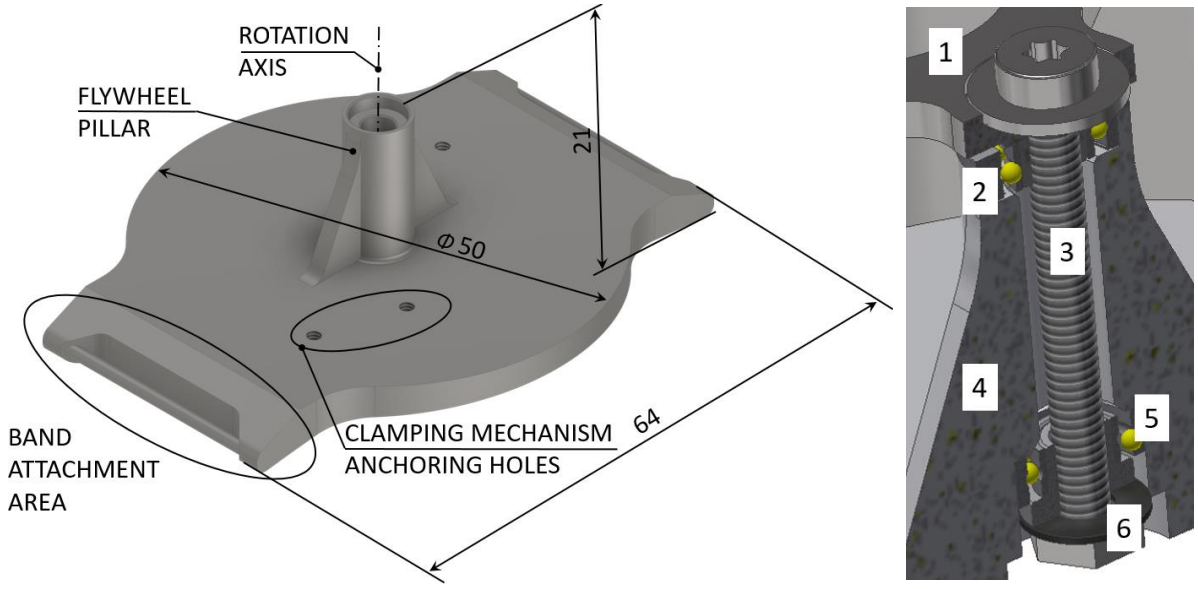

(a) (b)

Figure 7.10. Wearable device platform (a), and flywheel bearing arrangement inside the pillar denoted as flywheel (1), top bearing (2), connecting bolt (3), pillar (4), bottom bearing (5) and bottom-end tightening nut (6) (b).

The plates are designed according to the guidelines and recommendations presented in Section 4, ensuring that the free working length and the clamping fixture arrangement are as close as possible to the nominal values. What is more, the design includes a channel, allowing enough space for the electrical leads and the respective soldering points, without affecting the clamping.

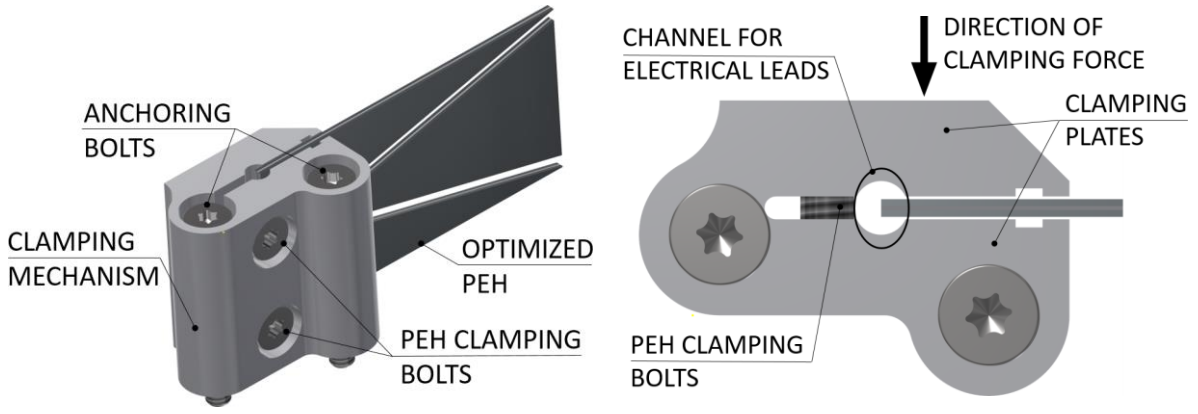

(a) (b)

Figure 7.11. Overall PEH clamping mechanism (a) and its detailed view (b).

The clamping mechanisms are placed symmetrically on each side of the central pillar, and slightly offset to accommodate the full length of the optimized PEHs, as it can be seen in Figure 7.12. What is more, such a placement of the clamping mechanisms, as well as of the PEHs, enables the utilization of a significant portion of the space, marked in red, available between

the flywheel path (marked in black) and the EH devices themselves, which are offset by a distance equal to or larger than the largest allowable initial tip deflection δ_{z_max}. This space can, in turn, be used for the placement of the circuitry belonging to the wearable medical device, such as the sensors, the processors, and/or the energy storage or communication components.

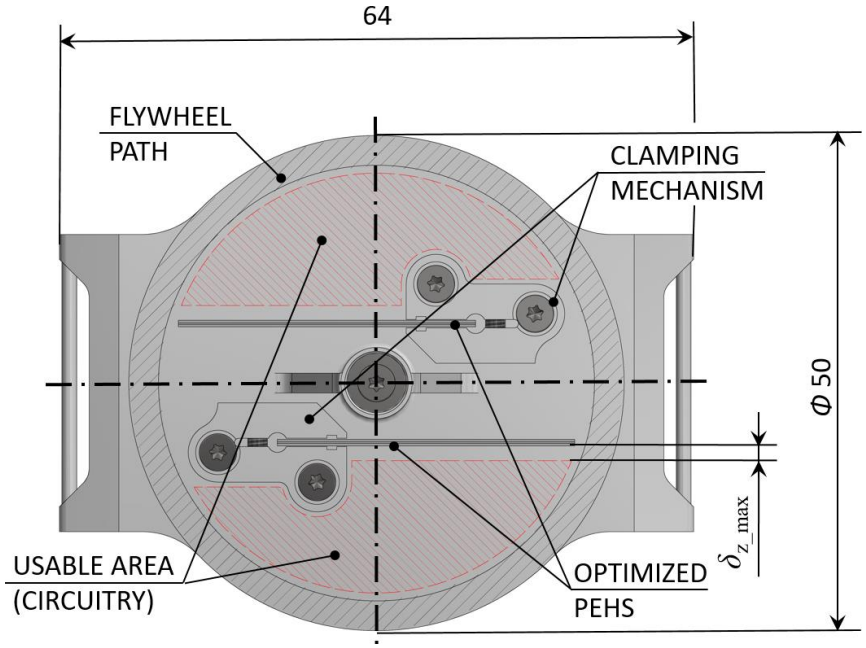

Figure 7.12. Arrangement of the EH components inside the proposed wearable device.

The modular flywheel, shown in Figure 7.13a, used to collect the ambient kinetic energy generated by the motion of the user's hand, consists of a rotating mass, offset from the axis of rotation. Two exchangeable modules (Figure 7.13b), attached to each end of the rotating mass, comprise three separate plectra able to pluck the tips of the respective segments of the optimized PEHs (dimensioned according to the guidelines derived in the part of the work dedicated to the study of the respective process parameters) thus providing their periodical excitation. Due to its modular design, the flywheel allows the wearable device to be used as a testbed for further developments and refinements of the plucking process, that could result from the study and the optimization of the design of the plectra themselves. Although the here illustrated prototype is to be manufactured from a polymer via the process of additive manufacturing, described in the following subsection, for functional reasons the flywheel should be made out of higher density material, e.g. metal, or additional weights should be attached to it, e.g. by integrating several high-density (e.g. tungsten) weights in the body of the flywheel. The complete prototype of the proposed device, comprising the two compliant mechanisms clamping two optimized segmented PEHs attached to the platform, and a rotating modular flywheel with attached exchangeable plectra, is, finally, shown in Figure 7.14.

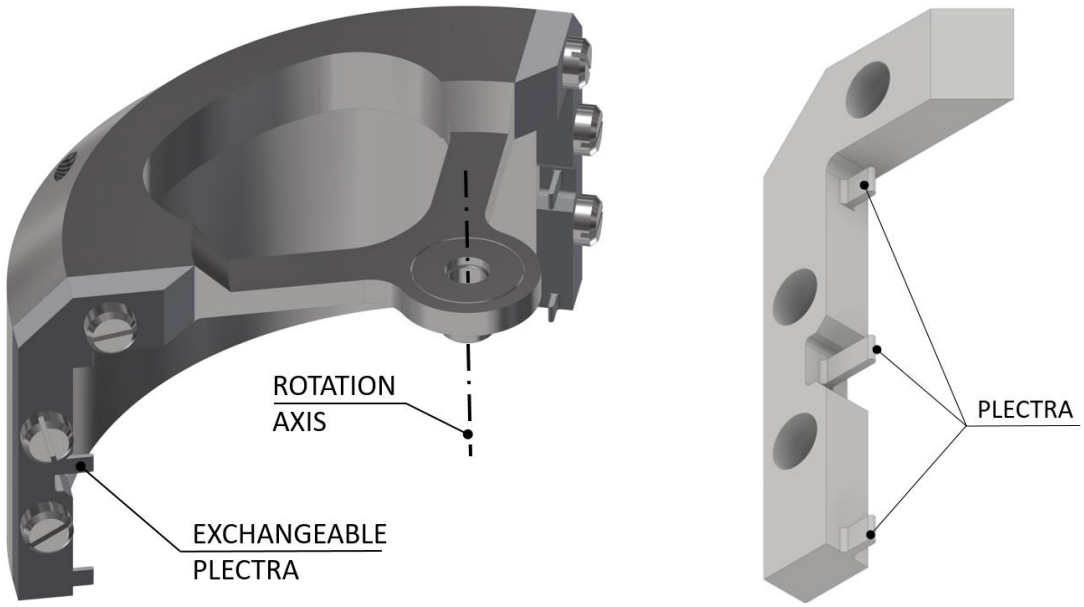

(a) (b)

Figure 7.13. Rotating modular flywheel (a), and the exchangeable module with three separate plectra (b).

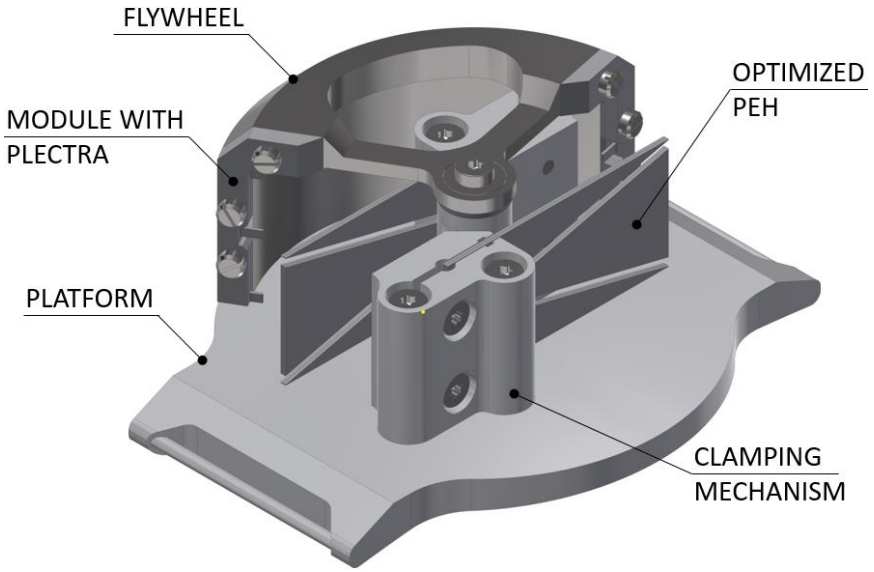

Figure 7.14. 3D model of the wearable device prototype powered by optimized PEHs.

While still being somewhat bulky, the size of the prototype is comparable to some commercially available smart watches [44]. The expected power output of this configuration, i.e., of the two optimized segmented PEHs plucked by the maximal allowable tip deflection for each individual segments, adequately paired with the respective optimal electrical loads, and thus operating in the ideal conditions, each able to provide a maximum power output of ~ 134 mW, would amount to ~ 268 mW. The thus achieved power levels are more than enough to power a medical wearable device, such as the one suggested in Section 3, requiring ~ 115 mW

in normal operation, without considering duty cycles. When the duty cycles are taken into account (cf. Section 3), the reduced power requirement of ~ 5 mW is easily met and exceeded by the combined output of the two segmented PEHs both in terms of maximum as well as average power i.e. ~ 6.8 mW.

In the frame of this work, an additive manufacturing approach using metal powders would ideally be employed to fabricate some of the components of the wearable device, i.e., the flywheel and the clamping mechanisms, thus enabling the construction of a functional prototype. These components would provide adequate mass (flywheel) and adequate tensile strength (clamping mechanism) properties, so as to ensure enough force for PEHs' excitation and to withstand these forces, transmitted through the clamped PEHs during the plucking process. A demonstration model of the prototype device, produced using the Stratasys® Fortus 250mc machine, from ABS combined with soluble supports, is shown in Figure 7.15. The prototype model is equipped with a protective cover (Figure 7.15a), enclosing the FUC mechanism, also serving as a mounting platform for additional electronic components of the wearable medical device, e.g. a display or various controls or connection ports. Figure 7.15b, on the other hand, shows the FUC mechanism and the two optimized PEHs held in place by the compliant clamping mechanisms. A hook-and-loop fastener band is attached to the base of the device, enabling to wear it on the wrist as a watch.

(a) (b)

Figure 7.15. 3D printed demonstration model of the devised wearable device prototype with (a) and without the protective cover (b).

A short introduction to additive manufacturing was given in this section, along with an outline of the most common features and innate issues. An extensive experimental DoE based experimental study of plucking parameters, i.e. plectrum design parameters, material and plucking speed was carried out, providing a valuable insight in the complex mechanism of plucking excitation as well as useful guidelines for an optimal plectrum design. Finally, a concept design

of a watch-like wearable device, comprising two optimally segmented PEHs plucked by a FUC mechanism, was devised, able to generate up to ~ 268 mW of maximum and ~ 6.8 mW of average power, providing thus more than enough power, for a wearable medical device aimed for autonomous health monitoring, i.e. ~ 115 mW without considering duty cycles and ~ 5 mW when duty cycles are considered.

The following and final section of this thesis will provide the conclusions derived in the herein presented research, as well as evidence the scientific contributions of the performed work. An outlook to the topics to be addressed in the prosecution of the herein conducted research will also be given.

8. CONCLUSIONS AND OUTLOOK

The initial part of the thesis provided a thorough and comprehensive description of wearable technologies, their most common types as well as the latest trends in their application. The basics principles of energy harvesting modalities were presented, with particular attention dedicated to the piezoelectric approach applied to the harvesting of kinetic energy generated by human motion. Specific issues related to the random excitation, innate to the most commonly utilized bimorph cantilever devices, especially present in wearable applications, were covered in detail. In fact, the considered PEHs are characterized by a narrow area of optimal operation around their eigenfrequencies, whereas the excitations generated by human motion are random. The most promising approaches to address these issues, reported in literature, were thus analysed. In this frame, a distinct focus was put on geometry optimization combined with the frequency up-conversion approach, potentially leading to a novel type of EH-based powering of wearable devices that could result in improved performances. An extensive overview of the state-of-the-art in energy harvesting integration in wearable technologies, covering a wide range of recent literature, was also presented here, both in terms of frequency up-conversion and geometry optimization. Through a detailed examination of previous art, it was observed that the majority of the reported studies does not consider the strength and fatigue of the PEHs, with most of the studies completely omitting the stresses occurring within the piezoelectric layers, limiting themselves to the criteria of maximal performances. This, in turn, results in either a noticeably limited lifetime of such devices, as well as their unsuitability for real-life applications, or in significantly lower performances if a longer device lifetime is required.

In the next section of the work, aimed at identifying the power requirements to be matched by the miniaturized EH device to be developed in the present study, the focus was on analysing the most common low-power electronic components used in a typical wearable medical device as the application area the work will be directed toward. The thus used components, ideally to be assembled in a watch-like wearable medical device, are hence divided in categories based on their respective functions. Wherever this was possible, commercially available components were considered in this frame, while recently published research was used where the technology was still under development. The concept of the typical duty cycles, based on well-established medical practices, was used to achieve a significant reduction in power requirements, while providing all the needed functionality in the foreseen applications framework. An example of a factual wearable medical device was proposed in this section, comprising the previously described components, and its overall power requirement was estimated at ~ 6.8 mW when the

duty cycles are considered.

To enable the development of an innovative design configuration of an optimized and miniaturized piezoelectric EH device that could produce such a power level, suitable analytical and experimental tools are needed. The experimental and numerical methods employed in this work were thus comprehensively presented in Section 4. A short outline covering the most common analytical models used to describe the behaviour of PEHs was given here. A detailed description of the complex numerical ANSYS® models employed in this work was then provided, covering the finite element types as well as the applied boundary conditions. A thorough mesh sensitivity analysis was also carried out to determine the optimal shape and size of the finite elements to be used, that resulted in a balance between the accuracy of the obtained results and the computational times. The four numerical analyses types, used for modelling the behaviour of piezoelectric energy harvesters were described next and applied to the conventional rectangular PEH. In this section the two used experimental setups, i.e., the harmonic analysis setup, based on the B&K® electrodynamic permanent magnet shaker providing the excitation of the base of the PEH, and the impact (FUC) analysis setup, comprising rotating plectra plucking a clamped PEH, were described next. The technical characteristics of all the components used in the setups were provided. A brief overview of clamping methods and conditions around the clamping area was also provided, offering some basic guidelines for the adequate clamping plate design.

Based on the described tools used in the work, in Section 5, advancing on prior art, novel designs of PEHs are thus conceived, modelled and investigated with the aim of optimizing their performances while miniaturizing their dimensions and considering also the respective strength constraints. The optimization of the PEH geometry was thus numerically carried out and experimentally verified. The initial design studies of the effects of shape variation, in terms of the segmentation of the geometry and the addition of stress concentrators, were thus numerically analysed, and the conclusions based on the obtained results showed promising trends in terms of performance improvements. The optimization of the first two suggested PEH design configurations, one obtained by segmenting the available design space of a conventional rectangular PEH so as to shape it in an inverted trapezoid and two trapezoidal segments, and the other configured as a shape with a V notch added at the clamped end of a rectangular PEH, was performed next. A central composite DoE was employed to generate random combinations of the design variables defining these shapes, and a 3D model was created and analysed using the modal and harmonic FE analyses. From the pairing of the FE results with the respective combinations of geometrical design variables, two quadratic models describing the effects of these variables on the PEH responses were obtained. An optimization algorithm was then applied to

these models to obtain the best possible combination of the variables defining the designs of the harvesting transducers resulting in the maximal PEH performances. The thus established innovative PEH design configurations were finally evaluated using FE analyses, with the resulting data showing a considerable improvement in performances in terms of the output voltages and powers. Another shape variation, based on adding stress concentrators along the edges of the optimized segmented PEHs, was introduced here as well, to test if the zones with increased stress levels could lead to a further improvement in voltage generation.

As devices aimed to collect and transduce vibration energy, PEHs are subjected to dynamical working conditions. With this in mind, a comprehensive investigation of the optimized PEHs' structural strength was also carried out here, using the FE stress analyses. Both tip deflection and the tip masses were thus studied with the goal of assessing the maximal allowable loads applicable to the optimized devices, while maintaining the stress levels in the piezoelectric layers below the fatigue limit. Extending and improving considerably the available state-of-the-art, the attained results, used in the subsequent experiments, ensure the long-lasting operation of the developed optimized devices, along with a more realistic view of their respective performance figures. The measurement data, attained by performing experimental studies on the thus obtained optimized PEHs, as well as the critical analysis and the assessment of the resulting data, were reported in Section 6 of the thesis. To assure that the geometry of the thus used numerical models is as close as possible to that of the actual devices, the layer thicknesses of a commercially available rectangular PEH, on which the optimized shapes are based, were measured first via a high precision optical instrument. The numerical model was validated next, by comparing the FE results to the data measured by using the two experimental setups. A good match ($\leq$ 5% differences) between the results of FE analyses and the experimental data was obtained in all the considered cases. The experimentally validated FE model was therefore used to determine the optimal load resistances of the studied devices, via the well-established method of multiple harmonic analyses with varying load resistance values. The originally devised optimized PEHs, cut from the aforementioned commercial rectangular device, were experimentally tested next, using the FUC experimental setup, by plucking their free ends, while keeping the respective initial deflections below the values established by the performed strength analyses. The resulting responses were compared to the respective FE ones, displaying a very good match, both in terms of the eigenfrequency and of the voltage outputs, with differences below 5%. Due to the limitations of the utilized experimental setup, the initial displacements differed in the considered experiments, making the comparison of the responses of the considered optimized shapes impossible. This led to the study of the voltage values normalized over the initial

tip displacement, facilitating the comparison between the output values generated by the various studied miniaturized devices' designs. These values were then used to calculate the power outputs of the PEHs in terms of the absolute, the average as well as the specific power outputs. A significant improvement in the performance was observed when the outputs of the optimized segmented shapes were compared to that of the conventional rectangular one. The trapezoidal segments alone outperformed thus the rectangular one by 28% when the absolute power is considered, and by almost five times in terms of the specific power output. The power output of the inverted shape, that should be seen as an addition to that of the two trapezoidal segments, although being lower, is still comparable to that of the rectangular device. What is more, a noticeable performance gain was observed when stress concentrators were added along the edges of the segmented PEHs. When compared to the rectangular shape, the most significant performance gain was therefore exhibited by the trapezoidal segment with added stress concentrators, outperforming the conventional shape in terms of the specific power output by more than 5.5 times. The power outputs achievable by the optimized PEHs excited by the respective largest allowable tip displacements, given by the here consequently investigated strength considerations, were also calculated, and the segmented device was found to exhibit the best overall performances in terms of the maximal power, allowing the attainment of 134.06 mW (~ 4 times more than a comparable rectangular PEH). In this case the addition of stress concentrators limits the initial displacement applicable to the modified segments, lowering their maximal achievable overall performance. It was also noted here that quite different behaviour and performance trends are exhibited by the considered class of harvesting devices when the limitations due to fatigue strength are considered, compared to the cases generally considered in prior art where the best performances are calculated based on the maximal voltage and power output design criteria only. In Section 7 a brief outline of the additive manufacturing technologies, a versatile and fast means to develop and adapt the prototypes of the devised class of devices for the foreseen application in a watch-like wearable device with several medical sensors with the respective data elaboration and transmission modules, was given, with a particular emphasis on the FDM method, used in this work to manufacture a demonstration prototype of the wearable device, as well as of the plectra for the planned subsequent experimental studies. A thorough experimental analysis of the effects that 3D printed plectrum design parameters and plucking conditions have on the response of a plucked PEH was performed in this section as well. By using the LCVT DoE methodology applied to the selected variables, as well as by assessing the resulting performance via experimental measurements, a quadratic model was obtained, describing the concurrent influence of these variable parameters on the PEHs' responses. Via an

optimization algorithm, the optimal combinations of the studied parameters were therefore determined for each of the four plectrum materials, coinciding with the limits of the considered ranges of parameter values. Moreover, the resulting response surface graphs display a clear tendency to form a saddle, suggesting that multiple maxima outside of the considered value ranges could be present. All of this enabled the concretization of the design of a wearable device based on the combination of optimized PEHs excited via a FUC mechanism. The essential components of such a device, as well as of its most important design features, were thoroughly described. The nominal power output of such an original miniaturized and optimized design configuration was estimated to be $P \sim 270$ mW, i.e., the combined output of two segmented PEHs exceeds by far the power levels needed for the foreseen application in the medical sector, while enabling the concurrent powering of up to three different medical sensors.

The results and the conclusions presented in this work provide a deep understanding of the behaviour of kinetic piezoelectric bimorph energy harvesters, particularly those subjected to random human motion excitation, converted via the FUC approach into the harmonic oscillations of the transducers themselves. The herein developed novel shapes, created via an innovative optimization approach combining a DoE methodology and experimentally validated numerical models, display a significant gain in performances in relation to the conventional rectangular device of comparable size. The innovative combination of FUC and optimized PEH geometry, presented in this work, offers furthermore the benefits of both design approaches, resulting in a miniaturized wearable device able to generate a substantial amount of power from kinetic energy caused by random human motion. What is more, this work points out the necessity to include strength criteria in designing PEHs, so as to obtain realistic performance figures and ensure their long-term operation in real life applications.

All these aspects constitute important scientific contributions of the work performed in the framework of the doctoral thesis. The effects of geometrical design parameters on the PEH performances were extensively studied, and optimal combinations of these parameters were assessed, resulting in novel optimized PEH design configurations displaying significantly improved performances compared to the conventional rectangular shape, when excited by plucking the free end. The optimization was carried out by using an original approach combining the DoE methodology and complex numerical analyses, forming thus a comprehensive mechanical engineering approach for achieving optimized PEH performances. What is more, by considering the generally omitted fatigue strength of the brittle piezoelectric layers, longer operating cycles of the optimized PEHs were ensured and a more practical performance figure is presented. The comprehensive experimental investigation of the effects of the impact excitation

mechanism's parameters on PEH performances provided valuable guidelines for the optimal plectrum design. The conceptual design of a compact watch-like device, comprising a miniaturized FUC mechanism used for the excitation of two optimized segmented PEHs was also presented; it is capable of generating an estimated maximal power of $P \sim 270$ mW and an average power of $P \sim 6.8$ mW, which is adequate for powering a miniaturized wearable medical device aimed for autonomous health monitoring.

This work also presents the basis for further research and development of optimized wearable devices. Thorough harmonic testing will, thus, be performed in future work on the optimized shapes both with and without tip masses, in order to study the influence of the loads and boundary conditions on the optimal load resistance values. A variable stress amplitude, matching more closely the studied load case, should be used to more accurately determine the maximal tip displacements, and the clamping stress induced in the piezoelectric layers should also be considered. An analysis of non-uniform notch distribution along the PEH edges should be carried out, to study the effects on the PEH response. By improving the FUC setup, a more controlled and predictable excitation could then be achieved, eliminating the need for voltage normalization. The clamping accuracy as well as the Rayleigh damping coefficients need to be addressed as well, so as to enhance the repeatability of the results, and bring the FE responses even closer to the experimental ones. A more accurate figure of merit should also be considered, to enable taking into account the plucking speed, which could have a significant effect on the PEH dynamical responses. As the herein presented devices are aimed for biomedical applications, a more suitable lead-free piezoelectric material should be considered in future research. In terms of plectrum optimization, a wider range of values needs to be selected, in order to assess the existence of possible maxima occurring outside the range of parameters considered in the herein performed study. Such an optimized plectrum design should then be included in the final design of the autonomous watch-like wearable device. A functional prototype of this device needs to be produced by employing metal AM technologies for the manufacturing of some of the key components, such as the clamping mechanisms and the flywheel. The resulting device has to be tested in both laboratory as well as in real life conditions, and its performance figures need to be assessed. The final device will therefore provide a flexible foundation on which the performances of a multitude of autonomous wearable devices could be assessed, aimed at numerous applications not only as medical devices, e.g. for remote patient monitoring, telemedicine and automated drug delivery all the way to work safety and professional sports, but also as key elements in IoT and Industry 4.0, as well as in structural health-monitoring (SHM) systems for airplanes or for civil engineering structures and even space applications.

List of References

[1] Y. Adesida, E. Papi, and A. H. McGregor, 'Exploring the Role of Wearable Technology in Sport Kinematics and Kinetics: A Systematic Review', *Sensors*, vol. 19, no. 7, 1597, 2019.

[2] S. Afroj, et al., 'Highly Conductive, Scalable, and Machine Washable Graphene-Based E-Textiles for Multifunctional Wearable Electronic Applications', *Adv. Funct. Mater.*, vol. 30, no. 23, 2000293, 2020.

[3] 'Agilent DSO-X 2012A oscilloscope', https://www.keysight.com/zz/en/support/DSOX2012A/oscilloscope-100-mhz-2-analog-channels.html, accessed: 18-Jan-2022.

[4] M. M. Ahmad, N. M. Khan, and F. U. Khan, 'Review of frequency up-conversion vibration energy harvesters using impact and plucking mechanism', *Int. J. Energy Res.*, vol. 45, no. 11, pp. 15609–45, 2021.

[5] S. Ahmad, B. M. Irons, and O. C. Zienkiewicz, *Theory Reference for the Mechanical APDL and Mechanical Applications*. Canonsburg, PA, USA: ANSYS, Inc., 2009.

[6] J. Ajitsaria, S. Y. Choe, D. Shen, and D. J. Kim, 'Modeling and analysis of a bimorph piezoelectric cantilever beam for voltage generation', *Smart Mater. Struct.*, vol. 16, no. 2, pp. 447–54, 2007.

[7] B. de Almeida and R. Pavanello, 'Topology Optimization of the Thickness Profile of Bimorph Piezoelectric Energy Harvesting Devices', *J. Appl. Comput. Mech.*, vol. 5, no. 1, pp. 113–27, 2018.

[8] R. Ambrosio, A. Jimenez, J. Mireles, M. Moreno, K. Monfil, and H. Heredia, 'Study of Piezoelectric Energy Harvesting System Based on PZT', *Integrated Ferroelectrics*, vol. 126, no. 1, pp. 77–86, 2011.

[9] A. A. G. Amer, S. Z. Sapuan, N. Nasimuddin, A. Alphones, and N. B. Zinal, 'A Comprehensive Review of Metasurface Structures Suitable for RF Energy Harvesting', *IEEE Access*, vol. 8, pp. 76433–52, 2020.

[10] B. Antonin, *Propedeutika Interne Medicine*. Zagreb, HR: Jumena, 1989.

[11] S. Aras, T. Johnson, K. Cabulong, and C. Gniady, 'GreenMonitor: Extending battery life for continuous heart rate monitoring in smartwatches', in *17th Int. Conf. E-health Netw., Appl. & Services (HealthCom)*, Boston, MA, USA, pp. 317–22, 2015.

[12] G. Aroganam, N. Manivannan, and D. Harrison, 'Review on Wearable Technology Sensors Used in Consumer Sport Applications', *Sensors*, vol. 19, no. 9, 1983, 2019.

[13] T. Arrigoni, S. Zelenika, E. Kamenar, and T. Schnurrer Luke Vrbanic, 'Design of the Prototype of a Full Arm Mechatronics Rehabilitation Device', in *DAAAM Proceedings*, vol. 1, B. Katalinic, ed. DAAAM International Vienna, pp. 0016–0024, 2018.

[14] H. F. Atlam and G. B. Wills, 'IoT Security, Privacy, Safety and Ethics', in *Digital Twin Technologies and Smart Cities*, M. Farsi, A. Daneshkhah, A. Hosseinian-Far, and H. Jahankhani, eds. Cham, CH: Springer International Publishing, pp. 123–49, 2020.

[15] G. Backman, B. Lawton, and N. A. Morley, 'Magnetostrictive Energy Harvesting: Materials and Design Study', *IEEE Trans. Magn.*, vol. 55, no. 7, pp. 1–6, 2019.

[16] Y. Bai et al., 'Investigation of a cantilever structured piezoelectric energy harvester used for wearable devices with random vibration input', *Mech. Syst. Signal. Pr.*, vol. 106, pp. 303–18, 2018.

[17] Y. Bai, H. Jantunen, and J. Juuti, 'Energy Harvesting Research: The Road from Single Source to Multisource', *Adv. Mater.*, vol. 30, no. 34, p. 1707271, 2018.

[18] 'BAK, Lithium polymer 300 mAh battery LP-402933-IS-3 datasheet', www.farnell.com/datasheets/1666647.pdf, accessed: 25-Nov-2021.

[19] B. Bao, Q. Wang, N. Wu, and S. Zhou, 'Hand-held piezoelectric energy harvesting structure: Design, dynamic analysis, and experimental validation', *Measurement*, vol. 174, p. 109011, 2021.

[20] C. Bao, Y. Dai, P. Wang, and G. Tang, 'A piezoelectric energy harvesting scheme based on stall flutter of airfoil section', *Eur. J. Mech. B-Fluid*, vol. 75, pp. 119–32, 2019.

[21] P. Barmuta, G. P. Gibiino, F. Ferranti, A. Lewandowski, and D. M. M.-P. Schreurs, 'Design of Experiments Using Centroidal Voronoi Tessellation', *IEEE Trans. Microwave Theory Techn.*, vol. 64, no. 11, pp. 3965–73, 2016.

[22] D. Benasciutti, L. Moro, S. Zelenika, and E. Brusa, 'Vibration energy scavenging via piezoelectric bimorphs of optimized shapes', *Microsyst. Technol.*, vol. 16, no. 5, pp. 657–68, 2010.

[23] J. Berián, I. Bravo, A. Gardel, J. L. Lázaro, and S. Hernández, 'A Wearable Closed-Loop Insulin Delivery System Based on Low-Power SoCs', *Electronics*, vol. 8, no. 6, p. 612, 2019.

[24] P. Biswal, S. K. Kar, and B. Mukherjee, 'Design and Optimization of High-Performance Through Hole Based MEMS Energy Harvester Using PiezoMUMPs', *J. of Elec. Mater.*, vol. 50, no. 1, pp. 375–88, 2021.

[25] D. Blažević, 'Analysis of mechanical aspects in the design of vibration energy harvesters', PhD Thesis, Rijeka, HR: University of Rijeka, Faculty of Engineering, 2014.

[26] D. Blažević, E. Kamenar, and S. Zelenika, 'Load optimised piezoelectric generator for powering battery-less TPMS', *SPIE (International Society for Optical Engineering) Proceedings*, vol. 8763: Smart Sensors, Actuators and MEMS VI (ed. Schmid U., Sanchez-Rojas J. L. and Leester-Schaedel M.), 2013, pp. 87631K-1 – 87631K-10.

[27] D. Blažević and S. Zelenika, 'Nonlinear numerical modelling and experimental validation of multilayer piezoelectric vibration energy scavengers', *SPIE (International Society for Optical Engineering) Proceedings*, vol. 9517: Smart Sensors, Actuators, and MEMS VII (ed. Sánchez-Rojas J. L., Brama R.), 2015, pp. 95171F-1 – 95171F-13.

[29] S. Bradai, S. Naifar, C. Viehweger, and O. Kanoun, 'Electromagnetic Vibration Energy Harvesting for Railway Applications', *MATEC Web Conf.*, vol. 148, 12004, 2018.

[30] A. Brenes et al., 'Large-bandwidth piezoelectric energy harvesting with frequency-tuning synchronized electric charge extraction', *Sensor. Actuat. A-Phys.*, vol. 302, 111759, 2020.

[31] 'B&K LDS LPA100 power amplifier', https://www.bksv.com/en/instruments/vibration-testing-equipment/vibration-amplifiers/lds-shaker-amplifier/lds-lpa-amplifiers, accessed: 18-Jan-2022.

[32] 'B&K LDS V201 Permanent magnet LDS shaker', https://www.bksv.com/en/instruments/vibration-testing-equipment/lds-shakers/permanent-magnet-shakers/lds-v201, accessed: 18-Jan-2022.

[33] M. Cai, Z. Yang, J. Cao, and W.-H. Liao, 'Recent Advances in Human Motion Excited Energy Harvesting Systems for Wearables', *Energy Technol.*, vol. 8, no. 10, 2000533, 2020.

[34] 'CEDRAT technologies: Amplified Piezo Actuators', https://www.cedrat-technologies.com/en/products/actuators/amplified-piezo-actuators.html, accessed: 26-Aug-2020.

[35] D. Charris, D. Gomez, A. R. Ortega, M. Carmona, and M. Pardo, 'A Thermoelectric Energy Harvesting Scheme with Passive Cooling for Outdoor IoT Sensors', *Energies*, vol. 13, no. 11, 2782, 2020.

[36] G. H. Choi, D. Mun, and S. Han, 'Exchange of CAD Part Models Based on the Macro-Parametric Approach', *Int. J. CAD/CAM*, vol. 2, no. 1, pp. 13-21, 2002.

[37] Y.-W. Chong, W. Ismail, K. Ko, and C.-Y. Lee, 'Energy Harvesting For Wearable Devices: A Review', *IEEE Sensors J.*, vol. 19, no. 20, pp. 9047–62, 2019.

[38] C. Covaci and A. Gontean, 'Piezoelectric Energy Harvesting Solutions: A Review', *Sensors*, vol. 20, no. 12, 3512, 2020.

[39] D. R. Cox and N. Reid, *The theory of the design of experiments*. Boca Raton, FL, USA: Chapman & Hall/CRC, 2000.

[40] A. Dean, M. Morris, J. Stufken, and D. Bingham, *Handbook of Design and Analysis of Experiments*. Boca Raton, USA: CRC Press, 2015.

[41] A. R. Dehghani-Sanij, E. Tharumalingam, M. B. Dusseault, and R. Fraser, 'Study of energy storage systems and environmental challenges of batteries', *Renew. Sust. Energ. Rev.*, vol. 104, pp. 192–208, 2019.

[42] A. Dey and N. Yodo, 'A Systematic Survey of FDM Process Parameter Optimization and Their Influence on Part Characteristics', *J. Manuf. Mater. Process.*, vol. 3, no. 3, 64, 2019.

[43] 'Digikey', www.digikey.com, accessed: 15-Nov-2021.

[44] 'Dimmensions of commercially available smart-watches', www.dimensions.com/collection/smart-watches, accessed: 12-Sep-2021.

[45] 'DinoCapture software', https://www.dino-lite.eu/index.php/en/software/dino-lite-general-software/dinocapture-windows, accessed: 18-Jan-2022.

[46] 'DinoEye Edge AM4025X', https://www.dino-lite.eu/index.php/en/component/k2/item/3629-am4025x, accessed: 18-Jan-2022.

[47] 'Distrelec', www.distrelec.de, accessed: 15-Nov-2021.

[48] N. R. Draper and H. Smith, *Applied Regression Analysis*. Hoboken, USA: John Wiley & Sons, 1998.

[49] N. E. Dutoit, B. L. Wardle, and S.-G. Kim, 'Design considerations for mems-scale piezoelectric mechanical vibration energy harvesters', *Integr. Ferroelectr.*, vol. 71, no. 1, pp. 121–60, 2005.

[50] P. F. Edemekong, D. L. Bomgaars, S. Sukumaran, and S. B. Levy, 'Activities of Daily Living', www.ncbi.nlm.nih.gov/books/NBK470404, accessed: 28-Sep-2021.

[51] 'ENDAQ vibrationdata toolbox', https://endaq.com/pages/vibration-shock-analysis-software-vibrationdata-toolbox, accessed: 11-Dec-2021.

[52] 'Energy Very Endure, ER14250 Datasheet', www.farnell.com/datasheets/1480397.pdf, accessed: 15-Nov-2021.

[53] H. Eren and J. G. Webster, *Measurement, Instrumentation, and Sensors Handbook*. Boca Raton, USA: CRC Press, 2014.

[54] C. E. Erkiliç and A. Yalcin, 'Evaluation of the wearable technology market within the scope of digital health technologies', *GJEB*, vol. 6, no. 3, 2020.

[55] A. Erturk and D. J. Inman, 'An experimentally validated bimorph cantilever model for piezoelectric energy harvesting from base excitations', *Smart Mater. Struct.*, vol. 18, no. 2, 025009, 2009.

[56] A. Erturk and D. J. Inman, *Piezoelectric Energy Harvesting*. New Yeork, NY, USA: John Wiley & Sons, 2011.

[57] 'EU EnABLES (European Infrastructure Powering the Internet of Things) H2020-INFRAIA-2014-2015 Grant no. 730957', www.enables-project.eu, accessed: 21-Mar-2021.

[58] K. Fan, Q. Tan, H. Liu, Y. Zhu, W. Wang, and D. Zhang, 'Hybrid piezoelectric-electromagnetic energy harvester for scavenging energy from low-frequency excitations', *Smart Mater. Struct.*, vol. 27, no. 8, 085001, 2018.

[59] 'Faulhaber Technical Information', www.faulhaber.com, accessed: 11-Nov-2021.

[60] M. Febbo, S. P Machado, and S. M Osinaga, 'A novel up-converting mechanism based on double impact for non-linear piezoelectric energy harvesting', *J. Phys. D: Appl. Phys.*, vol. 53, no. 47, 475501, 2020.

[61] 'Flashforge Creator 3 technical data', www.flashforge.com/product-detail/flashforge-creator-3-fdm-3d-printer, accessed: 13-Dec-2021.

[62] H. Fu et al., 'Rotational energy harvesting for self-powered sensing', *Joule*, vol. 5, no. 5, pp. 1074–118, 2021.

[63] X. Fu and W.-H. Liao, 'Modeling and Analysis of Piezoelectric Energy Harvesting With Dynamic Plucking Mechanism', *J. Vib. Acoust.*, vol. 141, no. 3, 031002, 2019.

[64] M. Gallina and D. Benasciutti, 'Finite element analysis of optimized piezoelectric bimorphs for vibrational "energy harvesting"', *Proc. Int. CAE Conf.*, pp. 1–4, 2013.

[65] A. Gebhardt and J.-S. Hötter, *Additive Manufacturing 3D Printing for Prototyping and Manufacturing*. München, DE: Carl Hanser Verlag, 2016.

[66] T. N. Gia et al., 'IoT-based continuous glucose monitoring system: A feasibility study', *Procedia Comput. Sci.*, vol. 109, pp. 327–34, 2017.

[67] I. Gibson, D. Rosen, and B. Stucker, *Additive Manufacturing Technologies*. New York, NY, USA: Springer, 2015.

[68] P. Gljuscic and S. Zelenika, 'Coupled Electromechanical Numerical Modelling of Piezoelectric Vibration Energy Harvesters', *DAAAM Proceedings*, vol. 1, pp. 0009–0015, 2018

[69] P. Gljušćić and S. Zelenika, 'Assessment of performances of optimized piezoelectric energy harvesters for wearables', *Proc. 20th Int. EUSPEN Conf.*, Geneva, CH, pp. 49–52, 2020.

[70] P. Gljušćić and S. Zelenika, 'Experimental Characterization of Optimized Piezoelectric Energy Harvesters for Wearable Sensor Networks', *Sensors*, vol. 21, no. 21, 7042, 2021.

[71] P. Gljušćić, S. Zelenika, D. Blažević, and E. Kamenar, 'Kinetic Energy Harvesting for Wearable Medical Sensors', *Sensors*, vol. 19, no. 22, 4922, 2019.

[72] P. Gljuscic, S. Zelenika, and E. Kamenar, 'Characterisation of Performances of Thermoelectric Generators for Energy Harvesting Applications', *DAAAM Proceedings*, vol. 1, pp. 0025–0030, 2018.

[73] P. Gljuscic, S. Zelenika, M. Perčić, and E. Kamenar, 'Experimental characterisation of performances of optimized piezoelectric energy harvesters', *Proc. 21st Int. EUSPEN Conf.*, Copenhagen, DK, pp. 131–34, 2021.

[74] S. Gong et al., 'A wearable and highly sensitive pressure sensor with ultrathin gold nanowires', *Nat. Commun.*, vol. 5, no. 1, 3132, 2014.

[75] J. Greiwe and S. M. Nyenhuis, 'Wearable Technology and How This Can Be Implemented into Clinical Practice', *Curr. Allergy Asthm. R.*, vol. 20, no. 8, 36, 2020.

[76] L. Gu and C. Livermore, 'Impact-driven, frequency up-converting coupled vibration energy harvesting device for low frequency operation', *Smart Mater. Struct.*, vol. 20, no. 4, 045004, 2011.

[77] M. A. Halim, M. H. Kabir, H. Cho, and J. Y. Park, 'A Frequency Up-Converted Hybrid Energy Harvester Using Transverse Impact-Driven Piezoelectric Bimorph for Human-Limb Motion', *Micromachines*, vol. 10, no. 10, 701, 2019.

[78] C. S. Han, K. Liu, J. H. Kim, D. H. Kang, and Y. S. Cho, 'Internal-field-dependent low-frequency piezoelectric energy harvesting characteristics of in situ processed Nb-doped Pb(Zr,Ti)O3 thin-film cantilevers', *J. Alloy. Compd.*, vol. 781, pp. 898–903, 2019.

[79] M. Hassan, W. Hu, G. Lan, A. Seneviratne, S. Khalifa, and S. K. Das, 'Kinetic-Powered Health Wearables: Challenges and Opportunities', *Computer*, vol. 51, no. 9, pp. 64–74, 2018.

[80] K. Hayashi et al., 'A 385×385μm2 0.165V 0.27nW Fully-Integrated Supply-Modulated OOK Transmitter in 65nm CMOS for Glasses-Free, Self-Powered, and Fuel-Cell-Embedded Continuous Glucose Monitoring Contact Lens', *IEICE T. Electron.*, vol. E102.C, no. 7, pp. 590–4,

2019.

[81] L. He, Z. Wang, X. Wu, Z. Zhang, D. Zhao, and X. Tian, 'Analysis and experiment of magnetic excitation cantilever-type piezoelectric energy harvesters for rotational motion', *Smart Mater. Struct.*, vol. 29, no. 5, 055043, 2020.

[82] R. Hernandez, D. Slaughter, D. Whaley, J. Tate, and B. Asiabanpour, 'Analyzing the Tensile, Compressive, and Flexural Properties of 3D Printed ABS P430 Plastic Based on Printing Orientation Using Fused Deposition Modeling', *Proc. 26th Ann. Int. Solid Freeform Fabr. Sym.*, San Marcos, TX, USA pp. 939–50, 2016.

[83] S. Z. Homayounfar et al., 'Multimodal Smart Eyewear for Longitudinal Eye Movement Tracking', *Matter*, vol. 3, no. 4, pp. 1275–93, 2020.

[84] A. Homayouni-Amlashi, A. Mohand-Ousaid, and M. Rakotondrabe, 'Multi Directional Piezoelectric Plate Energy Harvesters Designed By Topology Optimization Algorithm', *IEEE Robot. Autom. Lett.*, vol. 5, no. 2, pp. 462–9, 2020.

[85] H. Honma, Y. Tohyama, H. Mitsuya, G. Hashiguchi, H. Fujita, and H. Toshiyoshi, 'A power-density-enhanced MEMS electrostatic energy harvester with symmetrized high-aspect ratio comb electrodes', *J. Micromech. Microeng.*, vol. 29, no. 8, 084002, 2019.

[86] Huan Xue, Yuantai Hu, and Qing-ming Wang, 'Broadband piezoelectric energy harvesting devices using multiple bimorphs with different operating frequencies', *IEEE Trans. Ultras., Ferroel. Freq. Contr.*, vol. 55, no. 9, pp. 2104–8, 2008.

[87] 'HY3002D-2 power supply', http://www.tlead.biz/products/meters/DC_Power_Supply/597.html, accessed: 18-Jan-2022.

[88] V. In and A. Palacios, 'Energy Harvesting', in *Symmetry in Complex Network Systems*, Berlin, Heidelberg, DE: Springer, pp. 295–316, 2018.

[89] D. J. Inman, *Engineering vibration*, 4th ed., Internat. ed. Boston, MA, USA: Pearson, 2014.

[90] I. Izadgoshasb, Y. Y. Lim, L. Tang, R. V. Padilla, Z. S. Tang, and M. Sedighi, 'Improving efficiency of piezoelectric based energy harvesting from human motions using double pendulum system', *Energ. Convers. Manage.*, vol. 184, pp. 559–70, 2019.

[91] P. Janphuang, R. Lockhart, S. Henein, D. Briand, and N. F. de Rooij, 'On the experimental determination of the efficiency of piezoelectric impact-type energy harvesters using a rotational flywheel', *J. Phys.: Conf. Ser.*, vol. 476, 012137, 2013.

[92] J. Jiang, S. Liu, L. Feng, and D. Zhao, 'A Review of Piezoelectric Vibration Energy Harvesting with Magnetic Coupling Based on Different Structural Characteristics', *Micromachines*, vol. 12, no. 4, 436, 2021.

[93] S. Ju and C.-H. Ji, 'Indirect impact based piezoelectric energy harvester for low frequency vibration', *Transducers - 18th Int. Conf. Solid-State Sens. Actuators Microsyst.*, Anchorage, AK, USA, pp. 1913–6, 2015.

[94] E. Kamenar et al., 'Harvesting of river flow energy for wireless sensor network technology',

Microsyst. Technol., vol. 22, no. 7, pp. 1557–74, 2016.

[95] A. Kamišalić, I. Fister, M. Turkanović, and S. Karakatič, 'Sensors and Functionalities of Non-Invasive Wrist-Wearable Devices: A Review', *Sensors*, vol. 18, no. 6, 1714, 2018.

[96] B. Kathpalia, D. Tan, I. Stern, and A. Erturk, 'An experimentally validated model for geometrically nonlinear plucking-based frequency up-conversion in energy harvesting', *Smart Mater. Struct.*, vol. 27, no. 1, 015024, 2018.

[97] T. J. Kaźmierski, Ed., *Energy harvesting systems: principles modeling and applications.* New York, NY, USA: Springer, 2011.

[98] Y. Khan, A. E. Ostfeld, C. M. Lochner, A. Pierre, and A. C. Arias, 'Monitoring of Vital Signs with Flexible and Wearable Medical Devices', *Adv. Mater.*, vol. 28, no. 22, pp. 4373–95, 2016.

[99] D.-H. Kim et al., 'Epidermal Electronics', *Science*, vol. 333, no. 6044, pp. 838–43, 2011.

[100] M. Kim, J. Dugundji, and B. L. Wardle, 'Efficiency of piezoelectric mechanical vibration energy harvesting', S*mart Mater. Struct.*, vol. 24, no. 5, 055006, 2015.

[101] A. Komolafe et al., 'Integrating Flexible Filament Circuits for E-Textile Applications', *Adv. Mater. Technol.*, vol. 4, no. 7, 1900176, 2019.

[102] N. Krayner and R. Katz, 'Measuring Simplicity in Mechanical Design', *Procedia Manuf.*, vol. 21, pp. 878–89, 2018.

[103] Y. Kuang and M. Zhu, 'Design study of a mechanically plucked piezoelectric energy harvester using validated finite element modelling', *Sensor. Actuat. A-Phys.*, vol. 263, pp. 510–20, 2017.

[104] L. J. Kumar, P. M. Pandey, and D. I. Wimpenny, Eds., *3D Printing and Additive Manufacturing Technologies*. Singapore: Springer, 2019.

[105] P. Kumari, L. Mathew, and P. Syal, 'Increasing trend of wearables and multimodal interface for human activity monitoring: A review', *Biosens. Bioelectron.*, vol. 90, pp. 298–307, 2017.

[106] 'Laird - bluetooth modules', www.lairdconnect.com/wireless-modules/bluetooth-modules/bluetooth-42-and-40-modules/bt900-series-bluetooth-module, accessed: 24-Nov-2021.

[107] S. Leadenham and A. Erturk, 'Nonlinear M-shaped broadband piezoelectric energy harvester for very low base accelerations: primary and secondary resonances', *Smart Mater. Struct.*, vol. 24, no. 5, 055021, 2015.

[108] H. Lee et al., 'Toward all-day wearable health monitoring: An ultralow-power, reflective organic pulse oximetry sensing patch', *Sci. Adv.*, vol. 4, no. 11, eaas9530, 2018.

[109] H. Li, D. Liu, J. Wang, X. Shang, and M. R. Hajj, 'Broadband bimorph piezoelectric energy harvesting by exploiting bending-torsion of L-shaped structure', *Energy Convers. Manag.*, vol. 206, 112503, 2020.

[110] J. Li et al., 'Human-Body-Coupled Power-Delivery and Ambient-Energy-Harvesting ICs for a Full-Body-Area Power Sustainability', *2020 IEEE Int. Solid-State Circ. Conf.*, San Francisco, CA, USA, pp. 514–16, 2020.

[111] Y. C. Lo, C. C. Chen, Y. C. Shu, and M. F. Lumentut, 'Broadband piezoelectric energy harvesting induced by mixed resonant modes under magnetic plucking', *Smart Mater. Struct.*, vol. 30, no. 10, 105026, 2021.

[112] R. Lockhart, P. Janphuang, D. Briand, and N. F. de Rooij, 'A wearable system of micromachined piezoelectric cantilevers coupled to a rotational oscillating mass for on-body energy harvesting', I*EEE 27th Int. Conf. MEMS*, San Francisco, CA, USA, pp. 370–3, 2014.

[113] T. Luczak, R. Burch, E. Lewis, H. Chander, and J. Ball, 'State-of-the-art review of athletic wearable technology: What 113 strength and conditioning coaches and athletic trainers from the USA said about technology in sports', *Int. J. Sports Sci. Coa.*, vol. 15, no. 1, pp. 26–40, 2020.

[114] Y. Luo, L. Pu, G. Wang, and Y. Zhao, 'RF Energy Harvesting Wireless Communications: RF Environment, Device Hardware and Practical Issues', *Sensors*, vol. 19, no. 13, 3010, 2019.

[115] X. Ma, S. Bader, and B. Oelmann, 'Power Estimation for Indoor Light Energy Harvesting Systems', *IEEE Trans. Instrum. Meas.*, vol. 69, no. 10, pp. 7513–21, 2020.

[116] S. Majumder, T. Mondal, and M. Deen, 'Wearable Sensors for Remote Health Monitoring', *Sensors*, vol. 17, no. 12, 130, 2017.

[117] P. Malnar, 'Karakterizacija polimernih materijala za 3D tisak pasivnih komponenti rehabilitacijskih uređaja', Master's thesis, Rijeka, HR: University of Rijeka, Croatia, Faculty of Engineering, 2022.

[118] M. Malvić, 'Sustavi za prikupljanje niskorazinske energije iz okoliša', Student paper, Rijeka, HR: University of Rijeka, Faculty of Engineering, 2021.

[119] E. Marković, 'Eksperimentalna analiza piezoelektričnih pretvarača za nosive tehnologije podvrgnutih impulsnoj uzbudi', Master's thesis, Rijeka, HR: University of Rijeka, Croatia, Faculty of Engineering, 2021.

[120] E. Marković, S. Zelenika, P. Gljušćić, and M. Perčić, 'Experimental study of the effect of plectrum parameters on the performances of plucked piezoelectric energy harvesters', accepted for publication to the 22nd Int. Conf., Geneva, CH, 2022.

[121] D. O. Masara, H. El Gamal, and O. Mokhiamar, 'Split Cantilever Multi-Resonant Piezoelectric Energy Harvester for Low-Frequency Application', *Energies*, vol. 14, no. 16, 5077, 2021.

[122] I. Mathews et al., 'Analysis of CdTe photovoltaic cells for ambient light energy harvesting', J. Phys. D: Appl. Phys., vol. 53, no. 40, 405501, 2020.

[123] P. G. Mathews, *Design of experiments with MINITAB*. Milwaukee. WI, USA: ASQ Quality Press, 2005.

[124] H. M. Matt and F. L. di Scalea, 'Macro-fiber composite piezoelectric rosettes for acoustic source location in complex structures', *Smart Mater. Struct.*, vol. 16, no. 4, pp. 1489–99, 2007.

[125] 'Maxell, CR2032 Datasheet', biz.maxell.com/en/primary_batteries/CR2032H_DataSheet_16e.pdf, accessed: 25-Nov-2021.

[126] 'Maxim Integrated - Analog, linear, & mixed-signal devices'. www.maximintegrated.com/en.html, accessed: 14-Oct-2019.

[127] R. Mead, S. G. Gilmour, and A. Mead, *Statistical Principles for the Design of Experiments.* Cambridge, UK: Cambridge University Press, 2012.

[128] L. Meirovitch, *Fundamentals of vibrations*. Boston, MA, USA: McGraw-Hill, 2001.

[129] E. M. Melchor-Martínez, R. Macias-Garbett, A. Malacara-Becerra, H. M. N. Iqbal, J. E. Sosa-Hernández, and R. Parra-Saldívar, 'Environmental impact of emerging contaminants from battery waste: A mini review', *CSCEE*, vol. 3, 100104, 2021.

[130] 'Metrolaser Vibromet 500V vibrometer', http://www.metrolaserinc.com/products/vibrometer/, accessed: 18-Jan-2022.

[131] 'Microchip Technology', www.microchip.com, accessed: 14-Oct-2019.

[132] P. D. Mitcheson, E. M. Yeatman, G. K. Rao, A. S. Holmes, and T. C. Green, 'Energy Harvesting From Human and Machine Motion for Wireless Electronic Devices', *Proc. IEEE*, vol. 96, no. 9, pp. 1457–86, 2008.

[133] 'Mixed-signal and digital signal processing ICs | Analog Devices', www.analog.com/en/index.html, accessed: 14-Oct-2019.

[134] K. Moon, J. Choe, H. Kim, D. Ahn, and J. Jeong, 'A method of broadening the bandwidth by tuning the proof mass in a piezoelectric energy harvesting cantilever', *Sensor. Actuat. A-Phys.*, vol. 276, pp. 17–25, 2018.

[135] L. Moro, 'Analisi di Configurazione e Modellazione Elettromeccanica di Dispositivi Piezoelettrici per Accumulo di Energia', Master's thesis, Udine, IT: Università degli Studi di Udine, 2007.

[136] L. Moro and D. Benasciutti, 'Harvested power and sensitivity analysis of vibrating shoe-mounted piezoelectric cantilevers', *Smart Mater. Struct.*, vol. 19, no. 11,115011, 2010.

[137] 'Mouser', eu.mouser.com, accessed: 15-Nov-2021.

[138] 'MS Excel Solver algorithms', www.solver.com/excel-solveralgorithms- and-methods-used, accessed: 18-Jan-2022.

[139] 'Multicomp, Lithium-ion 120 mAh battery LIR2450 datasheet', www.farnell.com/datasheets/1475807.pdf, accessed: 25-Nov-2021.

[140] 'National Physics Laboratory, Notes on Applied Science No. 15', H.M. Stationary office, London, UK, 1956.

[141] 'NI LabVIEW', https://www.ni.com/en-rs/shop/labview.html, accessed: 18-Jan-2022.

[142] 'NI MyRIO 1900', https://www.ni.com/en-rs/support/model.myrio-1900.html, Accessed: 18-Jan-2022.

[143] D. W. Nicholson, *Finite Element Analysis: Thermomechanics of Solids*. Boca Raton, FL, USA: CRC Press, 2003.

[144] J. Noh, P. Kim, and Y.-J. Yoon, 'Load Resistance Optimization of a Magnetically Coupled

Two-Degree-of-Freedom Bistable Energy Harvester Considering Third-Harmonic Distortion in Forced Oscillation', *Sensors*, vol. 21, no. 8, 2668, 2021.

[145] A. Nozariasbmarz et al., 'Review of wearable thermoelectric energy harvesting: From body temperature to electronic systems', *Appl. Energ.*, vol. 258, 114069, 2020.

[146] M. Okayasu, G. Ozeki, and M. Mizuno, 'Fatigue failure characteristics of lead zirconate titanate piezoelectric ceramics', *J. Eur. Ceram. Soc.*, vol. 30, no. 3, pp. 713–25, 2010.

[147] D. Oletic and V. Bilas, 'System-Level Power Consumption Analysis of the Wearable Asthmatic Wheeze Quantification', *J. Sensors*, vol. 2018, pp. 1–18, 2018.

[148] Q. Ouyang et al., 'Self-powered, on-demand transdermal drug delivery system driven by triboelectric nanogenerator', *Nano Energy*, vol. 62, pp. 610–9, 2019.

[149] 'Panasonic, 1F supercapacitor EECRG0V105V datasheet', industrial.panasonic.com/cdbs/wwwdata/ pdf/RDG0000/ABC0000C80.pdf, accessed: 25-Nov-2021.

[150] J. Park, S. Lee, and B. M. Kwak, 'Design optimization of piezoelectric energy harvester subject to tip excitation', *J. Mech. Sci. Technol.*, vol. 26, no. 1, pp. 137–43, 2012.

[151] Y. Peng et al., 'Investigation of frequency-up conversion effect on the performance improvement of stack-based piezoelectric generators', *Renewable Energy*, vol. 172, pp. 551–63, 2021.

[152] M. Perčić, S. Zelenika, I. Mezić, R. Peter, and N. Krstulović, 'An experimental methodology for the concurrent characterization of multiple parameters influencing nanoscale friction', *Friction*, vol. 8, no. 3, pp. 577–93, 2020.

[153] 'piezo.com'. piezo.com, accessed: 20-Feb-2021.

[154] P. Pillatsch, E. M. Yeatman, and A. S. Holmes, 'A piezoelectric frequency up-converting energy harvester with rotating proof mass for human body applications', *Sensor. Actuat. A-Phys.*, vol. 206, pp. 178–85, 2014.

[155] M. Pozzi, 'Magnetic plucking of piezoelectric bimorphs for a wearable energy harvester', *Smart Mater. Struct.*, vol. 25, no. 4, 045008, 2016.

[156] M. Pozzi, M. S. H. Aung, M. Zhu, R. K. Jones, and J. Y. Goulermas, 'The pizzicato knee-joint energy harvester: characterization with biomechanical data and the effect of backpack load', *Smart Mater. Struct.*, vol. 21, no. 7, 075023, 2012.

[157] M. Pozzi and M. Zhu, 'Plucked piezoelectric bimorphs for energy harvesting applications', *SPIE (International Society for Optical Engineering) Proceedings*, vol. 8066: Smart Sensors, Actuators and MEMS V (ed. Schmid U., Sanchez-Rojas J. L. and Leester-Schaedel M.), 2011, 806616.

[158] 'Premier Farnell Limited', www.farnell.com, accessed: 20-Dec-2021.

[159] S. Priya, 'Modeling of electric energy harvesting using piezoelectric windmill', *Appl. Phys. Lett.*, vol. 87, no. 18, 184101, 2005.

[160] S. Priya and D. J. Inman, Eds., *Energy harvesting technologies*. New York, NY: Springer, 2009.

[161] S. Qi, R. Shuttleworth, S. Olutunde Oyadiji, and J. Wright, 'Design of a multiresonant beam for

broadband piezoelectric energy harvesting', *Smart Mater. Struct.*, vol. 19, no. 9, 094009, 2010.

[162] F. Qian, S. Zhou, and L. Zuo, 'Approximate solutions and their stability of a broadband piezoelectric energy harvester with a tunable potential function', *Commun. Nonlinear Sci. Numer. Simul.*, vol. 80, 104984, 2020.

[163] Qing-Ming Wang and L. E. Cross, 'Constitutive equations of symmetrical triple layer piezoelectric benders', *IEEE Trans. Ultrason., Ferroelect., Freq. Contr.*, vol. 46, no. 6, pp. 1343–51, 1999.

[164] 'Research Stereomicroscope System SZX16', https://www.olympus-ims.com/en/microscope/szx16, accessed: 18-Jan-2022.

[165] 'ROHM - New High Performance Optical Sensor for Heart Rate Monitoring Ideal for Wearables',www.rohm.com/news-detail?news-title=new-high-performance-optical-sensor-for-heart-rate-monitoring&defaultGroupId=false, accessed: 22-Nov-2021.

[166] 'ROHM Electronics basics - accelerometer-sensor',www.rohm.com/electronics-basics/sensor/accelerometer-sensor, accessed: 15-Nov-2021.

[167] 'ROHM Semiconductor - ROHM Co., Ltd.',www.rohm.com, accessed: 14-Oct-2019.

[168] V. J. Romero, J. V. Burkardt, M. D. Gunzberger, and J. S. Peterson, 'Initial evaluation of centroidal Voronoi tessellation method for statistical sampling and function integration', *Proc. 4th Int. Sym. Uncertainty Modeling and Analysis*, vol. ISUMA 2003, pp. 174–91, 2003.

[169] S. Roundy et al., 'Improving Power Output for Vibration-Based Energy Scavengers', *IEEE Pervas. Comput.*, vol. 4, no. 1, pp. 28–36, 2005.

[170] 'RWS Waterjet Service GmbH', www.stm-waterjet.com/en, accessed: 21-Feb-2021.

[171] H. Ryu, H. Yoon, and S. Kim, 'Hybrid Energy Harvesters: Toward Sustainable Energy Harvesting', *Adv. Mater.*, vol. 31, no. 34, 1802898, 2019.

[172] M. Safaei, H. A. Sodano, and S. R. Anton, 'A review of energy harvesting using piezoelectric materials: state-of-the-art a decade later (2008–2018)', *Smart Mater. Struct.*, vol. 28, no. 11, 113001, 2019.

[173] C. Saito, K. Masai, and M. Sugimoto, 'Classification of Spontaneous and Posed Smiles by Photo-reflective Sensors Embedded with Smart Eyewear', *Proc. 14th Int. Conf. Tang., Embed., Embod. Inter.*, Sydney, NSW, AU, pp. 45–52, 2020.

[174] T. Salo et al., 'Continuous blood pressure monitoring utilizing a CMOS tactile sensor', *26th Ann. Int. Conf. IEEE Eng. Med. Biol. Soc.*, vol. 3, San Francisco, CA, USA, pp. 23226–29, 2004.

[175] E. Sazonov, *Wearable Sensors - Fundamentals, Implementation and Applications*, 2nd ed. London, UK: Academic Press, 2020.

[176] S. Seneviratne et al., 'A Survey of Wearable Devices and Challenges', *IEEE Commun. Surv. Tut.*, vol. 19, no. 4, pp. 2573–620, 2017.

[177] D. Shen, J.-H. Park, J. Ajitsaria, S.-Y. Choe, H. C. Wikle, and D.-J. Kim, 'The design, fabrication and evaluation of a MEMS PZT cantilever with an integrated Si proof mass for vibration energy harvesting', *J. Micromech. Microeng.*, vol. 18, no. 5, 055017, 2008.

[178] G. Shi et al., 'A Multifunctional Wearable Device with a Graphene/Silver Nanowire Nanocomposite for Highly Sensitive Strain Sensing and Drug Delivery', *J. Carbon Res.*, vol. 5, no. 2, 17, 2019.

[179] G. Shi, Y. Yang, J. Chen, Y. Peng, H. Xia, and Y. Xia, 'A broadband piezoelectric energy harvester with movable mass for frequency active self-tuning', *Smart Mater. Struct.*, vol. 29, no. 5, 055023, 2020.

[180] L. Shuai, Z. H. Guo, P. Zhang, J. Wan, X. Pu, and Z. L. Wang, 'Stretchable, self-healing, conductive hydrogel fibers for strain sensing and triboelectric energy-harvesting smart textiles', *Nano Energy*, vol. 78, 105389, 2020.

[181] C. W. de Silva, *Sens. Act.: Eng. Sys. Instrum*. Boca Raton, FL, USA: CRC Press, 2015.

[182] 'SKF W 617/3 R Technical specification', https://www.skf.com/id/products/rolling-bearings/ball-bearings/deep-groove-ball-bearings/productid-W%20617%2F3%20R, accessed: 12-Aug-2021.

[183] 'SKF W 617/3 Technical specification', https://www.skf.com/sg/products/rolling-bearings/ball-bearings/deep-groove-ball-bearings/productid-W%20617%2F3, 12-Aug-2021.

[184] H. A. Sodano, D. J. Inman, and G. Park, 'Comparison of Piezoelectric Energy Harvesting Devices for Recharging Batteries', *J. Intel. Mat. Syst. Str.*, vol. 16, no. 10, pp. 799–807, 2005.

[185] H. A. Sodano, G. Park, and D. J. Inman, 'Estimation of Electric Charge Output for Piezoelectric Energy Harvesting', *Strain*, vol. 40, no. 2, pp. 49–58, 2004.

[186] D. Sopic, A. Aminifar, A. Aminifar, and D. Atienza, 'Real-Time Event-Driven Classification Technique for Early Detection and Prevention of Myocardial Infarction on Wearable Systems', *IEEE Trans. Biomed. Circuits Syst.*, vol. 12, no. 5, pp. 982–92, 2018.

[187] J. Sorić, *Finite Element Method*. Zagreb, HR: Golden marketing - Tehnička knjiga, 2004.

[188] 'Stratasys FDM Support Materials', support.stratasys.com/en/materials/fdm/fdm-support-materials, accessed: 13-Dec-2021.

[189] 'Stratasys Fortus 250mc technical data', support.stratasys.com/en/printers/fdm/fortus-250mc, accessed: 13-Dec-2021.

[190] W. Sun, Z. Cai, Y. Li, F. Liu, S. Fang, and G. Wang, 'Security and Privacy in the Medical Internet of Things: A Review', *Secur. Commun. Netw.*, vol. 2018, pp. 1–9, 2018.

[191] G. Takács and B. Rohal Ilkiv, *Model Predictive Vibration Control: Efficient constrained MPC vibration control for lightly damped mechanical systems*. London, UK: Springer, 2012.

[192] Y. K. Tan, *Energy Harvesting Autonomous Sensor Systems: Design, Analysis, and Practical Implementation*. Boca Raton, FL, USA: CRC Press, 2013.

[193] M. Tavakoli, L. Turicchia, and R. Sarpeshkar, 'An Ultra-Low-Power Pulse Oximeter Implemented With an Energy-Efficient Transimpedance Amplifier', *IEEE T. Biomed. Circ. S.*, vol. 4, no. 1, pp. 27–38, 2010.

[194] L. Tawalbeh, F. Muheidat, M. Tawalbeh, and M. Quwaider, 'IoT Privacy and Security: Challenges and Solutions', *Appl. Sci.-Basel*, vol. 10, no. 12, 4102, 2020.

[195] 'Texas Instruments Inc.', www.ti.com, accessed: 20-Dec-2021.

[196] 'Time Electronics 1051 Resistance Decade Box technical data',www.timeelectronics.com/decade-boxes/1051-8-decade-resistance-box,accessed: 11-Nov-2021.

[197] S. Timoshenko, *Strength of Materials, Part II: Advanced Theory and Problems*. New York, NY, USA: Van Nostrand Co., 1980.

[198] J. Twiefel and H. Westermann, 'Survey on broadband techniques for vibration energy harvesting', *J. Intel. Mat. Syst. Str.*, vol. 24, no. 11, pp. 1291–302, 2013.

[199] 'University of Rijeka, Croatia, Centre for Micro- and Nanosciences and technologies, Laboratory for Precision Engineering and Micro- and Nanosystems Technologies', nanori.uniri.hr/lpemnt, accessed: 13-Dec-2021.

[200] 'University of Rijeka, Croatia, Faculty of Engineering, Precision Engineering Laboratory', precenglab.riteh.uniri.hr,accessed: 19-Jul-2021.

[201] M. Vasiliev, M. Nur-E-Alam, and K. Alameh, 'Recent Developments in Solar Energy-Harvesting Technologies for Building Integration and Distributed Energy Generation', *Energies*, vol. 12, no. 6, 1080, 2019.

[202] 'Vernier 3D-BTA technical data', www.vernier.com/product/3-axis-accelerometer, accessed: 11-Nov-2021.

[203] 'Vernier myDAQ Adapter', https://www.vernier.com/product/vernier-mydaq-adapter/, accessed: 18-Jan-2022.

[204] 'VINATech, 5F supercapacitor WEC3R0 505QG datasheet', www.farnell.com/datasheets/2579990.pdf, accessed: 25-Nov-2021.

[205] E. Volterra, E. C. Zachmanoglou, and H. Kolsky, 'Dynamics of Vibrations', *J. Appl. Mech.*, vol. 33, no. 4, pp. 956–6, 1966.

[206] M. Wagih, A. S. Weddell, and S. Beeby, 'Millimeter-Wave Textile Antenna for on-Body RF Energy Harvesting in Future 5G Networks', *2019 IEEE Wireless Power Transfer Conf. (WPTC)*, London, United Kingdom, pp. 245–8, 2019.

[207] C. Wang et al., 'Monitoring of the central blood pressure waveform via a conformal ultrasonic device', *Nat. Biomed.*, vol. 2, no. 9, pp. 687–95, 2018.

[208] Q. Wang, S. Ling, X. Liang, H. Wang, H. Lu, and Y. Zhang, 'Self-Healable Multifunctional Electronic Tattoos Based on Silk and Graphene', *Adv. Funct. Mater.*, vol. 29, no. 16, 1808695, 2019.

[209] J. Wasserlauf, C. You, R. Patel, A. Valys, D. Albert, and R. Passman, 'Smartwatch Performance

for the Detection and Quantification of Atrial Fibrillation', *Circ. Arrhythm. Electrophysiol*., vol. 12, no. 6, e006834, 2019.

[210] S. Wei, H. Hu, and S. He, 'Modeling and experimental investigation of an impact-driven piezoelectric energy harvester from human motion', *Smart Mater. Struct.*, vol. 22, no. 10, 105020, 2013.

[211] C. B. Williams and R. B. Yates, 'Analysis of a micro-electric generator for microsystems', *Sensor. Actuat. A-Phys.*, vol. 52, no. 1, pp. 8–11, 1996.

[212] C. Wu et al., 'Self-Powered Iontophoretic Transdermal Drug Delivery System Driven and Regulated by Biomechanical Motions', *Adv. Funct. Mater.*, vol. 30, no. 3, 1907378, 2020.

[213] C. Wu, A. C. Wang, W. Ding, H. Guo, and Z. L. Wang, 'Triboelectric Nanogenerator: A Foundation of the Energy for the New Era', *Adv. Energy Mater.*, vol. 9, no. 1, 1802906, 2019.

[214] Z. Xiao et al., 'An Implantable RFID Sensor Tag toward Continuous Glucose Monitoring', *IEEE J. Biomed. Health.*, vol. 19, no. 3, pp. 910–9, 2015.

[215] Z. Xie, J. Xiong, D. Zhang, T. Wang, Y. Shao, and W. Huang, 'Design and Experimental Investigation of a Piezoelectric Rotation Energy Harvester Using Bistable and Frequency Up-Conversion Mechanisms', *Appl. Sci.-Basel*, vol. 8, no. 9, 1418, 2018.

[216] Z. Xu, X. Shan, D. Chen, and T. Xie, 'A Novel Tunable Multi-Frequency Hybrid Vibration Energy Harvester Using Piezoelectric and Electromagnetic Conversion Mechanisms', *Appl. Sci.-Basel*, vol. 6, no. 1, 10, 2016.

[218] T. Xue, 'On magnetic plucking configurations for frequency up-converting mechanical energy harvesters', *Sensor. Actuat. A-Phys.*, vol. 253, pp. 101–1011, 2017.

[219] T. Xue, H. G. Yeo, S. Trolier-McKinstry, and S. Roundy, 'Wearable inertial energy harvester with sputtered bimorph lead zirconate titanate (PZT) thin-film beams', *Smart Mater. Struct*., vol. 27, no. 8, 085026, 2018.

[220] Y. Yang, Q. Shen, J. Jin, Y. Wang, W. Qian, and D. Yuan, 'Rotational piezoelectric wind energy harvesting using impact-induced resonance', *Appl. Phys. Lett.*, vol. 105, no. 5, 053901, 2014.

[221] Y. Yang and L. Tang, 'Equivalent Circuit Modeling of Piezoelectric Energy Harvesters', *J. Intel. Mat. Syst. Str.*, vol. 20, no. 18, pp. 2223–35, 2009.

[222] Z. Yang, A. Erturk, and J. Zu, 'On the efficiency of piezoelectric energy harvesters', *Extreme Mech. Lett.*, vol. 15, pp. 26–37, 2017.

[223] Z. Yang, K. Nakajima, R. Onodera, T. Tayama, D. Chiba, and F. Narita, 'Magnetostrictive clad steel plates for high-performance vibration energy harvesting', *Appl. Phys. Lett.*, vol. 112, no. 7, 073902, 2018.

[224] A. K. Yetisen, J. L. Martinez-Hurtado, B. Ünal, A. Khademhosseini, and H. Butt, 'Wearables in Medicine', *Adv. Mater.*, vol. 30, no. 33, 1706910, 2018.

[225] Z. Zaalouni, S. Beldi, and A. Gharsallah, 'Study of miniaturized E-patch antenna loaded with

novel E-shape SRR metamaterial for RFID applications', *Int. J. RF. Microw. C. E.*, vol. 29, no. 6, e21698, 2019.

[227] S. Zelenika et al., 'Energy Harvesting Technologies for Structural Health Monitoring of Airplane Components—A Review', *Sensors*, vol. 20, no. 22, 6685, 2020.

[228] H. Zhang, M. Alrifaai, K. Zhou, and H. Hu, 'A novel fuzzy logic algorithm for accurate fall detection of smart wristband', *T. I. Meas. Control*, vol. 42, no. 4, pp. 786–94, 2020.

[229] Y. Zhang, C. Ding, J. Wang, and J. Cao, 'High-energy Orbit Sliding Mode Control for Nonlinear Energy Harvesting', *Nonlinear Dynam.*, vol. 105, no. 1, pp. 191–211, 2021.

[230] D. Zhu, M. J. Tudor, and S. P. Beeby, 'Strategies for increasing the operating frequency range of vibration energy harvesters: a review', *Meast. Sci. Technol.*, vol. 21, no. 2, 022001, 2010.

[231] M. Zouari, S. Naifar, G. Bouattour, N. Derbel, and O. Kanoun, 'Energy management based on fractional open circuit and P-SSHI techniques for piezoelectric energy harvesting', *Tech. Mess.*, vol. 86, no. 1, pp. 14–24, 2019.

List of Symbols

Latinic Symbols

variable	definition, unit
$\mathbf{B}_d$	damping matrix, -
$C_{\tilde{p}}$	piezoelectric material capacitance, F
D	charge density, Cm^{-3}
d	piezoelectric strain coefficient, pC/N
d_{31}	piezoelectric strain coefficient – 31 direction, pC/N
d_{33}	piezoelectric strain coefficient – 33 direction, pC/N
E	elastic modulus, GPa
E_{el}	electric field, V/m
E_{PZT}	elastic modulus of the piezoelectric material, GPa
E_s	elastic modulus of the substrate, GPa
e_{r_Base}	relative error for base excitation, -
$e_{r\_FreeEnd}$	relative error for tip excitation, -
f	frequency, Hz
f_{1base}	1^{st} uncoupled eigenfrequency experimentally assessed via base excitation, Hz
f_{coup}	coupled eigenfrequency, Hz
f_{1_coup}	1^{st} coupled eigenfrequency, Hz
$f_{1FreeEnd}$	1^{st} uncoupled eigenfrequency experimentally assessed via tip excitation, Hz
f_{max}	frequency of the highest mode of interest, Hz
f_{mech}	uncoupled eigenfrequency, Hz
f_{1_mech}	1^{st} uncoupled eigenfrequency, Hz
$f_{1\_mech\_EXP}$	1^{st} uncoupled eigenfrequency – experimentally assessed, Hz
$f_{1\_mech\_FEA}$	1^{st} uncoupled eigenfrequency – obtained via FE analysis, Hz
f_{2_mech}	2^{nd} uncoupled eigenfrequency, Hz
g	gravitational acceleration g = 9,81 m/s^2
h_n	height of V shaped notch, m
I_0	no-load current, A
i	gear ratio, -
j	imaginary unit, -
$\mathbf{K}_S$	stiffness matrix, -
k_M	DC motor torque constant, Nm/A
l	length, m
l_0	overall cantilever length, m

$\mathbf{M}$	mass matrix, -
m	mass, g
n_0	rotational speed, min^{-1}
P	power, W
P_{av_EXP}	average experimentally obtained power, W
P_{av_FEA}	average FE calculated power, W
$P_{av\_\delta zmax}$	average power at maximum allowable tip deflection, W
P_{max}	maximal power, W
P_{max_EXP}	maximal experimentally obtained power, W
P_{max_FEA}	maximal FE calculated power, W
$P_{max\_\delta zmax}$	maximal power at maximum allowable tip deflection, W
P_{notch}	power generated by the notched shape, W
P_{n_av}	average normalized power, W/m
P_{n_max}	maximum normalized power, W/m
$P_{n\_s\_max}$	specific normalized power, $W/m^2/m$
P_s	specific power, W/m^2
P_{seg}	power generated by the segmented shape, W
R^2	coefficient of determination
R_d	fatigue stress limit, MPa
R_L	external electrical load, Ω
R_{Lopt}	optimal load resistance, Ω
T	oscillation period, s
t	thickness, m
t_{PZT}	thickness of the piezoelectric layer, m
t_S	thickness of the metallic substrate layer, m
U	voltage, V
U_{max}	maximal voltage, V
U_{max_EXP}	maximal voltage – experimentally assessed, V
U_{max_FEA}	maximal voltage obtained via FE analysis, V
$U_{n\_max\_p\text{-}p}$	normalized peak-to-peak voltage, V/mm
$U_{p\text{-}p}$	peak-to-peak voltage, V
$U_{p\text{-}p\_EXP}$	peak-to-peak voltage– experimentally assessed, V
$U_{p\text{-}p\_FEA}$	FE calculated peak-to-peak voltage, V
U_{RMS}	RMS voltage, V
w	width, m
w_c	width of clamped end (segment), m
w_f	width of free end (segment), m

w_n	width of V shaped notch, m
x	shape optimization variable, m
y	shape optimization variable, m
y_n, y_{n+1}	response peaks, m

Greek Symbols

variable	definition, unit
α	Rayleigh damping constant, -
α_R	normalized resistance, -
α_s	voltage amplitude, V
β	Rayleigh damping constant, -
Δt	time step in transient analyses, s
δ	mechanical strain, V/m
δ_{log}	logarithmic decrement, -
δ_z	tip displacement during the plucking process, m
δ_{z_max}	maximal allowable tip displacement during the plucking process, m
ε	dielectric constant of the piezoelectric material, pC/N
ζ	mechanical damping coefficient, -
ζ_r	damping coefficient, -
η	conversion efficiency of the cantilever PEH, -
κ	electromechanical coupling coefficient, -
κ_r	foreword coupling term, -
ν_{PZT}	Poisson's ratio of the piezoelectric material, -
ν_s	Poisson ratio of the substrate, -
ρ_{PZT}	density of the piezoelectric material, kg m^{-3}
ρ_s	density of the substrate material, kg m^{-3}
σ	mechanical stress, MPa
σ_r	translational excitation component, -
σ_{sd}	standard deviation, -
χ_r^s	modal coupling term, -
ω	excitation frequency near the eigenfrequency of the PEH, s^{-1}
$\tilde{\omega}$	frequency ratio, -
ω_r	eigenfrequency of the PEH, s^{-1}

List of Abbreviations

ABS	acrylonitrile butadiene styrene
AC	alternating current
ADC	analogue-to-digital converter
ADL	activities of daily living
AM	additive manufacturing
APDL	ANSYS parametric design language
ASTM	American Society for Testing and Materials
BASS	breakaway supports
CAD	computer-aided design
CCD	central composite design
CGM	continuous glucose monitoring
CMEDM	coupled modal electromechanical distributed parameter model
CMOS	complementary-metal–oxide–semiconductor
DAQ	data acquisition
DC	direct current
DoE	design-of-experiments
DoF	degree of freedom
EBM	electron beam melting
EH	energy harvesting
EM	electromagnetic
FDM	fused deposition modelling
FE	finite element
FEA	finite element analysis
FRF	frequency response functions
FUC	frequency up-conversion
GRG	generalized Reduced Gradient
HR	heart rate
IC	integrated circuit
IoT	internet-of-things
LCVT	latinized centroidal Voronoi tessellation
LED	light-emitting diode
MEMS	micro-electromechanical system
MFC	macro-fibre composite
MICS	medical implant communication service

OLED	organic light-emitting diode
PA	polyamide
PC	polycarbonate
PEH	piezoelectric energy harvester
PET	polyethylene terephthalate
PLA	polylactic acid
PWV	pulse wave velocity
PWA	pulse wave analysis
PZT	lead zirconate titanate
RF	radio frequency
RFID	radio frequency identification
RMS	root mean square
RSM	response surface methodology
RTD	resistance temperature detectors
SC	supercapacitor
SLS	selective laser sintering
TEG	thermoelectric generator
TENG	triboelectric energy nanogenerator
TO	topology optimization
VI	virtual instrument
WHO	World Health Organization
WW	water works support

List of Figures

List of Tables